DOE/ID/13746

New Heat Flow Models in Fractured Geothermal Reservoirs

Final Report – 04/01/1999 – 03/31/2001

J. Reis

March 2001

Work Performed Under Contract No. DE-FG07-99ID13746

For
U.S. Department of Energy
Assistant Secretary for
Energy Efficiency and Renewable Energy
Washington, DC

By
Reis and Associates
Prescott Valley, AZ

DOE/ID/13746

NEW HEAT FLOW MODELS IN FRACTURED GEOTHERMAL RESERVOIRS

FINAL REPORT
04/01/1999 – 03/31/2001

J. Reis

March 2001

Work Performed Under Contract No. DE-FG07-99ID13746

Prepared for the
U.S. Department of Energy
Assistant Secretary for
Energy Efficiency and Renewable Energy
Washington, DC

Prepared by
Reis and Associates
Prescott Valley, AZ

NEW HEAT FLOW MODELS IN FRACTURED GEOTHERMAL RESERVOIRS

Final Technical Report
for
Grant DE-FG07-99ID13746

March 31, 2001

John Reis
Reis and Associates
8157 E. Gale Road
Prescott Valley, AZ 86314

TABLE OF CONTENTS

Executive Summary

This study developed new analytical models for predicting the temperature distribution within a geothermal reservoir following reinjection of water having a temperature different from that of the reservoir. The study consisted of two parts: developing new analytical models for the heat conduction rate into multi-dimensional, parallelepiped matrix blocks and developing new analytical models for the advance of the thermal front through the geothermal reservoir.

In the first part of the study, a number of semi-empirical models for the multi-dimensional heat conduction were developed to overcome the limitations to the exact solutions. The exact solution based on a similarity solution to the heat diffusion equation is the best model for the early-time period, but fails when thermal conduction fronts from opposing sides of the matrix block merge. The exact solution based on an infinite series solution was found not to be useful because it required tens of thousands of terms to be included for accuracy. The best overall model for the entire conduction time was a semi-empirical model based on an exponential conduction rate.

In the second part of the study, the early-time period exact solution based on similarity methods and the semi-empirical exponential model were used to develop new analytical models for the location of the thermal front within the reservoir during reinjection. These equations were based on an energy balance on the water in the fracture network. These convective models allowed for both dual and triple porosity reservoirs, i.e., one or two independent matrix domains. A method for incorporating measured fracture spacing distributions into these convective models were developed. It was found that there were only minor differences in the predicted areal extend of the heated zone between the dual and triple porosity models. Because of its simplicity, the dual porosity model is recommended.

These new models can be used for preliminary reservoir studies. Although they are not as accurate as numerical simulators, they are simple, easy, and inexpensive to use. These new models can be used to get general information about reservoir behavior before committing to the considerably greater expense of numerical simulation.

1.0 Introduction

The ability to accurately predict the future performance of geothermal reservoirs is an important element in the economic success of geothermal energy projects. A critical element in predicting such performance is the ability to predict heat and fluid flow through geothermal reservoirs. A variety of performance models for nonfractured reservoirs are available (Bodvarsson, et al., 1986). Most of these models are of limited accuracy because they do not account for the effect of natural fractures that are commonly found in most geothermal reservoirs (Brook, et al., 1978).

Most studies of the effects of fractures in geothermal reservoirs are conducted using numerical simulators that have been derived from the dual porosity assumption (Pruess, et al., 1996). In its simplest form, this assumption treats the fracture network as a continuum through which fluid (and thermal energy) flows and the associated matrix blocks as sources and sinks of both fluid and energy. The crossflow of fluid and energy between the fractures and the matrix blocks is modeled through an appropriate transfer function (Pruess and Narasimhan, 1985 and Bodvarsson, et al., 1985).

While numerical modeling is a valuable tool for predicting geothermal reservoir performance, it is not suitable for all cases. One limitation to numerical modeling with existing simulators is the cost required to obtain useful information. Numerical simulation requires access to a suitable simulator, training on how to use the simulator, and a significant amount of reservoir data.

A set of analytical models for geothermal behavior are presented in this report that complements existing simulator technology. These new models are simpler and less costly to use than traditional simulators. These models also extend current technology for reservoir modeling by allowing the effect of a realistic fracture spacing distribution to be explicitly modeled instead of using the normal assumption that all fractures are evenly spaced and all matrix blocks are the same size and shape.

This study was conducted in two parts. During the first part, analytical models were developed for the crossflow of energy by thermal conduction into three-dimensional matrix blocks. Those models formed the basis of the transfer function for the crossflow of thermal energy between the fractures and matrix blocks. During the second part, those models were incorporated into new models for the advance of the thermal front in a fracture system having a realistic fracture spacing distribution.

2.0 Classical Thermal Conduction Models

In this section, existing analytical models for thermal conduction will be reviewed. These models are based on the solution to the heat diffusion equation. The heat diffusion equation can be written as

$$\frac{d}{dx}\left(K\frac{dT}{dx}\right)+\frac{d}{dy}\left(K\frac{dT}{dy}\right)+\frac{d}{dz}\left(K\frac{dT}{dz}\right)=\rho c_p\frac{dT}{dt}\ , \tag{2.0.1}$$

where K, ρ, and c_p are the thermal conductivity, density, and specific heat of the rock, respectively, T is the local temperature, x, y, and z are the spatial dimensions, and t is the time.

Although the thermal properties of geological formations vary somewhat with temperature (Somerton, 1992), this variation is relatively small and will be neglected. For the case of a constant thermal conductivity, Eq. 2.0.1 simplifies to the following equation:

$$\frac{d^2T}{dx^2}+\frac{d^2T}{dy^2}+\frac{d^2T}{dz^2}=\frac{1}{\alpha}\frac{dT}{dt}\ , \tag{2.0.2}$$

where α is the thermal diffusivity and is given by

$$\alpha=\frac{K}{\rho c_p}\ . \tag{2.0.3}$$

2.1 One-Dimensional Conduction

For the case of one-dimensional conduction, Eq. 2.0.2 simplifies to

$$\frac{d^2T}{dx^2}=\frac{1}{\alpha}\frac{dT}{dt}\ . \tag{2.1.1}$$

The initial and boundary conditions relevant to this study are a uniform initial temperature throughout the matrix block, T_i, and a step change in the surface temperature to its final value at time zero, T_s. The geometry assumed in this study is shown in Fig. 1. Carslaw and Jaeger (1959) presented several solution methods to this equation that are discussed below.

2.1.1 Square-Root Solution

For the case of conduction into a semi-infinite solid, Eq. 2.1.1 can be solved using similarity methods (Carslaw and Jaeger, 1959) to yield the following temperature profile:

$$T(x,t) = T_i + (T_s - T_i)\left[1 - \text{erf}\ \frac{x}{2\sqrt{\alpha t}}\ \right], \tag{2.1.2}$$

where

$$\text{erf}(v) = \frac{2}{\sqrt{\pi}} \int_0^v e^{-u^2} du \,. \tag{2.1.3}$$

The heat transfer rate into the matrix block can be found by differentiating the temperature profile with respect to position at the surface:

$$q = -KA \left.\frac{dT}{dx}\right|_{x=0} . \tag{2.1.4}$$

Substituting Eq. 2.1.2 into 2.1.4 and evaluating yields the following expression for the conduction rate:

$$q = KA(T_s - T_i)\sqrt{\frac{1}{\pi\alpha t}} \,. \tag{2.1.5}$$

This model for one-dimensional conduction assumes a semi-infinite solid. A more realistic one-dimensional geometry for geothermal applications would be parallel fractures from which a slab-shaped matrix block is simultaneously heated from opposite sides as shown in Fig. 1. For this case, the total heat conduction rate into a matrix block is the sum of the heat transfer rates from the two opposing sides:

$$q = 2KA(T_s - T_i)\sqrt{\frac{1}{\pi\alpha t}} \,. \tag{2.1.6}$$

The total amount of thermal energy that can be conducted into the matrix block after an infinite time is given by

$$Q_\infty = \rho c_p V(T_s - T_i), \tag{2.1.7}$$

where V is the total volume of the matrix block,

$$V = AL, \tag{2.1.8}$$

A is the surface area of one face of the matrix block, and L is the width of the matrix block.

By substituting Eqs. 2.1.7 and 2.1.8 into Eq. 2.1.6 the following equation is obtained for the heat conduction rate into both faces of the matrix block:

$$\frac{q}{Q_\infty} = \frac{2}{\sqrt{\pi}} \frac{\sqrt{\alpha}}{L} \sqrt{\frac{1}{t}}. \tag{2.1.9}$$

If a characteristic time for thermal conduction is defined as

$$t_{cl} = \frac{\pi L^2}{64\alpha}, \tag{2.1.10}$$

the resulting conduction rate can be expressed as

$$\frac{q t_{cl}}{Q_\infty} = \frac{1}{4} \sqrt{\frac{t_{cl}}{t}}. \tag{2.1.11}$$

As discussed in a later section on the Linear Temperature-Profile Model, this characteristic time is an estimate for the time it takes for the thermal fronts to reach the centerline of the matrix block.

The normalized cumulative amount of thermal energy conducted into the matrix block can be obtained by integrating Eq. 2.1.11 over time:

$$\frac{Q}{Q_\infty} = \frac{1}{2} \sqrt{\frac{t}{t_{cl}}}. \tag{2.1.12}$$

Equations 2.1.11 and 2.1.12 are valid as long as heat transfer from the two opposing faces can be individually modeled as heat transfer into a semi-infinite solid, i.e., the thermal fronts

from the opposing faces have not interfered with each other at the centerline of the matrix block. This condition is met during the early times of heat conduction.

2.1.2 Series Solution

A different model can be obtained for the temperature distribution in a one-dimensional matrix block using the method of separation of variables to solve Eq. 2.1.1 (Carslaw and Jaeger, 1959). The temperature profile for this case is given by

$$T(x,t) = T_s - (T_s - T_i)\frac{4}{\pi}\sum_{n=0}^{\infty}\frac{1}{(2n+1)}\exp\left[-(2n+1)^2\frac{\alpha\pi^2 t}{L^2}\right]\sin\left\{(2n+1)\frac{\pi}{L}x\right\}. \qquad (2.1.13)$$

The heat conduction rate into the matrix block can be obtained by substituting Eq. 2.1.13 into Eq. 2.1.4. Because conduction is occurring into both faces of the matrix block, the conduction rate is twice that given by Eq. 2.1.4. The resulting heat conduction rate into the matrix block is

$$q = 8\frac{KA(T_s - T_i)}{L}\sum_{n=0}^{\infty}\exp\left\{-(2n+1)^2\frac{\alpha\pi^2 t}{L^2}\right. \quad . \qquad (2.1.14)$$

The normalized conduction rate into the matrix block can be obtained by substituting Eqs. 2.1.7, 2.1.8, and 2.1.10 into Eq. 2.1.14

$$\frac{qt_{cl}}{Q_\infty} = \frac{\pi}{8}\sum_{n=0}^{\infty}\exp\left[-(2n+1)^2\frac{\pi^3}{64}\frac{t}{t_{cl}}\right] \quad . \qquad (2.1.15)$$

The cumulative amount of thermal energy conducted into the matrix block (from both faces) is obtained by integrating Eq. 2.1.15 over time:

$$\frac{Q}{Q_\infty} = \frac{8}{\pi^2}\sum_{n=0}^{\infty}\frac{1}{(2n+1)^2}\left[1-\exp\left[-(2n+1)^2\frac{\pi^3}{64}\frac{t}{t_{cl}}\right]\right]. \qquad (2.1.16)$$

Unlike the square-root model previous discussed, the infinite series model is valid during the entire conduction period.

2.1.3 Discussion of One-Dimensional Models

In the above sections, two analytical models have been presented for one-dimensional thermal conduction into a matrix block. These models are based on theoretical solutions for thermal conduction available in the literature (Carslaw and Jaeger, 1959). There models have been cast into a normalized (dimensionless) form for easy comparison.

The normalized conduction rate and cumulative energy conducted for these two models are compared in Figs. 2 and 3, respectively. The series model is presented for a variety of terms in the infinite series.

The square-root model is simple and exact for the very early times, but fails for the later times when the conduction fronts entering the matrix block from the opposing faces meet and begin to interact with each other. When this occurs, the semi-infinite geometry assumed to obtain this model is no longer valid.

The series model is valid over the entire time of conduction, but is accurate only when a large number of terms are included in the series. As seen in Fig. 3, if only a few terms are included, the amount of energy conducted between the matrix block and fractures is significantly underpredicted. The cumulative energy conducted asymptotes to the wrong value at an infinite time if too few terms are used. Although the conduction rate is accurately predicted for late times because the higher-order terms in the series have decayed, those higher-order terms contribute to the cumulative energy conducted and must be included. To model the cumulative energy conducted to within 1%, at least 25 terms must be included in the series.

These figures reveal the inadequacy of these one-dimensional analytical models for the practical modeling of thermal conduction between fractures and matrix blocks. The square-root model is impractical because it is only valid during the early part of the conduction process. The series model is impractical because of the computational requirements of including a sufficient number of terms in the series.

2.2 Multi-Dimensional Conduction

In the previous section, it was shown that the classical solutions to the one-dimensional heat diffusion equation were impractical for use in the geothermal reservoir modeling. In this section the corresponding solutions to the three-dimensional equation will be presented and discussed.

For the case of multi-dimensional conduction, Eq. 2.0.2 gives the temperatures as a function of position and time:

$$\frac{d^2T}{dx^2}+\frac{d^2T}{dy^2}+\frac{d^2T}{dz^2}=\frac{1}{\alpha}\frac{dT}{dt}\ . \tag{2.0.2}$$

2.2.1 Square-Root Solution

For the case of conduction into a three-dimensional semi-infinite solid, i.e., into the corner of a rectangular parallelepiped, Eq. 2.0.2 can be solved using similarity methods (Carslaw and Jaeger, 1959) to yield the following temperature profile:

$$T(x,y,z,t)=T_i+(T_s-T_i)\left[1-\mathrm{erf}\left(\frac{x}{2\sqrt{\alpha t}}\right)\mathrm{erf}\left(\frac{y}{2\sqrt{\alpha t}}\right)\mathrm{erf}\left(\frac{z}{2\sqrt{\alpha t}}\right)\right]. \tag{2.2.1}$$

Because the heat transfer rate varies with position along the surface of the semi-infinite solid, the simple application of Eq. 2.1.4 cannot be used for multi-dimensional geometries. There are two approaches that can be used to determine the heat conduction rate into the matrix block. One approach is to integrate the heat flux form of Eq. 2.1.4, i.e.,

$$q''=-K\left.\frac{dT}{d\xi}\right|_{\xi=0}, \tag{2.2.2}$$

over all three surfaces of the semi-infinite solid, where ξ is direction normal to each respective surface. This approach will not be used here.

The heat conduction rate into the matrix block will be determined from the time derivative of the thermal energy content in the matrix block:

$$q=\frac{dQ}{dt}=\frac{d}{dt}\left[\rho c_p V\left(\overline{T}-T_i\right)\right], \tag{2.2.3}$$

where $\overline{T}$ is the average temperature in the matrix block. If the parallelepiped matrix block has dimensions of L_x, L_y, and L_z, the total volume is

$$V=L_xL_yL_z\,. \tag{2.2.4}$$

Because Eq. 2.2.1 applies to only one corner and there are eight corners in a parallelepiped matrix block, the volume associated with one corner is

$$V_{corner} = \frac{L_x L_y L_z}{8}. \tag{2.2.5}$$

The average temperature in one corner of the matrix block is obtained by integrating the temperature, given by Eq. 2.2.1, over the volume of the corner:

$$\bar{T} = \frac{1}{V_{corner}} \int_0^{\frac{L_z}{2}} \int_0^{\frac{L_y}{2}} \int_0^{\frac{L_x}{2}} T(x,y,z)\,dx\,dy\,dz. \tag{2.2.6}$$

If the following approximations are made for the early-time period, i.e., before the thermal fronts from opposing sides begin to interfere with each other,

$$\exp\left(-\frac{L_x^2}{16\alpha t}\right) \approx \exp\left\{-\frac{L_y^2}{16\alpha t}\right\} \approx \exp\left\{-\frac{L_z^2}{16\alpha t}\right\} \approx 0 \tag{2.2.7}$$

and

$$\operatorname{erf}\left(\frac{L_x}{4\sqrt{\alpha t}}\right) \approx \operatorname{erf}\left\{\frac{L_y}{4\sqrt{\alpha t}}\right\} \approx \operatorname{erf}\left\{\frac{L_z}{4\sqrt{\alpha t}}\right\} \approx 1, \tag{2.2.8}$$

the average temperature in one corner becomes

$$\bar{T} = T_i + \frac{4(T_s - T_i)}{L_x L_y L_z}\left[\sqrt{\frac{\alpha t}{\pi}}\left(L_x L_y + L_y L_z + L_x L_z\right) - 4\frac{\alpha t}{\pi}\left(L_x + L_y + L_z\right) + 16\sqrt{\left(\frac{\alpha t}{\pi}\right)^3}\right]. \tag{2.2.9}$$

From symmetry, this is also the average temperature in the entire matrix block.

The total heat conduction rate (into all eight corners) can be found by substituting Eqs. 2.2.9 and 2.1.7 into Eq. 2.2.3:

$$q = Q_\infty\left[2\left(\frac{1}{L_x} + \frac{1}{L_y} + \frac{1}{L_z}\right)\sqrt{\frac{\alpha}{\pi t}} - 16\left(\frac{1}{L_x L_y} + \frac{1}{L_y L_z} + \frac{1}{L_x L_z}\right)\frac{\alpha}{\pi} + 96\frac{1}{L_x L_y L_z}\sqrt{t\left(\frac{\alpha}{\pi}\right)^3}\right]. \tag{2.2.10}$$

If a characteristic time for multi-dimensional thermal conduction is defined as

$$t_{cl} = \frac{L_x^2}{576\alpha} D_L, \tag{2.2.11}$$

where a dimensionless geometry factor has been defined as

$$D_L = \frac{\left(4L_xL_y + 4L_xL_z + 36L_yL_z - 5L_x^2\right)}{\left(L_xL_y + L_xL_z + L_yL_z\right)}, \tag{2.2.12}$$

the normalized conduction rate can be written as

$$\frac{qt_{cl}}{Q_\infty} = \frac{1}{12}\left[1 + \frac{L_x}{L_y} + \frac{L_x}{L_z}\right]\sqrt{\frac{D_L}{\pi}}\sqrt{\frac{t_{cl}}{t}} - \frac{1}{36}\left(\frac{L_x}{L_y} + \frac{L_x}{L_z} + \frac{L_x^2}{L_yL_z}\right)\frac{D_L}{\pi} + \frac{1}{144}\frac{L_x^2}{L_yL_z}\sqrt{\left(\frac{D_L}{\pi}\right)^3}\sqrt{\frac{t}{t_{cl}}}. \tag{2.2.13}$$

and the normalized cumulative energy conducted can be written as

$$\frac{Q}{Q_\infty} = \frac{1}{6}\left[1 + \frac{L_x}{L_y} + \frac{L_x}{L_z}\right]\sqrt{\frac{D_L}{\pi}}\sqrt{\frac{t}{t_{cl}}} - \frac{1}{36}\left(\frac{L_x}{L_y} + \frac{L_x}{L_z} + \frac{L_x^2}{L_yL_z}\right)\frac{D_L}{\pi}\frac{t}{t_{cl}} + \frac{1}{216}\frac{L_x^2}{L_yL_z}\sqrt{\left(\frac{D_L}{\pi}\right)^3}\sqrt{\left(\frac{t}{t_{cl}}\right)^3}. \tag{2.2.14}$$

For simplicity, Eqs. 2.2.13 and 2.2.14 will be referred to as the extended-square-root model. As will be discussed in a following section on the Linear Temperature-Profile Model, the characteristic time given by Eq. 2.2.11 is an estimate for the time it takes for the thermal front to reach the centerline of the matrix block.

The early-time behavior, i.e., the time before the thermal fronts from opposing sides begin to interact, does not follow the simple square-root behavior observed for one-dimensional geometry. The difference arises because of interference from adjacent sides of the matrix block.

For very early times, i.e., before interference from adjacent sides becomes significant, the extended-square-root model can be simplified to

$$\frac{qt_{cl}}{Q_\infty} = \frac{1}{12}\left[1 + \frac{L_x}{L_y} + \frac{L_x}{L_z}\right]\sqrt{\frac{D_L}{\pi}}\sqrt{\frac{t_{cl}}{t}} \tag{2.2.15}$$

and

$$\frac{Q}{Q_\infty} = \frac{1}{6}\left[1 + \frac{L_x}{L_y} + \frac{L_x}{L_z}\right]\sqrt{\frac{D_L}{\pi}}\sqrt{\frac{t}{t_{cl}}}. \tag{2.2.16}$$

These equations show that for very early times, the thermal conduction rate for multi-dimensional matrix blocks still follows a square root of time behavior. This very early-time behavior will be referred to as the square-root model.

For the case of one-dimensional matrix blocks, e.g., L_y and L_z are much larger than L_x, both the extended-square-root and the square-root models simplify to the one-dimensional models given by Eqs. 2.1.11 and 2.1.12.

2.2.2 Series Solution

A different model can be obtained for the temperature distribution in a three-dimensional matrix block using the method of separation of variables to solve Eq. 2.0.2 (Carslaw and Jaeger, 1959). The geometry used is simultaneous conduction into all six sides of a parallelepiped matrix block having a dimensions L_x, L_y, L_z. The temperature profile for this case is given by

$$T(x,y,z,t) = T_s - \frac{64}{\pi^3}(T_s - T_i)\sum_{l=0}^{\infty}\sum_{m=0}^{\infty}\sum_{n=0}^{\infty}\left[\begin{array}{l}\dfrac{1}{(2l+1)(2m+1)(2n+1)} \\ *\exp\left\{-\left[\dfrac{(2l+1)^2}{L_x^2}+\dfrac{(2m+1)^2}{L_y^2}+\dfrac{(2n+1)^2}{L_z^2}\right]\pi^2\alpha t\right. \\ *\sin\left\{(2l+1)\dfrac{\pi}{L_x}x\right\}\sin\left\{(2m+1)\dfrac{\pi}{L_y}y\right\}\sin\left\{(2n+1)\dfrac{\pi}{L_z}z\right\}\end{array}\right]. \quad (2.2.17)$$

The average temperature is obtained by substituting Eq. 2.2.17 into Eq. 2.2.6:

$$\overline{T} = T_s - \frac{512}{\pi^6}(T_s - T_i)\sum_{l=0}^{\infty}\sum_{m=0}^{\infty}\sum_{n=0}^{\infty}\left[\begin{array}{l}\dfrac{1}{(2l+1)^2(2m+1)^2(2n+1)^2} \\ *\exp\left\{-\left[\dfrac{(2l+1)^2}{L_x^2}+\dfrac{(2m+1)^2}{L_y^2}+\dfrac{(2n+1)^2}{L_z^2}\right]\pi^2\alpha t\right.\end{array}\right]. \quad (2.2.18)$$

The conduction rate is found by substituting Eq. 2.2.18 and 2.1.7 into Eq. 2.2.3:

$$q = \frac{512}{\pi^4}\alpha Q_\infty \sum_{l=0}^{\infty}\sum_{m=0}^{\infty}\sum_{n=0}^{\infty}\left[\begin{array}{l}\dfrac{1}{(2l+1)^2(2m+1)^2(2n+1)^2}\left|\dfrac{(2l+1)^2}{L_x^2}+\dfrac{(2m+1)^2}{L_y^2}+\dfrac{(2n+1)^2}{L_z^2}\right| \\ *\exp\left\{-\left[\dfrac{(2l+1)^2}{L_x^2}+\dfrac{(2m+1)^2}{L_y^2}+\dfrac{(2n+1)^2}{L_z^2}\right]\right|\pi^2\alpha t\end{array}\right], \qquad (2.2.19)$$

Using the characteristic time for multi-dimensional thermal conduction defined by Eq. 2.2.11, the normalized conduction rate can be written as

$$\frac{qt_{cl}}{Q_\infty} = \frac{8L_x^2 D_L}{9\pi^4}\sum_{l=0}^{\infty}\sum_{m=0}^{\infty}\sum_{n=0}^{\infty}\left[\begin{array}{l}\dfrac{1}{(2l+1)^2(2m+1)^2(2n+1)^2}\left|\dfrac{(2l+1)^2}{L_x^2}+\dfrac{(2m+1)^2}{L_y^2}+\dfrac{(2n+1)^2}{L_z^2}\right| \\ *\exp\left\{-\left[\dfrac{(2l+1)^2}{L_x^2}+\dfrac{(2m+1)^2}{L_y^2}+\dfrac{(2n+1)^2}{L_z^2}\right]\right|\dfrac{\pi^2 L_x^2 D_L}{576}\dfrac{t}{t_{cl}}\end{array}\right]. \qquad (2.2.20)$$

The cumulative amount of thermal energy conducted is obtained by integrating Eq. 2.2.20 with respect to time:

$$\frac{Q}{Q_\infty} = \frac{512}{\pi^6}\sum_{l=0}^{\infty}\sum_{m=0}^{\infty}\sum_{n=0}^{\infty}\left[\begin{array}{l}\dfrac{1}{(2l+1)^2(2m+1)^2(2n+1)^2} \\ *\left[1-\exp\left\{-\left|\dfrac{(2l+1)^2}{L_x^2}+\dfrac{(2m+1)^2}{L_y^2}+\dfrac{(2n+1)^2}{L_z^2}\right|\dfrac{\pi^2 L_x^2 D_L}{576}\dfrac{t}{t_{cl}}\right]\right]\end{array}\right]. \qquad (2.2.21)$$

2.2.3 Discussion of Multi-Dimensional Models

In the above sections, two models have been presented for multi-dimensional thermal conduction into a matrix block. These models are based on theoretical solutions for thermal conduction available in the literature (Carslaw and Jaeger, 1959).

The normalized conduction rate and cumulative energy conducted for a cubic matrix block for these two models are compared in Figs. 4 and 5, respectively. The series model is presented for a variety of terms in the infinite series. The number of terms presented, one, eight, 1,331, and 17,576 correspond to including all terms in the infinite series for values of l, m, and n less than or equal to 0, 1, 10, or 25, respectively.

At the very early times, the extended-square-root and square-root models agree with each other. However, at dimensionless times greater than about 0.05, they begin to deviate significantly from each other. This deviation is from the failure of the square-root model to account for interference from adjacent sides of the matrix block. Thus, the square-root model can be considered valid only for dimensionless times less than about 0.05, or for only a very small fraction of the conduction transient. The extended-square-root model is considered accurate through much later times. At dimensionless times greater than about five, the extended-square-root model shows an unrealistic behavior because it (like the square-root model) assumes conduction into a semi-infinite medium and does not account for interference from opposing sides. Neither the extended-square-root or the square-root models are valid during the late conduction times.

The series model is exact during the entire conduction period, as long as a very large number of terms are used. As seen in Fig. 4, over 15,000 terms are required to agree with the square-root models at dimensionless times less than 0.01. At dimensionless times greater than about 1, all of the higher order terms in the series can be neglected for the conduction rate and only one term is required. However, neglecting the higher order terms results in the cumulative energy conducted to be significantly underpredicted. Even including 17,576 terms in the infinite series, there are only enough number of terms to converge to within about 2% of the true value after an infinite conduction time.

These figures, like those for one-dimensional conduction, reveal the inadequacy of these analytical models for the practical modeling of thermal conduction between fractures and matrix blocks. The extended-square-root and the square-root models are impractical because they are only valid during part of the conduction period. The series model is impractical because of the computational requirements of including tens of thousands of terms in the series for convergence.

2.3 Closure

An important step in accurately predicting the performance of geothermal reservoirs is to accurately model the crossflow of thermal energy between the matrix blocks and the fluids in the fractures. There are two classical models for the crossflow of thermal energy that can be obtained from the direct solution of the heat diffusion equation, the square-root and infinite series models. Unfortunately, these models do not provide a practical way to predict the crossflow of thermal energy and are of limited value in predicting the performance of geothermal reservoirs.

In the following section, a number of additional models are developed. These models, originally developed for the mathematically-similar problem of capillary imbibition of water into an oil-saturated, water-wet matrix block, will be rederived for application in predicting heat conduction in fractured geothermal reservoirs.

3.0 New Models For Thermal Conduction

In the previous section, it was demonstrated that the classical solutions to the heat diffusion equation do not yield simple models for the exchange of thermal energy between the matrix and fractures in geothermal flow, and therefore, are not practical for modeling geothermal processes. In this section, new semi-empirical models are presented that overcome some of the limitations of classical models. These new models are based on the mathematically-similar problem of capillary imbibition into water-wet matrix blocks.

When water is injected into a naturally fractured petroleum reservoir having water-wet, petroleum-saturated matrix blocks, the water flowing through the fractures will be spontaneously imbibed into the matrix blocks from capillary pressure. The water saturation (volume fraction of water in the pores) in the matrix block is governed by the following diffusion equation (Handy, 1960; Dutra and Aziz, 1992; Beckner, et al., 1988; Bech, et al., 1991; and Chen, et al., 1995a):

$$\frac{d}{dx}\left[D_i \frac{dS_w}{dx}\right] + \frac{d}{dy}\left\{D_i \frac{dS_w}{dy}\right\} + \frac{d}{dz}\left\{D_i \frac{dS_w}{dz}\right\} = -\phi \frac{dS_w}{dt}, \tag{3.0.1}$$

where S_w is the local water saturation, D_i is the diffusion coefficient defined as

$$D_i = \frac{k \dfrac{k_{rw} k_{ro}}{\mu_w \mu_o} \dfrac{dP_c}{dS_w}}{\left| \dfrac{k_{rw}}{\mu_w} + \dfrac{k_{ro}}{\mu_o} \right|}, \tag{3.0.2}$$

ϕ is the matrix block porosity, k is the absolute permeability, k_{rw} and k_{ro} are the relative permeabilities of the water and oil in the matrix block, respectively, P_C is the capillary pressure between the water and oil, and μ_w and μ_o are the water and oil viscosities, respectively.

For the case of a constant diffusion coefficient, Eq. 3.0.1 simplifies to

$$\frac{d^2 S_w}{dx^2} + \frac{d^2 S_w}{dy^2} + \frac{d^2 S_w}{dz^2} = -\frac{\phi}{D_i} \frac{dS_w}{dt}. \tag{3.0.3}$$

Comparing Eq. 3.0.3 for capillary imbibition to Eq. 2.0.2 for thermal conduction reveals that the two processes are mathematically similar. Because of this similarity, the many models developed for capillary imbibition may be adapted for use in the thermal processes in geothermal reservoirs. The negative sign in the water-saturation diffusion equation arises from assumptions

made in its initial derivation. In particular, the water-flow-rate equation (Darcy's Law) that is analogous to the conduction rate given by Eq. 2.1.4 by convention does not include the negative sign. This different is not significant to this study.

A variety of models for capillary imbibition have been developed. These have been summarized by Reis and Cil, (1999 and 2000). Although these models are semi-empirical, i.e., they are not necessarily rigorous solutions to the diffusion equation, their validity has been verified by comparing them to laboratory data. These models are rederived in the following sections in terms of temperature and heat conduction instead of water saturation and capillary imbibition. These models are then compared to the exact classical equations for heat conduction.

3.1 One-Dimensional Models

In this section one-dimensional models for thermal conduction will be presented that were originally developed for the problem of capillary imbibition. The analysis presented here gives an original derivation of these models in terms of thermal conduction. In some cases, the models have been extended beyond the forms developed for capillary imbibition.

3.1.1 Linear-Temperature-Profile Model

The linear-temperature-profile model is based on the corresponding linear-saturation-profile model first presented by Reis and Cil (1993). In this model, conduction is divided into two periods. During the early-time period, conduction fronts advance into the two opposing faces of the matrix block without being affected by each other, i.e., each is advancing into a semi-infinite medium. During the late-time period, the two conduction fronts have merged and interact with each other. These two time periods are modeled separately.

During the early-time period, the temperature profile is assumed to vary linearly from the surface temperature to the leading edge of the thermal front, which is at the initial temperature. During the late-time period, the temperature is assumed to vary linearly from the surface temperature to the temperature at the matrix block centerline. During the early-time period, conduction occurs through the advance of the thermal front. During the late-time period, conduction occurs through a changing temperature at the matrix block centerline.

Early-Time Period

During the early-time period, this model assumes that the temperature varies linearly from the temperature at the surface of the matrix block to the initial temperature at the leading edge of the thermal front. This temperature profile can be written as

$$T(x) = T_s + (T_i - T_s)\,\frac{x}{L'}\ , \tag{3.1.1}$$

where L' is the distance from the edge of the matrix block to the leading edge of the thermal front.

The heat flow at any point in the matrix block is given by the heat transfer rate equation:

$$q = -KA\frac{dT}{dx}. \tag{3.1.2}$$

Substituting Eq. 3.1.1 into Eq. 3.1.2 yields the following expression for the conduction rate at one face of the matrix block:

$$q = -\frac{KA}{L'}(T_i - T_s). \tag{3.1.3}$$

The cumulative energy conducted into one face of the matrix block during the early-time period is found from an energy balance:

$$Q = \int_0^{L'} \rho c_p (T(x) - T_i) A dx. \tag{3.1.4}$$

Substituting Eq. 3.1.1 into Eq. 3.1.4 and integrating yields the following expression for the cumulative energy conducted into the matrix block:

$$Q = \frac{(T_s - T_i)\rho c_p A L'}{2}. \tag{3.1.5}$$

A second expression for the energy conduction rate into one face of the matrix block can be obtained by differentiating Eq. 3.1.5 with respect to time:

$$q = \frac{(T_s - T_i)\rho c_p A}{2}\frac{dL'}{dt}. \tag{3.1.6}$$

Equating Eqs. 3.1.3 and 3.1.6 and solving the resulting differential equation for the position of the leading edge of the thermal front yields:

$$L' = \sqrt{4\alpha t}. \tag{3.1.7}$$

Substituting Eq. 3.1.7 back into Eq. 3.1.6 yields the following expression for the conduction rate:

$$q = \frac{(T_s - T_i)A\sqrt{K\rho c_p}}{2}\sqrt{\frac{1}{t}}. \tag{3.1.8}$$

The cumulative energy conducted into one face of the matrix block is obtained by integrating Eq. 3.1.8 with respect to time:

$$Q = (T_s - T_i)A\sqrt{K\rho c_p}\sqrt{t}. \tag{3.1.9}$$

The above equations are valid for one-half of the matrix block. Since conduction is assumed to occur into both sides simultaneously, the conduction rate and cumulative energy conducted into the matrix block are twice those values:

$$q = (T_s - T_i)A\sqrt{K\rho c_p}\sqrt{\frac{1}{t}} \tag{3.1.10}$$

and

$$Q = 2(T_s - T_i)A\sqrt{K\rho c_p}\sqrt{t}, \tag{3.1.11}$$

respectively. This square-root-of-time behavior during the early times is similar to that of the classical square-root model described earlier.

A comparison of the conduction rate given by Eq. 3.1.10 to the exact rate given by Eq. 2.1.6 reveals that that the linear-temperature-profile model underpredicts the true heat conduction rate by a factor of $2/\sqrt{\pi} \approx 1.13$. This difference arises because the actual temperature profile is not linear. To match the proper conduction rate, the linear-temperature-profile model, with its

assumed temperature profile, will be adjusted so that the early-time conduction rate matches the true value. This adjustment will be made by simply multiplying Eqs. 3.1.10 and 3.1.11 by a factor of $2/\sqrt{\pi}$:

$$q = \frac{2}{\sqrt{\pi}}(T_s - T_i)A\sqrt{K\rho c_p}\sqrt{\frac{1}{t}} \tag{3.1.12}$$

and

$$Q = \frac{4}{\sqrt{\pi}}(T_s - T_i)A\sqrt{K\rho c_p}\sqrt{t}\,. \tag{3.1.13}$$

This correction can be considered as an increase in the effective thermal diffusivity for this model by a factor of $4/\pi$.

By dividing Equation 3.1.13 by Eq. 2.1.7, the cumulative fraction of energy conducted can be written as

$$\frac{Q}{Q_\infty} = \frac{4}{\sqrt{\pi}}\frac{\sqrt{\alpha}}{L}\sqrt{t}\,. \tag{3.1.14}$$

For the linear-temperature-profile model this cumulative fraction is one-half when the thermal front reaches the centerline, i.e., at the centerline time. The centerline time can be obtained from Eq. 3.1.14 when the thermal front reaches the centerline:

$$\frac{1}{2} = \frac{4}{\sqrt{\pi}}\frac{\sqrt{\alpha}}{L}\sqrt{t_{cl}}\,, \tag{3.1.15}$$

or

$$t_{cl} = \frac{\pi L^2}{64\alpha}\,. \tag{3.1.16}$$

This is the characteristic time used for thermal conduction in Eq. 2.1.10.

Substituting Eqs. 2.1.7 and 3.1.16 into Eqs. 3.1.12 and 3.1.13 yields the following expressions for the normalized conduction rate and cumulative energy conducted:

$$\frac{qt_c}{Q_\infty} = \frac{1}{4}\sqrt{\frac{t_c}{t}} \tag{3.1.17}$$

and

$$\frac{Q}{Q_\infty} = \frac{1}{2}\sqrt{\frac{t}{t_c}}, \tag{3.1.18}$$

respectively. As expected, these equations are identical to the true values given by Eqs. 2.1.11 and 2.1.12, respectively. Thus, the linear-temperature-profile model can accurately represent the early-time period behavior as long as it is modified to reflect the proper conduction rate.

It is noted that an alternate method for calculating the centerline time is to solve Eq. 3.1.7 directly:

$$t_{cl}' = \frac{L^2}{16\alpha}. \tag{3.1.19}$$

This alternate centerline time is longer than that given by Eq. 3.1.16 because it reflects the lower effective conduction rate of the unmodified linear-temperature-profile model. This time will be referred to as the unmodified centerline time, while Eq. 3.1.16 will be referred to as the modified centerline time.

Late-Time Period

During the late-time period of the linear-temperature-profile model, the temperature profile is assumed to remain linear. To account for the changing thermal energy stored in the matrix block, the temperature at the centerline of the matrix block changes with time. The temperature in the remainder of the block decreases in a way to maintain the linear connection between the fixed surface temperature and the changing centerline temperature. This temperature profile for one face of the matrix block is given by

$$T(x) = T_s + (T_{cl} - T_s)\left|\frac{x}{\frac{L}{2}}\right|, \tag{3.1.20}$$

where T_{cl} is the temperature at the centerline of the matrix block and L/2 denotes the half-width of the matrix block, e.g., the centerline.

The cumulative energy conducted into one face of the matrix block during the late-time period (including that conducted during the early-time period) is given by

$$Q = \int_0^{L/2} \rho c_p \left(T(x) - T_i\right) A dx . \tag{3.1.21}$$

Substituting Eqs. 2.1.7 and 3.1.20 into 3.1.21 yields

$$Q = \frac{\rho c_p A L}{2}\left[\left(T_s - T_i\right) - \frac{\left(T_s - T_{cl}\right)}{2}\right]. \tag{3.1.22}$$

The conduction rate can be obtained by differentiating Eq. 3.1.22 with respect to time:

$$q = \frac{dQ}{dt} = \frac{\rho c_p A L}{4}\frac{dT_{cl}}{dt_{late}}, \tag{3.1.23}$$

where t_{late} is the time since the beginning of the late-time period:

$$t_{late} = t - t_{cl} . \tag{3.1.24}$$

The conduction rate can also be obtained from Eq. 3.1.2:

$$q = -KA\frac{\left(T_{cl} - T_s\right)}{\frac{L}{2}}. \tag{3.1.25}$$

Equating Eqs. 3.1.23 and 3.1.25 and solving the resulting differential equation for the temperature at the centerline of the matrix block yields:

$$T_{cl}(t) = T_s + \left(T_i - T_s\right)\exp\left[-\frac{8\alpha}{L^2}\left(t - t_{cl}\right)\right] . \tag{3.1.26}$$

Substituting Eq. 3.1.26 into Eq. 3.1.25 yields the following equation for the conduction rate:

$$q = 2\frac{KA(T_s - T_i)}{L}\exp\left[-\frac{8\alpha}{L^2}(t - t_{cl})\right] \quad . \tag{3.1.27}$$

This is the conduction rate for one-half of the matrix block. The total conduction rate is twice this value. After combining this equation with Eq. 2.1.7, the conduction rate is

$$\frac{q}{Q_\infty} = \frac{4\alpha}{L^2}\exp\left[-\frac{8\alpha}{L^2}(t - t_{cl})\right] \quad . \tag{3.1.28}$$

The cumulative energy conducted into the matrix block is found by integrating Eq. 3.1.28 from the centerline time to the desired time and adding the energy conducted from the early time. After some algebra, this becomes:

$$\frac{Q}{Q_\infty} = 1 - \frac{1}{2}\exp\left[-\frac{8\alpha}{L^2}(t - t_{cl})\right] \quad . \tag{3.1.29}$$

If Eq. 3.1.16 is used to replace the thermal diffusivity with the centerline time, the normalized conduction rate and cumulative energy conducted become

$$\frac{qt_{cl}}{Q_\infty} = \frac{\pi}{16}\exp\left\{-\frac{\pi}{8}\left|\frac{t}{t_{cl}} - 1\right|\right. \tag{3.1.30}$$

and

$$\frac{Q}{Q_\infty} = 1 - \frac{1}{2}\exp\left\{-\frac{\pi}{8}\left|\frac{t}{t_{cl}} - 1\right|\right. \quad , \tag{3.1.31}$$

respectively. These equations are based on the modified centerline time. i.e., a centerline time that is based on modifying the conduction rate during the early-time period to match the exact square-root model.

If the unmodified centerline time is used to eliminate the thermal diffusivity, the normalized conduction rate and cumulative energy conducted become

$$\frac{qt_{cl}'}{Q_\infty} = \frac{1}{4}\exp\left\{-\frac{1}{2}\left(\frac{t}{t_{cl}'} - 1\right)\right\} \tag{3.1.32}$$

and

$$\frac{Q}{Q_\infty} = 1 - \frac{1}{2}\exp\left\{-\frac{1}{2}\left|\frac{t}{t_{cl}'} - 1\right|\right\} \quad . \tag{3.1.33}$$

These two versions of the late-time, linear-temperature-profile model are compared in Figs. 6 and 7, for the normalized conduction rate and cumulative energy conducted, respectively. For Eqs. 3.1.32 and 3.1.33, the dimensionless time is the time divided by the unmodified centerline time, t_{cl}'. These figures show that both versions of the late-time model are very poor during the early-time period, i.e., at dimensionless times less than one. In particular, they show a finite amount of conduction has already occurred at time zero. These figures also show that using the unmodified centerline time, Eq. 3.1.19, provides a better match to the exact series solution during the late-time period than does the model using the modified centerline time, Eq. 3.1.16, which provides a better match during the early-time period. This suggests that the adjustment to the early-time conduction rate equation to match the exact equation may not be appropriate during the late-time period.

Thus, the one-dimensional linear-temperature-profile model that best matches the exact series model is given by Eqs. 3.1.17 and 3.1.18 during the early-time period and by Eqs. 3.1.32 and 3.1.33 during the late-time period. The centerline time, i.e., the time when the early-time ends and the conduction front effectively reaches the centerline of the matrix block is given by Eq. 3.1.16 when using the early-time model and 3.1.19 when using the late-time model. Transition from the early- to the late-time period should be modeled using Eq. 3.1.16, because it yields the best model through the early-time period to transition.

3.1.2 Exponential Model

The exponential model is an empirical fit of a single-term exponential decline to the cumulative energy conducted. The exponential model assumes that the normalized cumulative energy conducted after an infinite time is unity and that the normalized cumulative energy conducted at the centerline time, i.e., the characteristic conduction time, is one-half. This latter assumption is consistent with both the classical models and the linear-temperature-profile model.

The exponential model is expressed as

$$\frac{qt_{cl}}{Q_\infty} = \ln(2)\exp\left\{-\ln(2)\frac{t}{t_{cl}}\right. \tag{3.1.34}$$

and

$$\frac{Q}{Q_\infty} = 1 - \exp\left[-\ln(2)\frac{t}{t_{cl}}\right] \quad , \tag{3.1.35}$$

for the normalized conduction rate and cumulative energy conducted, respectively. The appropriate expression for the characteristic conduction time is given by Eq. 3.1.16.

The exponential model is compared to the infinite series model in Figs. 8 and 9 for the normalized conduction rate and cumulative energy conducted, respectively. From this figure, it can be seen that the exponential model yields a poor match for the conduction rate during the early-time period, but yields a fair match to the cumulative energy conducted over most of the conduction period. This model is superior to the linear-temperature-profile model because it does not predict a finite amount of conduction having already occurred at time zero.

3.1.3 Two-Term Exponential Model

Dutra and Aziz (1992) presented a model for capillary imbibition that is similar to the exponential model presented above, except that they included two exponential terms in their model. They determined the model parameters through a curve fit. After converting their model to the problem of thermal conduction, the normalized conduction rate and cumulative energy conducted become

$$\frac{qt_{cl}}{Q_\infty} = \frac{\pi^3}{128}\left[\xi_1 \exp\left[-\xi_1\frac{\pi^3}{64}\frac{t}{t_{cl}}\right] + \xi_2 \exp\left\{-\xi_2\frac{\pi^3}{64}\frac{t}{t_{cl}}\right\}\right] \tag{3.1.36}$$

and

$$\frac{Q}{Q_\infty} = 1 - \frac{1}{2}\exp\left[-\xi_1\frac{\pi^3}{64}\frac{t}{t_{cl}}\right] - \frac{1}{2}\exp\left\{-\xi_2\frac{\pi^3}{64}\frac{t}{t_{cl}}\right\} \quad , \tag{3.1.37}$$

respectively, with

$$\xi_1 = 0.8147 \tag{3.1.38}$$

and

$$\xi_2 = 2.2910 \quad . \tag{3.1.39}$$

The appropriate expression for the characteristic conduction time is given by Eq. 3.1.16. If Eq. 3.1.36 is evaluated at the characteristic conduction time, the fraction of the total volume imbibed at that time is essentially one-half, a result consistent with the other models.

This model is compared to the infinite series model and to the exponential model in Figs. 8 and 9 for the normalized conduction rate and cumulative energy conducted, respectively. The two-term exponential model predicts provides a better match then the exponential model to the infinite series model during the late-time period and is virtually equal to the exponential model during the early-time period. Judgement is required to determine whether the added computational costs of the two-term exponential model are worth the increased accuracy.

3.1.4 Power-Law Model

A final one-dimensional model developed for capillary imbibition that has potential for use in thermal conduction is the power-law model. In this model, the square-root model is used for the early-time period (a power-law behavior with an exponent of -1/2) and a different power-law is used for the late-time period. The mantissa and exponent for the power-law during the late-time period are obtained from a curve-fit of the exact solution. This approach was originally presented by Chen et al. (1995b) and extended by Reis and Cil (1999) for the problem of capillary imbibition.

During the early-time period, the conduction rate is given by Eq. 2.1.6. The cumulative energy conducted during the early-time period is obtained by integrating this equation over time:

$$Q = 4KA\left(T_s - T_i\right)\sqrt{\frac{1}{\pi\alpha}}\sqrt{t}\,. \tag{3.1.40}$$

During the late-time period, the conduction rate can be modeled as

$$q = 2A\beta t^{-\gamma}\,, \tag{3.1.41}$$

where the 2 denotes conduction into the two opposing faces of the matrix block, A is the area of one of the matrix block faces into which conduction occurs, and β and γ are power-law empirical constants.

If the conduction rate is assumed to be continuous between the early- and late-time periods, i.e., the conduction rates for the two periods are equal at the transition time between the two time periods, the following expression is obtained for the pre-exponential constant β:

$$\beta = \frac{\sqrt{K\rho c_p}\,(T_s - T_i)}{\sqrt{\pi}}\, t_{tr}^{\,\gamma - 1/2}\,, \tag{3.1.42}$$

where t_{tr} is the transition time between the early- and late-time behavior. The difference between the characteristic (centerline) time and the transition time will be discussed below.

The cumulative energy conducted after the transition time is obtained by integrating Eq. 3.1.42 with respect to time and adding the energy conducted during the early-time period:

$$Q = 2A\beta \int_{t_{tr}}^{t} t^{-\gamma} dt + Q_{early}\,, \tag{3.1.43}$$

where Q_{early} is the cumulative energy conducted prior to the transition time. After evaluating, Eq. 3.1.43 becomes

$$Q = 4A \frac{\sqrt{K\rho c_p}}{\sqrt{\pi}} (T_s - T_i) \sqrt{t_{tr}} \left[1 - \frac{1}{2(1-\gamma)} + \frac{1}{2(1-\gamma)} \left| \frac{t}{t_{tr}} \right|^{1-\gamma} \right]. \tag{3.1.44}$$

After noting that $\gamma > 1$, the cumulative energy conducted after an infinite time can be obtained from Eq. 3.1.44:

$$Q_\infty = 4A \frac{\sqrt{K\rho c_p}}{\sqrt{\pi}} (T_s - T_i) \sqrt{t_{tr}} \left| 1 - \frac{1}{2(1-\gamma)} \right|. \tag{3.1.45}$$

The normalized conduction rate during the late-time period is obtained by combining Eqs. 3.1.41, 3.1.42, and 3.1.45:

$$\frac{q t_{tr}}{Q_\infty} = \frac{\left(\frac{t_{tr}}{t} \right)^{\gamma}}{2 \left[1 + \frac{1}{2(\gamma - 1)} \right]}\,. \tag{3.1.46}$$

and the normalized cumulative energy conducted is obtained by combining Eqs. 3.1.44 and 3.1.45:

$$\frac{Q}{Q_\infty} = 1 - \frac{1}{(2\gamma - 1)} \left| \frac{t}{t_{tr}} \right|^{1-\gamma} . \tag{3.1.47}$$

Several versions of the power-law model are possible. First, it will be assumed that transition from the early- to late-time behavior occurs at the centerline time. It will also be assumed that the cumulative fraction of energy conducted at the transition time is one-half. These assumptions match those in the linear-temperature-profile model. Using these assumptions, Eq. 3.1.47 can be evaluated at the centerline time to obtain the late-time exponent, γ:

$$\gamma = \frac{3}{2} . \tag{3.1.48}$$

Substituting Eq. 3.1.48 into Eqs. 3.1.46 and 3.1.47 results in the following power-law model:

$$\frac{q t_{cl}}{Q_\infty} = \frac{1}{4} \left(\frac{t_{cl}}{t} \right)^{\frac{3}{2}} \tag{3.1.49}$$

and

$$\frac{Q}{Q_\infty} = 1 - \frac{1}{2} \left| \frac{t}{t_{cl}} \right|^{-\frac{1}{2}} , \tag{3.1.50}$$

for the normalized conduction rate and cumulative energy conducted, respectively. These equations will referred to as the simple power-law model.

The simple power-law model is compared to the infinite series model in Figs. 10 and 11, for the normalized conduction rate and cumulative energy conducted, respectively. Figure 11 shows that the simple power-law model provides a poor match for the late-time period. From Fig. 10, it can be seen that the conduction rate drops too fast during the initial stages of the late-time period. The true conduction rate, shown by the series model, drops more slowly after the thermal fronts begin to interact at the centerline of the matrix block. Thus, the assumption that transition from early- to late-time behavior occurs when the thermal front arrives at the centerline

of the matrix block is not good. There is a time delay between the arrival of the thermal fronts at the centerline of the matrix block and when this arrival is reflected by the conduction rate into the matrix block at the matrix block surface.

An improved power-law model can be obtained if an empirical relationship between the transition from early-to late-time behavior and the centerline time is obtained. An examination of these models reveals that the following relationship provides a good match to these parameters:

$$t_{tr} = \frac{16}{9} t_{cl} \,, \tag{3.1.51}$$

The normalized fraction of cumulative energy conducted at this transition time can be empirically approximated as two-thirds of that conducted after an infinite time. Using these empirical values, the exponent for the late-time conduction rate becomes

$$\gamma = 2 \tag{3.1.52}$$

and the improved power-law model can be expressed as

$$\frac{q t_{cl}}{Q_\infty} = \frac{16}{27} \left(\frac{t_{cl}}{t} \right)^2 \tag{3.1.53}$$

and

$$\frac{Q}{Q_\infty} = 1 - \frac{16}{27} \left(\frac{t_{cl}}{t} \right) \,, \tag{3.1.54}$$

for the normalized conduction rate and cumulative energy conducted, respectively. In this model, transition from the early-time square-root model to Eqs. 3.1.53 and 3.1.54 occurs at a dimensionless time of 16/9, as given by Eq. 3.1.51. These equations will referred to as the improved power-law model.

The improved power-law model is compared to the infinite series model in Figs. 10 and 11, for the normalized conduction rate and cumulative energy conducted, respectively. It can be seen that the improved power-law model provides a better match to the exact series solution than does the simple power-law model. The improved power-law model, however, still does not accurately predict the late-time behavior. The problem with the power-law model is that the exact late-time behavior does not plot as a straight line on a log-log plot, i.e., it does not have a

power-law behavior. It is noted that for the case of capillary imbibition, the late-time behavior does follow a power-law behavior (Reis and Cil, 1999). A key difference between the capillary imbibition and thermal conduction cases is that the variation in the water-saturation diffusivity with a changing water saturation is significantly greater than the variation in the thermal diffusivity with a changing temperature, particularly near the endpoint conditions found during the late-time period.

3.1.5 Discussion of One-Dimensional Models

In this section, four semi-empirical models for thermal conduction were presented. These models were originally developed for the problem of capillary imbibition into matrix blocks but were adapted for thermal conduction transients. In all cases, the models were rederived from basic principles using an approach that parallels that of the original imbibition problem.

Two of the new models, the exponential and two-term exponential models, are simple curve fits to the exact infinite series model: one model fits a single exponential to the infinite series model and one fits a summation of two exponentials to the infinite series model.

The other two models, the linear-temperature-profile and power-law models, divide the conduction process into two periods. The first period is the early-time or infinite-acting period in which conduction occurs into the two opposing faces of the matrix block as if each face were a semi-infinite material. This early-time period ends when the thermal fronts approach the centerline of the matrix block and begin to interact with each other. The second period is the late-time period that occurs after the two opposing thermal fronts have begun to interact and the conduction behavior deviates from infinite-acting behavior. The time when the behavior changes from early- to late-time behavior differs for the two models.

No single equation provides a good fit to the exact infinite series model (as expressed using 25 terms) over the entire conduction period. The two-equation, linear-temperature-profile model provided the best match if the proper early- and late-time equations are used for their respective periods. Unfortunately, this model may not be practical for geothermal studies because the status of conduction relative to the transition time at every point in the reservoir must be monitored and the equation used for the conduction rate switched at the appropriate time. The power-law model has this same limitation and yielded a worse fit to the infinite series model during the late-time period.

The two exponential models provide the most promise for a general purpose model, although they are not accurate during the very early-time period. During the late-time period,

including two exponential terms resulted in a closer fit to the exact solution. Because the difference between the one- and two-term models may be exaggerated by the logarithmic scale of Figs. 8 and 9, the cumulative energy conducted from these models are compared to the infinite series model in Fig. 12 on a linear scale. Although the two-term exponential model still provides a better fit than the exponential model, it can be seen that there is only a modest difference through the majority of the conduction period.

3.2 Multi-Dimensional Models

In this section, semi-empirical models for multi-dimensional thermal conduction will be presented. Some of these models were first proposed for the related problem of capillary imbibition into water-wet matrix blocks (Reis and Cil, 1999).

3.2.1 Linear-Temperature-Profile Model

The multi-dimensional linear-temperature-profile model is based on the corresponding linear-saturation-profile model first developed by Cil (1992) and reported by Reis and Cil (2000). The linear-saturation-profile model was first presented in its one-dimensional form by Reis and Cil (1993).

In this model, conduction is divided into two periods. During the early-time period, conduction fronts advance simultaneously into all six faces of the parallelepiped matrix block without being affected by the conduction fronts from the opposing sides. Interference from adjacent sides is included in this model, however. This early-time period behavior lasts until the first set of conduction fronts reach the centerline of the matrix block. This first set of conduction fronts will enter the opposing faces of the matrix block that have the smallest spacing between them. During the late-time period, the first set of conduction fronts have merged within the matrix block and interact with each other.

During the early-time period, the temperature profile is assumed to vary linearly from the surface temperature at the edge of the matrix block to the leading edge of the conduction front within the matrix block. The leading edge of the conduction front is at the initial matrix block temperature. During the late-time period, the temperature is assumed to vary linearly from the surface temperature to the temperature at the center of the matrix block. During the early-time period, conduction occurs through the advance of the conduction front. During the late-time period, conduction occurs through a changing temperature at the center of the matrix block.

Early-Time Period

The conduction rate in the x-, y-, and z- directions into a parallelepiped matrix block can be written as

$$q_x = -2KA_x \frac{dT}{dx}, \tag{3.2.1}$$

$$q_y = -2KA_y \frac{dT}{dy}, \tag{3.2.2}$$

and

$$q_z = -2KA_z \frac{dT}{dz}, \tag{3.2.3}$$

respectively, where the 2 in these equations accounts for the two opposing faces allowing conduction in each of the directions, and A_x, A_y, and A_z are the respective areas of the individual matrix block faces.

In this model, the temperature profile varies linearly from the temperature at the surface of the matrix block, T_s, to the initial matrix block temperature, T_i, at the leading edge of the conduction front. The conduction fronts are assumed to advance at the same speed into all faces of the matrix block and are located a distance L' from each face. For the x-direction, this temperature profile can be expressed as

$$T(x) = T_s + (T_i - T_s)\frac{x}{L'} \quad . \tag{3.2.4}$$

The total conduction rate into the matrix block is the sum of the conduction rates in the three orthogonal directions;

$$q = -KA_o \frac{(T_i - T_s)}{L'}, \tag{3.2.5}$$

where A_o is the total surface area of the matrix block,

$$A_o = 2(L_x L_y + L_x L_z + L_y L_z), \tag{3.2.6}$$

and L_x, L_y, and L_z are the matrix block dimensions in the x, y, and z directions, respectively.

The cumulative amount of energy conducted into the matrix block can be found from an energy balance,

$$Q = \int_0^{V'} \rho c_p \left(T(x) - T_i\right) dV, \tag{3.2.7}$$

where V' is the volume of the matrix block between the leading edges of the conduction fronts and the faces of the matrix block. This integral can be rewritten as

$$Q = \int_0^{L'} \rho c_p \left(T(x) - T_i\right) A' \, dx, \tag{3.2.8}$$

where A' is the surface area of a parallelepiped block inside the matrix block that is a distance x from the surface. This internal area can be written as

$$A' = 2\left(L_x - 2x\right)\left(L_y - 2x\right) + 2\left(L_x - 2x\right)\left(L_z - 2x\right) + 2\left(L_y - 2x\right)\left(L_z - 2x\right), \tag{3.2.9}$$

or

$$A' = A_o - 8\left(L_x + L_y + L_z\right)x + 24x^2. \tag{3.2.10}$$

Substituting Eqs. 3.2.4 and 3.2.10 into Eq. 3.2.8 and integrating yields the following expression for the cumulative energy conducted into the matrix block:

$$Q = \rho c_p \left(T_s - T_i\right) \left[\frac{A_o}{2} L' - \frac{4}{3}\left(L_x + L_y + L_z\right) L'^2 + 2L'^3 \right]. \tag{3.2.11}$$

The conduction rate into the matrix block can be obtained by differentiating Eq. 3.2.11 with respect to time:

$$q = \frac{dQ}{dt} = \rho c_p \left(T_s - T_i\right) \left[\frac{A_o}{2} - \frac{8}{3}\left(L_x + L_y + L_z\right) L' + 6L'^2 \right] \frac{dL'}{dt}. \tag{3.2.12}$$

Equating the expressions for the conduction rate given by Eqs. 3.2.5 and 3.2.12 yields the following nonlinear differential equation for the position of the leading edge of the conduction front:

$$\left[\frac{A_o}{2} L' - \frac{8}{3}\left(L_x + L_y + L_z\right) L'^2 + 6L'^3 \right] \frac{dL'}{dt} = \alpha A_o, \tag{3.2.13}$$

where the thermal diffusivity is given by

$$\alpha = \frac{K}{\rho c_p}. \tag{3.2.14}$$

This differential equation can be solved to yield the following quartic expression for the leading edge of the conduction front:

$$t = \frac{1}{4\alpha} L'^2 - \frac{8}{9\alpha A_o}\left(L_x + L_y + L_z\right) L'^3 + \frac{3}{2\alpha A_o} L'^4. \tag{3.2.15}$$

The linear-temperature-profile model given by Eqs. 3.2.12 and 3.2.11, using Eq. 3.2.15 for the position of the conduction front, was scaled by dividing these equations by Eq. 2.1.7. The resulting dimensional plots for the conduction rate and cumulative energy conducted are shown in Figs. 13 and 14 for a cubic matrix block. For comparison, the extended-square-root model scaled in the same way is shown as the exact model. The matrix block was assumed to be 1 meter square and have a thermal diffusivity of 1.5 m^2/s.

These figures show that the linear-temperature-profile model provides an good match to the exact early-time model, although it begins to deviate from the exact model at 10,000 seconds. This is about the time the first conduction fronts reach the center of the matrix block. It can be seen that this multi-dimensional linear-temperature-profile model overpredicts the cumulative energy conducted at the centerline time. It was shown in Section 3.1, however, that the linear-temperature-profile for one-dimensional geometry underpredicted the exact extended-square-root model. A correction factor for this deviation that accounts for the geometry differences will be presented below.

An expression for the time required for the first set of conduction fronts to reach the center of the matrix block for the linear-temperature profile model can also be obtained. To be consistent with the previously reported one-dimensional models, this time will be called the centerline time. If the dimensions are ordered such the L_x is the smallest of the three dimensions, the centerline time can be found from Eqs. 3.2.15 by setting L' equal to $L_x/2$.

The resulting expression for the centerline time is

$$t_{cl} = \frac{L_x^2 D_L}{576\alpha}, \tag{3.2.16}$$

where a dimensionless geometry factor has been defined as

$$D_L = \frac{\left(4L_xL_y + 4L_xL_z + 36L_yL_z - 5L_x^2\right)}{\left(L_xL_y + L_xL_z + L_yL_z\right)}. \tag{3.2.17}$$

This is the expression for the centerline time presented in Eq. 2.2.11 above.

For very early times, i.e., when L' is very small, the position of the conduction front from Eq. 3.2.15 simplifies to

$$L' = \sqrt{4\alpha t}\,. \tag{3.2.18}$$

This expression is equal to the unmodified location of the conduction front in one-dimensional geometry given by Eq. 3.1.7. The difference between Eqs. 3.2.15 and 3.2.18 is from Eq. 3.2.15 allowing interference from adjacent conduction fronts in multi-dimensional imbibition.

The dimensionless location of the conduction front at any time, L'/L_x, can be obtained by substituting Eq. 3.2.16 into Eq. 3.2.15:

$$\frac{t}{t_{cl}} = \frac{144}{D_L}\left|\frac{L'}{L_x}\right|^2 - \frac{512}{D_LA_o}\left(L_x + L_y + L_z\right)L_x\left(\frac{L'}{L_x}\right)^3 + \frac{864L_x^2}{D_LA_o}\left(\frac{L'}{L_x}\right)^4. \tag{3.2.19}$$

The normalized conduction rate is found by combining Eq. 3.2.5 with Eqs. 2.1.7 and 3.2.16:

$$\frac{qt_{cl}}{Q_\infty} = \frac{1}{576}\frac{D_LA_o}{L_yL_z}\frac{L_x}{L'}\,, \tag{3.2.20}$$

where the dimensionless location of the conduction front is given by Eq. 3.2.19.

The normalized cumulative energy conducted can be found by dividing Eq. 3.2.11 by Eq. 2.1.7:

$$\frac{Q}{Q_\infty} = \frac{1}{2}\frac{A_o}{L_yL_z}\left|\frac{L'}{L_x}\right| - \frac{4}{3}\frac{\left(L_x + L_y + L_z\right)L_x}{L_yL_z}\left(\frac{L'}{L_x}\right)^2 + 2\frac{L_x^2}{L_yL_z}\left(\frac{L'}{L_x}\right)^3. \tag{3.2.21}$$

The cumulative energy conducted at the centerline time, i.e., at the end of the early-time period, can be obtained by evaluating Eq. 3.2.21 when the position of the conduction front, L', reaches the minimum matrix block half-width, $L_x/2$:

$$\frac{Q_{early}}{Q_\infty} = \frac{1}{2} + \frac{1}{6}\frac{L_x}{L_y} + \frac{1}{6}\frac{L_x}{L_z} - \frac{1}{12}\frac{L_x^2}{L_y L_z}. \tag{3.2.22}$$

For a one-dimensional matrix block, the cumulative energy conducted at the centerline time is one-half, while for a cubic matrix block the cumulative energy conducted is three-quarters. All other matrix block dimensions will fall between those two extremes.

Unfortunately, the above equations do not match the exact model at the centerline time as shown in Figs. 13 and 14. An improved linear-temperature-profile model can be obtained by adding a correction factor that forces agreement with the exact model. Such a correction factor was obtained by comparing the extended-square-root model evaluated at the centerline time (Eq. 2.2.14) with Eq. 3.2.22. The ratio of the exact normalized cumulative energy conducted at the centerline time to that of the linear-temperature-profile model was correlated to the dimensionless geometry factor given by Eq. 3.2.17 for a wide variety of parallelepiped matrix block shapes. This correction factor is given by the following curve fit of this ratio:

$$C_f = \left.\frac{Q_{exact}}{Q_{linear-temperature-profile}}\right|_{cl} = 1.748\text{x}10^{-4} D_L^{\,2} - 8.812\text{x}10^{-4} D_L + 0.9326 \tag{3.2.23}$$

This curve fit is shown in Fig. 15.

The corrected early-time linear-temperature-profile model can obtained simply by multiplying the expressions for the normalized conduction rate and cumulative energy conducted give above by the correction factor. The corrected normalized conduction rate is

$$\frac{qt_{cl}}{Q_\infty} = \frac{1}{576}\frac{C_f D_L A_o}{L_y L_z}\frac{L_x}{L'}, \tag{3.2.24}$$

and the corrected normalized cumulative energy conducted is

$$\frac{Q}{Q_\infty} = C_f\left[\frac{1}{2}\frac{A_o}{L_y L_z}\left|\frac{L'}{L_x}\right| - \frac{4}{3}\frac{(L_x + L_y + L_z)L_x}{L_y L_z}\left(\frac{L'}{L_x}\right)^2 + 2\frac{L_x^2}{L_y L_z}\left(\frac{L'}{L_x}\right)^3\right|. \tag{3.2.25}$$

The corrected cumulative energy conducted at the centerline time is

$$\frac{Q_{early}}{Q_\infty} = C_F\left|\frac{1}{2} + \frac{1}{6}\frac{L_x}{L_y} + \frac{1}{6}\frac{L_x}{L_z} - \frac{1}{12}\frac{L_x^2}{L_y L_z}\right|. \tag{3.2.26}$$

The corrected early-time, linear-temperature-profile models for the normalized conduction rate are compared to the exact extended square-root models in Figs. 16a through 16c for a one-dimensional slab, a square matchstick, and a cube, respectively. The corresponding cumulative energy conducted is shown in Figs. 17a through 17c, respectively. In all cases, the dimensionless position of the conduction front (L'/L_x) is obtained from Eq. 3.2.19. The exact models are given by the extended-square-root models of Eqs. 2.2.13 and 2.2.14, respectively.

These figures show that the corrected linear-temperature-profile model may provide a slightly better match to the exact model given by the extended-square-root model for dimensionless times less than one.

Late-Time Period

For the late-time period, the temperature profile for the linear-temperature-profile model is given by

$$T(x) = T_s + (T_{cl} - T_s)\left[\frac{x}{\frac{L_x}{2}}\right], \tag{3.2.27}$$

where x is the distance from the surface into the matrix block and $L_x/2$ is the distance from the surface of the matrix block to its center. It is noted that the matrix block dimensions were previously ordered such that L_x is the smallest dimension.

The conduction rate during the late-time period is given by

$$q = -KA_o \frac{(T_{cl} - T_s)}{\frac{L_x}{2}}. \tag{3.2.28}$$

The cumulative energy conducted into the matrix block can be expressed as

$$Q = \int_0^V \rho c_p (T(x) - T_i) dV. \tag{3.2.29}$$

This integral can be rewritten as

$$Q = \int_0^{\frac{L_x}{2}} \rho c_p \left(T(x) - T_i\right) A' \, dx \, . \tag{3.2.30}$$

Substituting Eqs. 3.2.27 and 3.2.10 into Eq. 3.2.30 and integrating yields the following expression for the cumulative energy conducted into the matrix block:

$$Q = \rho c_p \left[\begin{array}{l} \left[\frac{1}{4} A_o \left[T_s - 2T_i + T_{cl} \right] L_x \right. \\ \left. - \left(L_x + L_y + L_z\right)\left(T_s - T_i\right) + \frac{2}{3}\left(L_x + L_y + L_z\right)\left(T_{cl} - T_s\right) L_x{}^2 \right] . \\ \left. + \left[\left(T_s - T_i\right) + \frac{3}{4}\left(T_{cl} - T_s\right) \right] L_x{}^3 \right] \end{array} \right. \tag{3.2.31}$$

The conduction rate can be found by differentiating Eq. 3.2.31 with respect to time:

$$q = \frac{dQ}{dt} = \rho c_p \left[\frac{1}{4} A_o L_x - \frac{2}{3}\left(L_x + L_y + L_z\right) L_x{}^2 + \frac{3}{4} L_x{}^3 \right] \frac{dT_{cl}}{dt} \, . \tag{3.2.32}$$

Equating the conduction rates given by Eqs. 3.2.28 and 3.2.32 yields the following differential equation for the temperature of the centerline of the matrix block:

$$\frac{dT_{cl}}{dt_{late}} + \beta T_{cl} = \beta T_s \, , \tag{3.2.33}$$

where

$$\beta = \frac{2\alpha A_o}{\frac{1}{4} A_o L_x^2 - \frac{2}{3}\left(L_x + L_y + L_z\right) L_x^3 + \frac{3}{4} L_x^4} \tag{3.2.34}$$

and t_{late} is the time since the beginning of the late-time period:

$$t_{late} = t - t_{cl} \, . \tag{3.2.35}$$

This differential equation can be solved for the centerline temperature using the initial condition that the centerline temperature is equal to the initial temperature at the start of the late-time period:

$$T_{cl}(t) = T_s + (T_i - T_s)\exp\{-\beta(t - t_{cl})\}. \tag{3.2.36}$$

Substituting Eq. 3.2.36 into Eq. 3.2.28 yields the following equation for the conduction rate:

$$q = 2\frac{KA_o}{L_x}(T_s - T_i)\exp\{-\beta(t - t_{cl})\}. \tag{3.2.37}$$

The normalized conduction rate can be obtained by combining Eq. 3.2.37 with Eqs. 2.1.7, 3.2.6, 3.2.16, 3.2.17, and 3.2.34:

$$\frac{qt_{cl}}{Q_\infty} = \frac{1}{288}\frac{A_o D_L}{L_y L_z}\exp\left\{\gamma\left|1 - \frac{t}{t_{cl}}\right|\right., \tag{3.2.38}$$

where

$$\gamma = \frac{1}{12}\frac{(4L_xL_y + 4L_xL_z + 36L_yL_z - 5L_x^2)}{(6L_yL_z + L_x^2 - 2L_xL_y - 2L_xL_z)}. \tag{3.2.39}$$

The normalized cumulative energy conducted can be obtained by integrating Eq. 3.2.38 from the centerline time and adding the cumulative energy conducted during the early-time period given by Eq. 3.2.22:

$$\frac{Q}{Q_\infty} = 1 - \frac{Q_{late}}{Q_\infty}\exp\left\{\gamma\left|1 - \frac{t}{t_{cl}}\right|\right., \tag{3.2.40}$$

where

$$\frac{Q_{late}}{Q_\infty} = 1 - \frac{Q_{early}}{Q_\infty} = \frac{1}{2} + \frac{1}{12}\frac{L_x^2}{L_yL_z} - \frac{1}{6}\frac{L_x}{L_z} - \frac{1}{6}\frac{L_x}{L_y}. \tag{3.2.41}$$

Note that the above model uses the uncorrected expression for the cumulative fraction of energy conducted at the centerline time.

If this late-time period model is corrected so that the cumulative energy conducted at the centerline time matches that of the corrected early-time model, the fraction of the cumulative

energy conducted at the centerline time is found from Eq. 3.2.26 instead of 3.2.22. Using this equation, Eq. 3.2.41 can be rewritten as

$$\frac{Q_{late}}{Q_\infty} = 1 - C_F\left[\frac{1}{2} + \frac{1}{6}\frac{L_x}{L_y} + \frac{1}{6}\frac{L_x}{L_z} - \frac{1}{12}\frac{L_x^2}{L_y L_z}\right] \tag{3.2.42}$$

and the cumulative energy conducted is still obtained using Eq. 3.2.40.

The corresponding conduction rate is found by differentiating Eq. 3.2.40 with respect to time:

$$\frac{qt_{cl}}{Q_\infty} = \frac{Q_{late}}{Q_\infty}\gamma \exp\left\{\gamma\left|1 - \frac{t}{t_{cl}}\right|\right. \quad . \tag{3.2.43}$$

The corrected late-time, linear-temperature-profile model for the normalized conduction rate, Eq. 3.2.43, and cumulative energy conducted, Eq. 3.2.40, are compared to the exact infinite-series model in Figs. 18 and 19, respectively, for a cubic matrix block. The infinite-series model is given by Eqs. 2.2.20 and 2.2.21 using 17,576 terms.

Theses figures show that the corrected linear-temperature-profile model provides a modest match to the exact rate and a good match to the cumulative energy conducted model during the late-time period. It is noted that the late-time linear-temperature-profile model does not provide a good model during the early-time period and, as previously indicated, that the series model with only 17,576 terms underpredicts the true late-time behavior by several percent.

3.2.2 Extended One-Dimensional Models

Another approach to modeling the behavior of multi-dimensional conduction is to extend the one-dimensional models using an equivalent matrix block size or a shape factor that corrects the one-dimensional geometry to multiple dimensions. Kuo et al. (1977) reported shape factors and sphericity corrections for transient heat conduction into irregular-shaped rock fragments in an infinite pool of liquid. They assumed a convective heat transfer boundary instead of a step temperature change at the matrix block surface. It is believed that the step change used here more accurately represents fractured geothermal reservoirs because there is no infinitely large pool of water in which convection occurs.

Zimmerman et al. (1990) suggested replacing the matrix block half-width with an equivalent width calculated by the volume to surface area of the block:

$$\frac{L_{eq}}{2} = \frac{V}{A_o}. \tag{3.2.44}$$

For a parallelepiped matrix block, the equivalent width of the matrix block becomes

$$L_{eq} = \frac{1}{\left| \frac{1}{L_x} + \frac{1}{L_y} + \frac{1}{L_z} \right|}. \tag{3.2.45}$$

This equivalent width will be referred to as the geometric equivalent width.

Zhang et al. (1996) proposed replacing the matrix block half-width with the following equivalent width:

$$\frac{L_{eq}}{2} = \frac{1}{\sqrt{\sum_{i=1}^{n} \frac{A_i}{V x_i}}}, \tag{3.2.46}$$

where A_i is the area of the i^{th} matrix block face and x_i is the matrix block half-width associated with that fracture face. For a parallelepiped matrix block, the equivalent width of the matrix block becomes

$$L_{eq} = \frac{1}{\sqrt{\frac{1}{L_x^2} + \frac{1}{L_y^2} + \frac{1}{L_z^2}}}. \tag{3.2.47}$$

This equivalent width will be referred to as the RMS equivalent width.

The extended one-dimensional models can be compared to the multi-dimensional models by inserting the equivalent width into the one-dimensional models. The one-dimensional, early-time square-root model for the conduction rate was given in Eq. 2.1.9 as

$$\frac{q}{Q_\infty} = \frac{2}{\sqrt{\pi}} \frac{\sqrt{\alpha}}{L} \sqrt{\frac{1}{t}}. \tag{3.2.48}$$

Using the geometric equivalent width, the multi-dimensional conduction rate becomes

$$\frac{q}{Q_\infty} = 2\sqrt{\frac{\alpha}{\pi}}\left(\frac{1}{L_x}+\frac{1}{L_y}+\frac{1}{L_z}\right)\sqrt{\frac{1}{t}}\,. \tag{3.2.49}$$

Combining this equation with Eq. 2.1.7 yields the following normalized conduction rate:

$$\frac{qt_{cl}}{Q_\infty} = \frac{1}{12}\sqrt{\frac{D_L}{\pi}}\left(1+\frac{L_x}{L_y}+\frac{L_x}{L_z}\right)\sqrt{\frac{t_{cl}}{t}}\,. \tag{3.2.50}$$

The normalized cumulative energy conducted can be obtained by integrating Eq. 3.2.50:

$$\frac{Q}{Q_\infty} = \frac{1}{6}\sqrt{\frac{D_L}{\pi}}\left(1+\frac{L_x}{L_y}+\frac{L_x}{L_z}\right)\sqrt{\frac{t}{t_{cl}}}\,. \tag{3.2.51}$$

Using the RMS equivalent length, the conduction rate becomes

$$\frac{q}{Q_\infty} = 2\sqrt{\frac{\alpha}{\pi}}\sqrt{\frac{1}{L_x^{\,2}}+\frac{1}{L_y^{\,2}}+\frac{1}{L_z^{\,2}}}\sqrt{\frac{1}{t}}\,. \tag{3.2.52}$$

Combining this equation with Eq. 2.1.7 yields the following normalized conduction rate:

$$\frac{qt_{cl}}{Q_\infty} = \frac{1}{12}\sqrt{\frac{D_L}{\pi}}\sqrt{1+\left|\frac{L_x}{L_y}\right|^{2}+\left(\frac{L_x}{L_z}\right)^{2}}\sqrt{\frac{t_{cl}}{t}}\,. \tag{3.2.53}$$

The normalized cumulative energy conducted can be obtained by integrating Eq. 3.2.53:

$$\frac{Q}{Q_\infty} = \frac{1}{6}\sqrt{\frac{D_L}{\pi}}\sqrt{\frac{1}{L_x^{\,2}}+\frac{1}{L_y^{\,2}}+\frac{1}{L_z^{\,2}}}\sqrt{\frac{t}{t_{cl}}}\,. \tag{3.2.54}$$

These extended one-dimensional models are compared to the exact multi-dimensional conduction rate (given by the extended-square-root model) in Figs. 20 and 21 for the normalized conduction rate and cumulative energy conducted for a cubic matrix block, respectively. From these figures it can be seen that the extended one-dimensional models provide a poor match to the true models. The primary difficulty arises because one-dimensional models, even though

they may use an equivalent width, do not correctly model the interference between the conduction fronts entering the matrix block from adjacent faces.

A more accurate application of the extended one-dimensional models might be to use a spherical one-dimensional model rather than the parallelepiped models used in this study. This approach was not taken because the solution of spherical heat diffusion equation involves an infinite series of complimentary error functions instead of the much simpler exponential functions (Carslaw and Jaeger, 1959). Using complimentary error functions instead of exponential functions would prevent an analytical solution from being obtained for the advance of the thermal front in fracture networks.

3.2.3 Exponential Model

The exponential model is an empirical fit of a single-term exponential function to the cumulative energy conducted. The exponential model assumes that the normalized cumulative energy conducted after an infinite time is unity and that the normalized cumulative energy conducted at the centerline time, i.e., at the time the first conduction front reaches the center of the matrix block, matches that predicted by the linear-temperature-profile model, i.e., Eq. 3.2.22 for the uncorrected linear-temperature-profile model and Eq. 3.2.26 for the corrected model.

The cumulative energy conducted for the exponential model is expressed as

$$\frac{Q}{Q_\infty} = 1 - \exp\left[-\delta \frac{t}{t_{cl}}\right], \tag{3.2.55}$$

where δ is the match constant for multi-dimensional conduction. This constant is given by

$$\delta = \ln\left| \frac{12 L_y L_z}{L_x^2 + 6 L_y L_z - 2 L_x L_y - 2 L_x L_z} \right| \tag{3.2.56}$$

for the uncorrected linear-temperature-profile model and

$$\delta = -\ln\left[1 - C_F \left| \frac{1}{2} + \frac{1}{6}\frac{L_x}{L_y} + \frac{1}{6}\frac{L_x}{L_z} - \frac{1}{12}\frac{L_x^2}{L_y L_z} \right| \right] \tag{3.2.57}$$

for the corrected linear-temperature-profile model.

The conduction rate for the exponential model is the time derivative of Eq. 3.2.55:

$$\frac{qt_{cl}}{Q_\infty} = \delta \exp\left(-\delta \frac{t}{t_{cl}}\right) \quad . \tag{3.2.58}$$

The exponential model is compared to the true multi-dimensional conduction rate (infinite series and extended-square-root models) in Figs. 22 and 23 for the normalized conduction rate and cumulative energy conducted for a cubic matrix block, respectively. These figures show that exponential models provide a poor match to the exact models during the early-time period, but a fair match to the exact cumulative energy conducted during the late-time period. This difference between the corrected and uncorrected models is insignificant and will not be considered further.

3.2.4 Power-Law Model

The power-law model for one-dimensional geometry was presented in Section 3.1.4. It was shown that it did not yield a good model for thermal conduction. Reis and Cil (2000) demonstrated that the power-law model was incomplete in multiple dimensions. This model will not be considered further.

3.2.5 VW-PW Model

Another model for the conduction rate and cumulative energy conducted can be obtained from the assumed temperature of Vinsome and Westerveld (1980). They assumed *a priori* that the temperature profile in a one-dimensional semi-infinite medium can be expressed as

$$T(x,t) - T_i = \left(T_s - T_i + P_1 x + P_2 x^2\right) \exp\left(-\frac{2x}{\sqrt{\alpha t}}\right) \quad , \tag{3.2.59}$$

where P_1 and P_2 are time-dependent parameters.

Pruess and Wu (1993) presented a method to extend this model to three-dimensional geometries. This combined model, the VW-PW model, was published for use in a finite-

difference, numerical simulator and was not presented in an analytical form. Pruess and Wu reported that the numerical form of this model was in good agreement with the exact solution.

The derivation of this model in analytical form is outlined below.

The conduction rate for this model is found by inserting Eq. 3.2.59 into the conduction rate equation and evaluating it at the matrix block surface:

$$q = -KA_o \left.\frac{dT}{dx}\right|_{x=0}, \tag{3.2.60}$$

or after substituting,

$$q = -KA_o \left[P_1 - 2\frac{(T_s - T_i)}{\sqrt{\alpha t}} \right]. \tag{3.2.61}$$

The cumulative energy conducted is found by integrating Eq. 3.2.61 over time. In this model x represents the distance from any point within the matrix block to the nearest surface.

To complete this model, an expression for P_1 must be obtained. If a material balance is applied to a one-dimensional, differential, matrix block element that has a variable area in the direction of conduction, the following differential equation can be obtained for the temperature in the block:

$$\frac{\partial T}{\partial t} = \alpha \frac{\partial^2 T}{\partial x^2} + \alpha \frac{\partial \ln(A')}{\partial x} \frac{\partial T}{\partial x}, \tag{3.2.62}$$

where A' is the cross sectional area of the matrix block a distance x from the surface of the matrix block. For the parallelepiped matrix blocks considered here, this area is given by Eq. 3.2.10. Making the appropriate substitutions yields a relatively complex linear equation for P_1 and P_2, the two unknowns in the assumed temperature profile.

A second relationship between P_1 and P_2 can be obtained from a material balance on the entire matrix block. The time derivative of the cumulative energy conducted is equal to conduction rate into the matrix block. Using the cumulative energy conducted given by Eq. 3.2.8, this energy balance can be written as

$$\frac{dQ}{dt} = \frac{d}{dt} \int_0^{\frac{L_x}{2}} \rho c_p (T(x) - T_i) A' dx = -KA_o \left.\frac{dT}{dx}\right|_{x=0}. \tag{3.2.63}$$

Making the appropriate substitutions yields a second complex linear equation for P_1 and P_2.

Equations 3.2.62 and 3.2.63 can be solved to obtain algebraic expressions for both P_1 and P_2. These expressions are very complex functions of time that involve products of various fractional polynomials of time with the exponentiation of the inverse square-root-of-time. The complexity of these functions make them impractical for use in analytical reservoir modeling. This model will not be considered further.

3.2.6 Discussion of Semi-Empirical Models

In this report, several semi-empirical models for thermal conduction were presented. Most of these models were originally developed for the problem of capillary imbibition into matrix blocks but were adapted for thermal conduction transients. These models were rederived from basic principles using an approach that parallels that of the original imbibition problem. In some cases, the models were extended beyond those for imbibition.

The linear-temperature-profile model divides the conduction process into two periods. The first period is the early-time or infinite-acting period in which conduction occurs into all six faces (eight corners) of the parallelepiped matrix block as if each of the corners was a semi-infinite material. This early-time period ends when the thermal fronts from the opposing faces having the closest spacing approach the centerline of the matrix block and begin to interact with each other. The second period is the late-time period that occurs after those thermal fronts have begun to interact and the conduction behavior deviates from infinite-acting behavior. The extended one-dimensional model is a one-dimensional model that uses an equivalent matrix block size to account for the three-dimensional geometry. This model has the same functional form as the one-dimensional model. The exponential model is a simple curve fit to the linear-temperature-profile model. The match point for the curve fit is the cumulative energy conducted at the centerline time.

No single equation provided a good fit over the entire conduction period. The early-time linear-temperature-profile model was in excellent agreement with the exact early-time extended-square-root model. The late-time linear-temperature-profile model provided a fair fit to the series model during the late-time period. Unfortunately, this model may not be practical for geothermal studies because the status of conduction relative to the transition time at every point in the reservoir must be monitored and the equation used for the conduction rate switched at the appropriate time. The extended one-dimensional model provided a poor fit to the exact models, primarily because they did not account for interference between adjacent conduction fronts. The

exponential model provided the best overall fit with a single equation to the exact model for the cumulative energy conducted over the entire conduction period.

Because the difference between the exponential and exact models may be exaggerated by the logarithmic scale of Figs. 22 and 23, the cumulative energy conducted from these models are compared in Fig. 24 on a linear scale. The exponential model predicts a cumulative energy conducted that is too low during the early-time period, i.e., a dimensionless time less than one, and too high during the late-time period, but matches the exact model at a dimensionless time equal to one. The effect of these deviations in reservoir models is expected to be minor as long as conduction comes to completion in parts of the reservoir because they will balance out.

In summary, the exponential model provides the greatest promise for a general purpose conduction model for geothermal reservoirs when conduction is expected to come to completion in at least some parts of the reservoir. The extended-square-root model is the best model to use before conduction comes to completion .

4.0 Review of Existing Thermal Advance Models

In this section, existing analytical models for the advance of thermal fronts in geological formations are reviewed. In these models, water at one temperature is injected into a geologic layer having a different temperature. Thermal conduction from the permeable layer to the impermeable overburden or matrix blocks is included. These models have been grouped into three types. First are models for water injection into a single layer, second are models for water injection into a fracture network, and third are models involving steam injection instead of water.

4.1 Water Injection into Single Layer

The first model for the advance of a thermal front through a geological formation was presented by Lauwerier (1955). The geometry for this model is shown in Fig. 25. He assumed that the initial reservoir temperature was zero and referenced his model to that condition.

If an energy balance is conducted on the shaded region in the permeable layer, shown in Fig. 25, the following equation can be obtained:

$$-\mathrm{Vel}_w \frac{L_f}{2}\rho_w c_w \frac{dT_f}{dx} + K_m \left.\frac{dT_m}{dy}\right|_{y=\frac{L_f}{2}} = \frac{L_f}{2}\rho_f c_f \frac{dT_f}{dx} \quad , \tag{4.1.1}$$

where the first term is the net thermal energy carried into the shaded region from the flow of hot water, the second term is the thermal energy conducted out of the region into the overburden, and the term on the right-hand-side is the change in thermal energy stored in the shaded region. In this equation, it is assumed that the local water temperature in the permeable layer is equal to the local rock temperature, $T_w=T_f$. It is also assumed that the thermal properties of the underburden are the same as those of the overburden to allow for a symmetry boundary condition along the centerline of the permeable layer and that there is no vertical variation in temperature within the permeable layer.

If a similar energy balance is applied to the layer immediately above the shaded region, the following equation is obtained:

$$K_m \frac{d^2 T_m}{dy^2} = \rho_m c_m \frac{dT_m}{dt} \quad . \tag{4.1.2}$$

If the following dimensionless variables are defined,

$$x_D = \frac{K_m}{\frac{L_f}{2}^2 \rho_w c_w Vel_w} x \quad , \tag{4.1.3}$$

$$y_D = y\frac{2}{L_f} \quad , \tag{4.1.4}$$

and

$$t_D = \frac{K_m}{\frac{L_f}{2}^2 \rho_f c_f} t \quad , \tag{4.1.5}$$

Eq. 4.1.2 can be written as

$$\frac{\rho_f c_f}{\rho_m c_m} \frac{d^2 T_m}{dy_D^2} = \frac{dT_m}{dt_D} \quad , \tag{4.1.6}$$

and Eq. 4.1.1 can be written as

$$-\frac{dT_f}{dx_D} + \left.\frac{dT_m}{dy_D}\right|_{y_D=1} = \frac{dT_f}{dt_D} \quad . \tag{4.1.7}$$

Because T_f=T_m along the edge of the permeable formation, Eq. 4.1.7 can be written as

$$-\frac{dT_m}{dx_D} + \frac{dT_m}{dy_D} = \frac{dT_m}{dt_D} \quad . \tag{4.1.8}$$

The initial condition on these equations is as follows:

$$T_f = T_m = T_{inj}, \; x_D<0 \tag{4.1.9}$$

and

$$T_f = T_m = T_i \; x_D >0. \tag{4.1.10}$$

Lauwerier solved these equations for the temperature difference between the overburden, T_m, and the injected water, T_{inj} using Laplace transforms. He first took the Laplace transformation with respect to x_D and then took the transformation with respect to t_D. He reported the following equations after these transformations:

for the overburden,

$$\frac{\rho_f c_f}{\rho_m c_m}\frac{d^2\theta}{dy_D^2} = s\theta - \frac{T_{inj}}{p} \quad , \tag{4.1.11}$$

and for the permeable layer,

$$(p+s)\theta - \frac{d\theta}{d\eta} - \frac{T_{inj}}{p} = 0 \quad , \tag{4.1.12}$$

where p and s are the Laplace transform variables for x_D and t_D, respectively, and θ is the transformed temperature difference.

Lauwerier reported the following solution to these equations:

for the overburden,

$$T_m = T_{inj}\,\mathrm{erfc}\left[\frac{x_D + |y_D| - 1}{2\sqrt{\frac{\rho_f c_f}{\rho_m c_m}(t_D - x_D)}}\right] U(t_D - x_D) \quad , \tag{4.1.13}$$

and for the permeable layer,

$$T_m = T_{inj}\,\mathrm{erfc}\left\{\frac{x_D}{2\sqrt{\frac{\rho_f c_f}{\rho_m c_m}(t_D - x_D)}}\right\} U(t_D - x_D) \quad , \tag{4.1.14}$$

where $U(t_D\text{-}x_D)$ is the unit step function that is zero for $t_D\text{-}x_D$ less than one and unity if greater than one.

This approach cannot be used directly for flow in fractures because the formulation of these equations does not allow the permeable layer thickness to go to zero. An alternative way of

modeling fractures with the Lauwerier model is to maintain a finite layer thickness, but assume that the heat capacity of that layer is zero, i.e., c_f is zero. Under this assumption, Eq. 4.1.14 can be written as

$$T_m = T_{inj}\,\mathrm{erfc}\,\frac{K_m}{L_f \rho_w c_w (Vel)_w \sqrt{\alpha_m t}}\,x \quad . \tag{4.1.15}$$

Bodvarsson (1969) extended the model of Lauwerier (1955) to allow for a sinusoidal temperature distribution for the injected water.

4.2 Water Injection into Fracture Network

Models for the advance of a thermal front in a network of parallel fractures were presented by Gringarten et al. (1975), Bodvarsson and Tsang (1982), and Satman (1988). They extended the model of Lauwerier to finite sizes matrix blocks by imposing a symmetry boundary condition at the matrix block midpoint, e.g., the temperature gradient was assumed to be zero at the midpoint between two parallel fractures. They obtained solutions in Laplace space, but were unable to analytically invert them into the time domain. Analytical and numerical solutions obtained during the early-time period, i.e., before the effects of finite fracture spacing became apparent, agreed with the Lauwerier solution. The numerical solutions were obtained using the Stehfest algorithm (1970).

A different modeling approach was taken by Moody and Horne (1988). They assumed an equivalent porous media model. The effects of the matrix on the fracture temperatures were modeled as a source-sink term using pseudo steady-state conduction with the lumped-capacitance approach. They assumed an equivalent temperature for the matrix and an effective heat transfer coefficient between the matrix and fractures.

Moody and Horne applied an energy balance to the fracture network and obtained the following equation for radial flow:

$$-\rho_w c_w \dot{V}_w \frac{dT_w}{dr}\Delta r - hA\left(T_w - T_m\right) = \rho_w c_w V_w \frac{dT_w}{dt} \quad . \tag{4.2.1}$$

The corresponding energy balance for the matrix blocks can be expressed as

$$hA(T_w - T_m) = \rho_m c_m V_m \frac{dT_m}{dt} \quad . \tag{4.2.2}$$

The initial condition for this model is that the reservoir and fluid are at a temperature of T_i at the start of injection. The boundary condition at the injection well is the temperature of the injected water is $T_{inj.}$.

The total volume of a differential element is given by

$$V_e = 2\pi r \Delta r H \quad , \tag{4.2.3}$$

where r is the radius from the injection well and H is the height of the element. The fluid element is large enough to contain both fractures and matrix blocks. For one-dimensional radial flow, H is also the reservoir thickness. The fluid and rock volumes are given by

$$V_w = \phi_f V_e \quad , \tag{4.2.4}$$

and

$$V_m = (1 - \phi_f) V_e \quad , \tag{4.2.5}$$

respectively, where ϕ_f is the fracture porosity of the element (as a fraction of the element bulk volume).

The effective area for heat transfer can be written as

$$A = \frac{2V_w}{L_f} \quad . \tag{4.2.6}$$

Using these relationships, Moody and Horne defined the following dimensionless parameters:

$$\eta = \frac{\phi_f}{1 - \phi_f} \quad , \tag{4.2.7}$$

$$M_D = \frac{\rho_w c_w \eta}{\rho_m c_m} \quad , \tag{4.2.8}$$

$$t_D = \frac{2h\eta t}{\rho_m c_m L_f} \quad , \tag{4.2.9}$$

$$r_D = \frac{r}{r_w} \quad , \tag{4.2.10}$$

$$V_D = \frac{2\pi H r_w^2 \left(r_D^2 - 1\right) h \phi_f}{L_f \rho_f c_f V_w} \quad , \tag{4.2.11}$$

$$\tau_w = \frac{T_w - T_i}{T_{inj} - T_i} \quad , \tag{4.2.12}$$

$$\tau_m = \frac{T_m - T_i}{T_{inj} - T_i} \quad , \tag{4.2.13}$$

and

$$t_D^* = T_D - M_D V_D \quad . \tag{4.2.14}$$

Using these definitions, Moody and Horne reported the following solutions to the governing differential equations:

For $\frac{V_D}{t_D^*} < 1$,

the dimensionless rock temperature is given by

$$\tau_m = U\left(t_D^*\right)\left[1 - \exp\left\{-\left(V_D + t_D^*\right)\right\}\sum_{k=0}^{\infty} \left|\sqrt{\frac{V_D}{t_D^*}}\right|^k I_k\left(2\sqrt{V_D t_D^*}\right)\right| \tag{4.2.15}$$

and the dimensionless water temperature is given by

$$\tau_w = U\left(t_D^*\right)\left[1 - \exp\left\{-\left(V_D + t_D^*\right)\right\}\sum_{k=1}^{\infty} \left|\sqrt{\frac{V_D}{t_D^*}}\right|^k I_k\left(2\sqrt{V_D t_D^*}\right)\right| \quad , \tag{4.2.16}$$

where I_k is a modified Bessel function of the first kind and of order k.

For $\frac{V_D}{t_D^*} > 1$,

the dimensionless rock temperature is given by

$$\tau_m = U\left(t_D^*\right)\left[1-\exp\left\{-\left(V_D+t_D^*\right)\right\}\sum_{k=1}^{\infty}\left|\sqrt{\frac{V_D}{t_D^*}}\right|^{-k} I_k\left(2\sqrt{V_D t_D^*}\right)\right| \tag{4.2.17}$$

and dimensionless the water temperature is given by

$$\tau_w = U\left(t_D^*\right)\left[1-\exp\left\{-\left(V_D+t_D^*\right)\right\}\sum_{k=0}^{\infty}\left(\sqrt{\frac{V_D}{t_D^*}}\right)^{-k} I_k\left(2\sqrt{V_D t_D^*}\right)\right| \quad . \tag{4.2.18}$$

This model has several important limitations. The authors did not provide a method for determining the effective matrix temperature or heat transfer coefficient, making it difficult to convert the solution from dimensionless parameters to dimensional parameters. Further, the solution is given in terms of an infinite series of Bessel functions. This limits the practicality of the method.

4.3 Steam Injection

Marx and Langenheim (1959) presented a model for the location of a thermal front during steam injection. They assumed injection into a single layer and conduction into the semi-infinite overburden and underburden. Their model geometry is essentially the same at that of Lauwerier (1955). A key difference between the two approaches is that Marx and Langenheim assumed a step change in temperature at the thermal front from the initial formation temperature to the injected fluid temperature, while Lauwerier allowed the temperature to vary gradually with distance from the injection well.

An energy balance on the permeable layer yields the following equation:

$$h_{inj} = 2\int_0^t \frac{K_m \Delta T}{\sqrt{\pi \alpha_m (t-\tau)}}\frac{dA}{d\tau}d\tau + \rho_f c_f L_f \Delta T \frac{dA}{dt} \quad , \tag{4.3.1}$$

where h_{inj} is the enthalpy injection rate, α is the thermal diffusivity of the overburden and underburden, τ is the time when the thermal front reaches dA, and ΔT is the difference between

the initial formation temperature and that of the injected steam. The integral is the conductive heat loss to the overburden and underburden and the square-root form of the integrand arises from the assumption of one-dimensional conduction into a semi-infinite medium, i.e., Eq. 2.1.11.

Marx and Langenheim solved Eq. 4.3.1 using Laplace transforms and obtained the area of the thermal zone:

$$A(t) = \frac{h_{inj}\rho_f c_f L_f \alpha}{4K_m^2 \Delta T}\left[\exp\{u^2\}\operatorname{erfc}\{u\} + \frac{2u}{\sqrt{\pi}} - 1\right] , \tag{4.3.2}$$

where

$$u = \frac{2K_m}{\rho_f c_f L_f \sqrt{\alpha}}\sqrt{t} , \tag{4.3.3}$$

As shown by Hearn (1969), Eq. 3.3.2 can be simplified for flow in a fracture where L_f goes to zero:

$$A(t) = \frac{h_{inj}\sqrt{\alpha}}{\sqrt{\pi} k_m \Delta T}\sqrt{t} . \tag{4.3.4}$$

Closmann (1967) extended the approach of Marx and Langenheim (1959) to allow for a finite fracture spacing of parallel fractures. He assumed an infinite-series model for the conduction rate into the overburden and underburden instead of the square-root model for conduction into a semi-infinite medium assumed by Marx and Langenheim. The resulting area of the thermal zone for this model is given by

$$A(t) = \frac{h_{inj} L \rho_m c_m}{\rho_f c_f K_m \Delta T}\left[\frac{K_m t}{\rho_m c_m L^2 \left| 1 + \dfrac{L\rho_m c_m}{L_f \rho_f c_f} \right|} + \frac{L\rho_m c_m}{12 L_f \rho_f c_f \left(1 + \dfrac{L\rho_m c_m}{L_f \rho_f c_f}\right)^2} - \frac{1}{2}\sum_{n=1}^{\infty} \frac{\exp\left\{-\dfrac{2\gamma_n^2 K_m t}{\rho_m c_m L^2}\right\}}{\gamma_n^2 J_n}\right] , \tag{4.3.5}$$

where

$$J_n = \gamma_n^2 \frac{L_f \rho_f c_f}{L \rho_m c_m} + 1 + \frac{L\rho_m c_m}{L_f \rho_f c_f} \tag{4.3.6}$$

and γ_n's are the roots of the following equation:

$$\gamma + \frac{L\rho_m c_m}{L_f \rho_f c_f} \tan\gamma = 0 \quad . \tag{4.3.7}$$

For the case of the thermal zone being a fracture having a negligible thermal capacity, the heated area is given by

$$A(t) = \frac{h_{inj}}{\rho_m c_m L \Delta T}\left[t + \frac{L^2 \rho_m c_m}{2\pi^2 K_m} \sum_{n=1}^{\infty} \frac{1}{n^2}\left(1 - \exp\left(-\frac{4n^2\pi^2 K_m t}{\rho_m c_m L^2} \right) \right) \right] \quad . \tag{4.3.8}$$

Because this model is based on an infinite series and requires the use of a root finding algorithm, it is not practical for reservoir modeling.

4.4 Discussion of Existing Models

Although the previous studies have provided valuable models that are applicable to geothermal reservoirs, these models have limitations. The models of Lauwerier and of Marx and Langenheim are limited to cases where conduction is from a single heated fracture into a semi-infinite medium. The model of Moody and Horne is too complex for practical application and requires an unknown effective matrix block temperature and heat transfer coefficient. For the case of finite-sized matrix blocks, Closmann's model was the only one in which the extent of the thermal zone could be analytically calculated. Unfortunately, that model required the use of an infinite series.

From this review of existing technology the following conclusion can also be made: no analytical models exist that incorporate multi-dimensional effects of real fracture networks and fracture spacing distributions on the crossflow of heat between the matrix blocks and fractures.

5.0 New Models for Thermal Advance

In this section, new methods for modeling the advance of a thermal front in a fractured geothermal reservoir will be developed. This analysis parallels that of Marx and Langenheim (1959), but is generalized to allow multiple matrix domains having different matrix block sizes and shapes, as well as and different matrix-fracture crossflow conduction rate models.

The new models for the advance of a thermal front in a geothermal reservoir are based on an energy balance on the water injected into the fractures. The enthalpy of the injected water is modeled as either being lost to the formation matrix by conduction or as advancing the boundary of the heated zone. Two geometries are considered for the formation matrix blocks. First is a one-dimensional geometry consisting of a single fracture or set of parallel fractures. Second is a multi-dimensional geometry consisting of an interconnecting fracture network with parallelepiped matrix blocks. For each of these geometries, conduction models for the early- and late-time periods will be used.

5.1 One-Dimensional Geometry

The new models for the advance of thermal fronts in geothermal reservoirs are based on an energy balance on the injected water. This energy balance can be written as

$$h_{inj} = q_{acc} + q_{loss} \quad , \tag{5.1.1}$$

where h_{inj} is the enthalpy injection rate into the high-permeability layer (fracture), q_{acc} is the rate at which energy accumulates in the permeable layer, and q_{loss} is the sum of the energy loss rates to the two adjacent layers from thermal conduction. The geometry for the one-dimensional case is shown in Fig. 26.

The rate at which energy accumulates in the permeable layer can be expressed by

$$q_{acc} = L_f \rho_f c_f (T_w - T_i) \frac{dA}{dt} = L_f \rho_f c_f \Delta T \frac{dA}{dt} \quad , \tag{5.1.2}$$

where L_f is the thickness of that layer or aperture if it is a fracture, $\rho_f c_f$ is the volumetric heat capacity of the layer, T_w is the local water temperature, T_i is the initial temperature of the formation, and A is the areal coverage of the advancing thermal front (the contact area of the hot

zone with one of the adjacent layers). Piston-like advance of the thermal front in the permeable layer is assumed. It is also assumed that the local layer temperature is equal to the local water temperature.

The rate of energy loss to the two adjacent layers is given by

$$q_{loss} = \int_0^{A(t)} q_{A,1}(t-\tau)\, dA + \int_0^{A(t)} q_{A,2}(t-\tau)\, dA \quad , \tag{5.1.3}$$

where $q_{A,1}$ and $q_{A,2}$ are the local conduction fluxes (energy conduction per unit surface area) into layers 1 and 2, respectively, and τ is the time when the thermal front in the permeable layer passes the local area dA.

Substituting Eqs. 5.1.2 and 5.1.3 into Eq. 5.1.1 yields the following integro-differential equation for the areal coverage of the thermal front in the high permeability layer (fracture):

$$h_{inj} = L_f \rho_f c_f \Delta T \frac{dA}{dt} + \int_0^{A(t)} q_{A,1}(t-\tau)\, dA + \int_0^{A(t)} q_{A,2}(t-\tau)\, dA \quad . \tag{5.1.4}$$

Converting Eq. 5.1.4 from integrals over area to integrals over time yields

$$h_{inj} = L_f \rho_f c_f \Delta T \frac{dA}{dt} + \int_0^{t} q_{A,1}(t-\tau)\, \frac{dA}{d\tau}\, d\tau + \int_0^{t} q_{A,2}(t-\tau)\, \frac{dA}{d\tau}\, d\tau \quad . \tag{5.1.5}$$

If the area in Eq. 5.1.5 is replaced with the layer width or fracture height, H, times the penetration distance of the water front in the high-permeability layer, X(t), i.e.,

$$A(t) = HX(t), \tag{5.1.6}$$

that equation can be written in terms of the penetration distance of the thermal front in the fracture:

$$h_{inj} = HL_f \rho_f c_f \Delta T \frac{dX}{dt} + H \int_0^{t} q_{A,1}(t-\tau)\, \frac{dX}{d\tau}\, d\tau + H \int_0^{t} q_{A,2}(t-\tau)\, \frac{dX}{d\tau}\, d\tau \quad . \tag{5.1.7}$$

For the case of the fracture aperture being very small and the energy accumulating in the fracture being negligible, the first term on the right-hand side of Eq. 5.1.7 can be deleted and the equation for the position of the thermal front in the fracture is

$$h_{inj} = H \int_0^t q_{A,1}(t-\tau)\,\frac{dX}{d\tau}\,d\tau + H \int_0^t q_{A,2}(t-\tau)\,\frac{dX}{d\tau}\,d\tau \quad . \tag{5.1.8}$$

The location of the thermal front in the fracture can be obtained by solving Eq. 5.1.7 or 5.1.8 for X(t) after a suitable expression for the conduction rate per unit area has been selected.

5.1.1 Early-Time Period

For the early-time period, i.e., for the case when the thermal front in the matrix does not reach the centerline of the matrix block before the thermal front in the permeable layer reaches the production well, the conduction rate per unit area from the permeable layer into the impermeable matrix can be obtained from Eq. 2.1.11. The conduction rate into one face along the fracture is one-half of that given by that equation. This conduction rate per unit area into one face is given by

$$q_A = \frac{q}{dA} = \frac{q}{Hdx} = \frac{V_m \rho_m c_m \Delta T}{8 t_{cl} H dx} \sqrt{\frac{t_{cl}}{t}}\,, \tag{5.1.9}$$

where the subscript m refers to the matrix properties. For this model, the one-dimensional time for the conduction front to reach the center of the matrix is given by Eq. 2.1.10. The volume of the matrix block is given by

$$V_m = H L_m dx\,. \tag{5.1.10}$$

Substituting Eq. 5.1.9 into Eq. 5.1.7 and solving for X(t) using Laplace transforms yields the following expression for the position of the water front in the fracture:

$$X(t) = \frac{h_{inj}}{m^2 L_f H \rho_f c_f \Delta T}\left[\exp\{m^2 t\}\,\mathrm{erfc}\{m\sqrt{t}\} + \frac{2}{\sqrt{\pi}}\,m\sqrt{t} - 1\right], \tag{5.1.11}$$

where

$$m = \frac{\sqrt{\pi}\,(\beta_1 + \beta_2)}{L_f \rho_f c_f \Delta T}\,, \tag{5.1.12}$$

$$\beta_1 = \frac{L_1 \rho_1 c_1 \Delta T}{8\sqrt{t_{cl,1}}}, \tag{5.1.13}$$

and

$$\beta_2 = \frac{L_2 \rho_2 c_2 \Delta T}{8\sqrt{t_{cl,2}}}, \tag{5.1.14}$$

where the subscripts 1 and 2 refer to the matrix properties of the two layers adjacent to the permeable layer.

For the case of the permeable layer being a fracture and its aperture going to zero, Eq. 5.1.11 simplifies to:

$$X(t) = \frac{2h_{inj}}{\pi H(\beta_1 + \beta_2)}\sqrt{t}, \tag{5.1.15}$$

Alternatively, an expression for the position of the water front in a fracture can be found by substituting Eq. 5.1.9 into Eq. 5.1.8 and solving for X(t):

$$X(t) = \frac{2h_{inj}}{\pi H(\beta_1 + \beta_2)}\sqrt{t}. \tag{5.1.16}$$

This latter approach yields the same result as including the accumulation term in the permeable layer in the original solution and taking the limit as the formation thickness goes to zero.

If the matrices on the two sides of the fracture have the same properties, Eqs. 5.1.15 and 5.1.16 simplify to

$$X(t) = \frac{h_{inj}}{\sqrt{\pi} H \sqrt{\alpha \rho_m c_m \Delta T}}\sqrt{t}. \tag{5.1.17}$$

Although these models have been written in terms of the matrix block thicknesses, those thicknesses cancel algebraically, as they must in the early-time, infinite-acting period. The matrix block thicknesses were left in the models to allow for an easier comparison with the late-time models discussed below.

This early-time model is similar to the previously discussed model of Marx and Langenheim (1959) and of Hearn (1969). It differs only in that it allows different thermal

properties on either side of the permeable layer. For the case of identical properties on either side, this model is identical to that those models.

5.1.2 Late-Time Period

For the late-time period, i.e., for the case when the conduction front in the matrix reaches the centerline of the matrix blocks before the thermal front in the permeable layer reaches the production well, the conduction rate per unit area of permeable layer face can be obtained from Eqs. 3.1.34. Unlike the early-time period, the thicknesses of the two matrix layers adjacent to the permeable layer are important during the late-time period and must be accounted for.

The conduction rate per unit area is given by

$$q_A = \frac{q}{dA} = \frac{\ln(2)}{2}\frac{Q_\infty}{t_{cl}dA}\exp\left\{-\ln(2)\frac{t}{t_{cl}}\right\}. \tag{5.1.18}$$

Substituting for Q_∞ from Eq. 2.1.7 yields

$$q_A = \frac{q}{dA} = \frac{\ln(2)}{2}\frac{L_m\rho_m c_m \Delta T}{t_{cl}}\exp\left[-\ln(2)\frac{t}{t_{cl}}\right]. \tag{5.1.19}$$

Substituting Eq. 5.1.19 into Eq. 5.1.7 and solving for X(t) using Laplace transforms yields the following expression for the position of the water front in the fracture:

$$X(t) = \frac{h_{inj}}{HL_f\rho_f c_f \Delta T}\left[K + Jt + L\exp\{Ft\} + M\exp\{Gt\}\right], \tag{5.1.20}$$

where

$$K = D - \frac{EB}{C}\frac{1}{C}, \tag{5.1.21}$$

$$J = \frac{E}{C}, \tag{5.1.22}$$

$$M = \frac{1 - \frac{E}{C} + F \;\; D - \frac{EB}{C} \;\; \frac{1}{C}}{G - F}, \tag{5.1.23}$$

$$L = -M - K, \tag{5.1.24}$$

with

$$B = \left| \frac{\ln(2)}{t_{cl,2}} + \frac{\ln(2)}{t_{cl,1}} \right| + \frac{(\gamma_1 + \gamma_2)}{L_f \, \rho_f c_f \Delta T}, \tag{5.1.25}$$

$$C = \frac{\ln(2)}{t_{cl,1}} \frac{\ln(2)}{t_{cl,2}} + \frac{\left| \gamma_1 \frac{\ln(2)}{t_{cl,2}} + \gamma_2 \frac{\ln(2)}{t_{cl,1}} \right|}{L_f \, \rho_f c_f \Delta T}, \tag{5.1.26}$$

$$D = \frac{\ln(2)}{t_{cl,1}} + \frac{\ln(2)}{t_{cl,2}}, \tag{5.1.27}$$

$$E = \frac{\ln(2)}{t_{cl,1}} \frac{\ln(2)}{t_{cl,2}}, \tag{5.1.28}$$

$$F = -\frac{B}{2} - \sqrt{\left(\frac{B}{2}\right)^2 - C}, \tag{5.1.29}$$

$$G = -\frac{B}{2} + \sqrt{\left(\frac{B}{2}\right)^2 - C}, \tag{5.1.30}$$

and

$$\gamma_1 = \frac{\ln(2)}{2} \frac{L_1 \rho_1 c_1 \Delta T}{t_{cl,1}}, \tag{5.1.31}$$

$$\gamma_2 = \frac{\ln(2)}{2} \frac{L_2 \rho_2 c_2 \Delta T}{t_{cl,2}}, \tag{5.1.32}$$

For the case of the permeable layer being a fracture and its aperture going to zero, Eq. 5.1.20 can be written as:

$$X(t)=\frac{h_{inj}}{H}\left|\frac{K}{L_f\,\rho_f c_f \Delta T}+\frac{J}{L_f\,\rho_f c_f \Delta T}t+\frac{L}{L_f\,\rho_f c_f \Delta T}\exp\{Ft\}+\frac{M}{L_f\,\rho_f c_f \Delta T}\exp\{Gt\}\right|, \tag{5.1.33}$$

where

$$\frac{K}{L_f\,\rho_f c_f \Delta T}=\frac{\gamma_1\left|\frac{\ln(2)}{t_{cl,2}}\right|^2+\gamma_2\left(\frac{\ln(2)}{t_{cl,1}}\right)^2}{\left(\gamma_1\frac{\ln(2)}{t_{cl,2}}+\gamma_2\frac{\ln(2)}{t_{cl,1}}\right)^2}, \tag{5.1.34}$$

$$\frac{J}{L_f\,\rho_f c_f \Delta T}=\frac{1}{\left|\gamma_1\frac{t_{cl,1}}{\ln(2)}+\gamma_2\frac{t_{cl,2}}{\ln(2)}\right|}, \tag{5.1.35}$$

$$\frac{L}{L_f\,\rho_f c_f \Delta T}=-\frac{1}{(\gamma_1+\gamma_2)}, \tag{5.1.36}$$

$$\frac{M}{L_f\,\rho_f c_f \Delta T}=\frac{1}{(\gamma_1+\gamma_2)}-\frac{\gamma_1\left|\frac{\ln(2)}{t_{cl,2}}\right|^2+\gamma_2\left(\frac{\ln(2)}{t_{cl,1}}\right)^2}{\left(\gamma_1\frac{\ln(2)}{t_{cl,2}}+\gamma_2\frac{\ln(2)}{t_{cl,1}}\right)^2}, \tag{5.1.37}$$

$$F=-\frac{(\gamma_1+\gamma_2)}{L_f\rho_f c_f \Delta T}, \tag{5.1.38}$$

and

$$G=0. \tag{5.1.39}$$

Alternatively, an expression for the position of the water front in a fracture can be found by substituting Eq. 5.1.19 into Eq. 5.1.8 and solving for X(t):

$$X(t)=\frac{h_{inj}}{H(\gamma_1+\gamma_2)}\left[\left|\frac{D-\frac{E}{I}}{I}\right|+\frac{E}{I}t+\left[1-\left(\left|\frac{D-\frac{E}{I}}{I}\right|\right)\right]\exp\{-It\}\right], \tag{5.1.40}$$

where

$$I = \frac{\gamma_1 \frac{\ln(2)}{t_{cl,2}} + \gamma_2 \frac{\ln(2)}{t_{cl,1}}}{(\gamma_1 + \gamma_2)} \quad . \tag{5.1.41}$$

If the matrices on the two sides of the fracture are identical, Eqs. 5.1.33 and 5.1.40 simplify to

$$X(t) = \frac{h_{inj} t_{cl}}{\ln(2) H L_m \rho_m c_m \Delta T} \left| 1 + \ln(2) \frac{t}{t_{cl}} \right|, \tag{5.1.42}$$

where the properties and dimensions are those associated with one matrix block on one side of the fracture. The thermal front advances linearly with time if the two matrix blocks are identical. It is noted that this model predicts a finite advance of the thermal front at the start of injection. This behavior at very early times is an artifact of using a late-time conduction model during the early-times of thermal front advance. Because of this, this late-time model is not valid during early times, i.e., times before t_{cl} (Eq. 2.1.10).

5.1.3 Discussion of One-Dimensional Models

This analysis has presented new models for quantifying the effect on the advance of a thermal front down a single fracture when the matrix properties on either side of the fracture differ. The early-time period model is similar to the previously published model of Marx and Langenheim (1959), except that it has been extended to allow different matrix properties on either side of the fracture.

The effect of different thermal properties on the location of the thermal front in the fracture can be seen in Figs. 27 and 28, for the early- and late-time models, respectively. For these models, the matrix block sizes are identical, but the thermal conductivity on one side of the fracture, i.e., of one matrix block, has been reduced by one-half. The relevant thermal properties for the base case of identical properties are given in Table 1. For the early-time period figure, Eqs. 5.1.16 and 5.1.17 were used for the cases of different and identical properties, respectively. For the late-time period figure, Eqs. 5.1.40 and 5.1.42 were used for the cases of different and identical properties, respectively. These figures show that a reduction of the thermal conductivity by a factor of two in one matrix block increases the advance rate of the front by 17% during the early-time period and by a constant amount during the late-time period.

Figures 29 and 30 compare the early- and late-time models for the case of identical and different properties, respectively. For Fig. 30, the thermal conductivity of one matrix block was reduced by a factor of two, consistent with Figs. 27 and 28. As indicated in Table 1, the time for the conduction front in the matrix blocks to reach the centerline, t_{cl}, is 42 days. For much earlier times, the early-time period model is valid. For later times, the late-time period model is valid. There is a significant period of overlap between the two models.

The effect of different matrix block sizes is shown in Figs. 31 and 32. Fig. 31 shows the effect of matrix block size on the late-time model and Fig. 32 compares the early- and late-time models. In these figures, the size of one of the matrix block is increased by a factor of two. The thermal conductivity for these figures is the same for all matrix blocks. From these figures it can be seen that changing the matrix block size changes the advance rate of the thermal front. It can also be seen that there is not necessarily an overlap between the early-and late-time period models.

5.2 Multi-Dimensional Geometry

For water advancing through a fracture network, the development of the governing equation is similar to that of water advancing through a single fracture. There are some important differences, however.

For a fracture network, the accumulation term is expressed as

$$q_{acc} = H\phi_f\rho_w c_w (T_w - T_i)\frac{dA}{dt} = H\phi_f\rho_w c_w \Delta T \frac{dA}{dt} \quad , \tag{5.2.1}$$

where H is the formation thickness, ϕ_f is the fracture porosity (as a fraction of the formation bulk volume), and the area is the areal extent of the heated zone as observed from the surface, i.e., the area in contact with the overburden.

This accumulation term expresses an important difference between the geometries of the one-dimensional, single fracture system and the multi-dimensional fracture network. For the single fracture, the fracture aperture or permeable layer thickness, L_f, was used. For the fracture network, the formation thickness, H, is used. For the single fracture, the area is the surface area of the matrix block in contact with the fracture, while for the fracture network the area is the planform or bulk area of the thermal zone as seen from the surface. These dimensions are orthogonal to each other. Conceptually, this can be visualized by considering the permeable layer or fracture of the one-dimensional model to be oriented vertically and heat conduction to

the matrix to be horizontal. In this conceptualization, the layer thickness and fracture aperture, L_f, is the horizontal width of that layer or fracture while the formation thickness, H, is the vertical height of the formation containing the vertical feature.

The energy stored in the matrix blocks is accounted for in the flux integrals given by Eq. 5.1.3. As mentioned above, the area in the flux integrals is the areal sweep of the thermal front, i.e., the contact area of the heated zone with the overburden. The area is not the actual surface area of the matrix blocks in contact with the fractures that was used in the one-dimensional models. In the multi-dimensional models, it is assumed that the formation is thick and that the thermal losses out of the fractured layer have a negligible impact on the advance of the thermal front relative to that of the heating of the matrix blocks within the reservoir.

The governing integro-differential equation for the area of the heated zone within a fracture network is obtained by substituting Eqs. 5.2.1 and 5.1.3 into Eq. 5.1.1, and converting from integrals over area to integrals over time:

$$h_{inj} = H\phi_f \rho_w c_w \Delta T \frac{dA}{dt} + \int_0^t q_{A,1}(t-\tau)\ \frac{dA}{d\tau} d\tau + \int_0^t q_{A,2}(t-\tau)\ \frac{dA}{d\tau} d\tau \quad . \tag{5.2.2}$$

For the case of the fracture porosity (as a function of bulk formation volume) being negligible, i.e., the fluid in the fractures have a negligible thermal capacity, Eq. 5.2.2 can be written as

$$h_{inj} = \int_0^t q_{A,1}(t-\tau)\ \frac{dA}{d\tau} d\tau + \int_0^t q_{A,2}(t-\tau)\ \frac{dA}{d\tau} d\tau \quad . \tag{5.2.3}$$

As with the cased of one-dimensional conduction, two conduction models will be used: one for the early-time period and one for the late-time period.

5.2.1 Early-Time Period

In this section, a model for determining the area of the thermal zone, i.e., the area affected by the injected water, will be determined for the early-time period in which the conduction fronts within individual matrix blocks are not expected to meet at the center of the matrix blocks.

The governing integro-differential equation for the area of the thermal zone is given by Eq. 5.2.2:

$$h_{inj} = H\phi_f \rho_w c_w \Delta T \frac{dA}{dt} + \int_0^t q_{A,1}(t-\tau)\ \frac{dA}{d\tau} d\tau + \int_0^t q_{A,2}(t-\tau)\ \frac{dA}{d\tau} d\tau \quad . \tag{5.2.4}$$

For the case of the fracture porosity (as a function of bulk formation volume) being negligible, i.e., the fluid in the fractures have a negligible thermal capacity, Eq. 5.2.4 can be written as

$$h_{inj} = \int_0^t q_{A,1}(t-\tau)\ \frac{dA}{d\tau} d\tau + \int_0^t q_{A,2}(t-\tau)\ \frac{dA}{d\tau} d\tau \quad . \tag{5.2.5}$$

The integrals in these equations account for the conductive energy transfer between the fracture network and the matrix blocks.

For the early-time period, the multi-dimensional conduction rate per unit area can be expressed through Eq. 2.2.13:

$$q_A = \frac{q}{dA} = \frac{Q_\infty}{t_{cl} dA} \left| J\sqrt{\frac{t_{cl}}{t}} - K + M\sqrt{\frac{t}{t_{cl}}} \right|, \tag{5.2.6}$$

where

$$J = \frac{1}{12} \left| 1 + \frac{L_x}{L_y} + \frac{L_x}{L_z} \right| \sqrt{\frac{D_L}{\pi}}, \tag{5.2.7}$$

$$K = \frac{1}{36} \left| \frac{L_x}{L_y} + \frac{L_x}{L_z} + \frac{L_x^2}{L_y L_z} \right| \frac{D_L}{\pi}, \tag{5.2.8}$$

and

$$M = \frac{1}{144} \frac{L_x^2}{L_y L_z} \sqrt{\frac{D_L}{\pi}^3} \quad . \tag{5.2.9}$$

In these equations, a dimensionless geometry factor has been defined as

$$D_L = \frac{\left(4L_x L_y + 4L_x L_z + 36 L_y L_z - 5L_x^2\right)}{\left(L_x L_y + L_x L_z + L_y L_z\right)}, \tag{5.2.10}$$

the time for the conduction fronts within the matrix blocks to reach the matrix block centers is given by

$$t_{cl} = \frac{L_x^2}{576\alpha} D_L, \tag{5.2.11}$$

and the cumulative amount of thermal energy conducted into a matrix domain after an infinite time is

$$Q_\infty = \chi_i \rho_m c_m (T_w - T_i) HdA = \chi_i \rho_m c_m \Delta T HdA, \tag{5.2.12}$$

where χ_i is the volume fraction of the i^{th} matrix domain, and HdA is the volume of a differential area of the geothermal reservoir. The volume fractions for the two matrix domains are related through the following expression:

$$\chi_1 + \chi_2 = 1. \tag{5.2.13}$$

Using these definitions, Eq. 5.2.6 can be rewritten as

$$q_A = \chi\omega \left| J\sqrt{\frac{t_{cl}}{t}} - K + M\sqrt{\frac{t}{t_{cl}}} \right|, \tag{5.2.14}$$

where

$$\omega = \frac{H\rho_m c_m \Delta T}{t_{cl}}. \tag{5.2.15}$$

Substituting Eq. 5.2.14 into Eq. 5.2.5, taking the Laplace transform of the equation, and solving for the area of the thermal zone in Laplace space yields

$$A(s) = \frac{h_{inj}}{E_1} \frac{1}{\sqrt{s}\left| s - \frac{E_2}{E_1}\sqrt{s} + \frac{E_3}{E_1} \right|}. \tag{5.2.16}$$

where

$$E_1 = \chi_1\omega_1 J_1\sqrt{\pi t_{cl,1}} + \chi_2\omega_2 J_2\sqrt{\pi t_{cl,2}} \quad , \tag{5.2.17}$$

$$E_2 = \chi_1\omega_1 K_1 + \chi_2\omega_2 K_2 \quad , \tag{5.2.18}$$

and

$$E_3 = \frac{\chi_1\omega_1 M_1}{\sqrt{t_{cl,1}}}\frac{\sqrt{\pi}}{2} + \frac{\chi_2\omega_2 M_2}{\sqrt{t_{cl,2}}}\frac{\sqrt{\pi}}{2} \quad . \tag{5.2.19}$$

Unfortunately a general inversion for Eq. 5.2.16 is not known. However, if the matrix block dimensions for a double porosity reservoir (single matrix domain) obey the following inequality:

$$\frac{L_z}{L_y} + \frac{L_y}{L_z} + \left(2 - \frac{3\pi}{2}\right)\left[1 + \frac{L_x}{L_y} + \frac{L_x}{L_z}\right] + \frac{L_x^2}{L_y L_z} > 0 \quad , \tag{5.2.20}$$

the bracketed term in the denominator of Eq. 5.2.16 can be factored and a partial fraction expansion applied. In this case, Eq. 5.2.16 can be inverted to the time domain to yield the following expression for the area of the thermal zone:

$$A(t) = \frac{h_{inj}}{E_1}\left[\frac{f_1}{\sqrt{\pi t}} + f_2\left(\frac{1}{\sqrt{\pi t}} - a\exp\left\{a^2 t\right\}\operatorname{erfc}\left\{a\sqrt{t}\right\}\right) + f_3\left(\frac{1}{\sqrt{\pi t}} - b\exp\left\{b^2 t\right\}\operatorname{erfc}\left\{b\sqrt{t}\right\}\right)\right] , \tag{5.2.21}$$

where

$$f_1 = \frac{1}{ab} \quad , \tag{5.2.22}$$

$$f_2 = -\frac{1}{a(b-a)} \quad , \tag{5.2.23}$$

$$f_3 = \frac{1}{a(b-a)} - \frac{1}{ab} \quad , \tag{5.2.24}$$

$$a = \frac{1}{2}\frac{E_2}{E_1} + \frac{\sqrt{\left|\frac{E_2}{E_1}\right|^2 - 4\frac{E_3}{E_1}}}{2} \quad , \tag{5.2.25}$$

and

$$b = \frac{1}{2}\frac{E_2}{E_1} - \frac{\sqrt{\left|\frac{E_2}{E_1}\right|^2 - 4\frac{E_3}{E_1}}}{2} \quad . \tag{5.2.26}$$

An inspection of Eqs. 5.2.22 through 5.2.24 reveals that

$$f_1 + f_2 + f_3 = 0 \quad . \tag{5.2.27}$$

Using this relationship, the expression for the area of the thermal zone, given by Eq. 5.2.21, can be simplified to

$$A(t) = \frac{h_{inj}}{E_1}\left[-f_2 a \exp\left\{a^2 t\right\}\operatorname{erfc}\left\{a\sqrt{t}\right\} - f_3 b \exp\left\{b^2 t\right\}\operatorname{erfc}\left\{b\sqrt{t}\right\}\right] \quad . \tag{5.2.28}$$

The restriction on the matrix block shape required by Eq. 5.2.20 limits the shapes of matrix blocks in which this solution applies. Acceptable values for the matrix block size can be obtained from the following equations:

$$L_y \geq L_x \tag{5.2.29}$$

and

$$L_z \geq \frac{1}{2}\left(\frac{3\pi}{2} - 2\right)\left(L_x + L_y\right) \pm \frac{1}{2}\sqrt{\left[\left(2 - \frac{3\pi}{2}\right)\left(L_x + L_y\right)\right]^2 - 4\left[\left(2 - \frac{3\pi}{2}\right)L_x L_y + L_y^2 + L_x^2\right]} \quad . \tag{5.2.30}$$

A conservative linear approximation to Eq. 5.2.30 is given by

$$L_z \geq \frac{1}{2}\left[\left(\frac{3\pi}{2} - 2\right) + \sqrt{3\pi\left(\frac{3\pi}{4} - 2\right)}\right]L_y + 4.84425 L_x \quad . \tag{5.2.31}$$

Equations 5.2.30 and 5.2.31 are plotted in Figs. 33 through 35 as a function of L_y for values of L_x of 10 m, 20 m, and 50 m, respectively. Acceptable values for matrix block geometry are those in the upper triangle. As long as L_z is greater than about $7L_y$, a solution probably exists. The matrix block shapes excluded in this solution are those that are nearly cubic.

The effect of matrix block size and shape on the swept thermal area is shown in Fig. 36. The three curves in this figure are for $L_y = L_x$, $L_y = 2L_x$, $L_y = 5L_x$, respectively, where $L_x = 10$ m. The value of L_z was determined from Eq. 5.2.31. The relevant properties are shown in Table 1. This figure shows that the thermal area grows faster for larger matrix blocks when the smallest dimension remains constant. This effect is from the reduced surface area for heat transfer associated with the matrix blocks having a larger aspect ratio. Larger matrix blocks slow energy transport between the fluid in the fractures and the matrix because of the reduced surface area per volume. This slower transport allows the fracture fluid to retain more of its original energy as it advances through the fracture network and results in a larger affected area.

The effect of two matrix domains having different matrix block sizes but identical thermal properties is shown in Fig. 37. In this figure the matrix blocks in each domain have $L_y = 2L_x$, with L_z being given by Eq. 5.2.31. One curve in the figure is for one matrix domain with $L_x = 10$ m and the second curve is for two matrix domains with one domain having $L_x = 10$ m and the other having $L_x = 20$ m. For the second curve, the volume fraction of the two matrix domains are one-half for each domain. Having some matrix blocks that are larger than others results in a more rapid advance of the thermal fronts through the reservoir because of the longer time required to heat the larger matrix blocks.

5.2.2 Late-Time Period

For the late-time period, i.e., for the case of water advance through a fracture network after conduction fronts reach the center of matrix blocks near the injection well, the conduction rate per unit surface area can be obtained from the multi-dimensional conduction model given by Eq. 3.2.58. This imbibition rate per unit area is given by

$$q_A = \frac{q}{dA} = \frac{V_m \rho_m c_m \Delta T \delta}{t_{cl} dA} \exp\left(-\delta \frac{t}{t_{cl}}\right) . \tag{5.2.32}$$

For this model, the multi-dimensional time for the conduction front to reach the center of the matrix is given by Eq. 2.2.11.

For the case of two matrix domains, the volume to be used in Eq. 5.2.32 is the volume fraction of the reservoir associated with each respective matrix domain:

$$V_m = \chi_i H dA , \tag{5.2.33}$$

where χ_i is the volume fraction of the i^{th} matrix domain. The volume fractions for the matrix domains within the fractured layer are related through the following expression:

$$\chi_1 + \chi_2 = 1. \tag{5.2.34}$$

The conduction rate per unit area can then be written as

$$q_A = \frac{q}{dA} = \frac{\chi_i H \rho_m c_m \Delta T \delta}{t_{cl}} \exp\left\{-\delta \frac{t}{t_{cl}}\right. \quad . \tag{5.2.35}$$

Substituting Eq. 5.2.35 into Eq. 5.2.2 and solving using Laplace transforms yields the following expression for the total area behind the thermal front in the fracture network:

$$A(t) = \frac{h_{inj}}{H \phi_f \rho_w c_w \Delta T}\left[K + Jt + L\exp\{Ft\} + M\exp\{Gt\}\right], \tag{5.2.36}$$

where

$$K = \left(D - \frac{EB}{C}\right)\frac{1}{C}, \tag{5.2.37}$$

$$J = \frac{E}{C}, \tag{5.2.38}$$

$$M = \frac{1 - \frac{E}{C} + F\left(D - \frac{EB}{C}\right)\frac{1}{C}}{G - F}, \tag{5.2.39}$$

$$L = -M - K, \tag{5.2.40}$$

with

$$B = \left|\frac{\delta_1}{t_{cl,1}} + \frac{\delta_2}{t_{cl,2}}\right| + \frac{(\chi_1\lambda_1 + \chi_2\lambda_2)}{H \phi_f \rho_w c_w \Delta T}, \tag{5.2.41}$$

$$C = \frac{\delta_1}{t_{cl,1}}\frac{\delta_2}{t_{cl,2}} + \frac{\left| \chi_1\lambda_1\frac{\delta_2}{t_{cl,2}} + \chi_2\lambda_2\frac{\delta_1}{t_{cl,1}} \right|}{H\phi_f\rho_w c_w \Delta T}, \qquad (5.2.42)$$

$$D = \frac{\delta_1}{t_{cl,1}} + \frac{\delta_2}{t_{cl,2}}, \qquad (5.2.43)$$

?? EMBED Equation.3 , (5 2.44)

?? EMBED Equation.3 ??, (5.2.45)

EMBED Equa ion.3 , (5.2.46)

t

and

EMBED Equation.3 , (5.2.47)

EMBED Equation.3 . (5.2.48)

For the case of the fracture porosity, ϕ_f, going to zero, Eq. 5.2.36 can be written as:

$$A(t) = h_{inj}\left| \frac{K}{H\phi_f\rho_w c_w \Delta T} + \frac{J}{H\phi_f\rho_w c_w \Delta T}t + \frac{L}{H\phi_f\rho_w c_w \Delta T}\exp\{Ft\} + \frac{M}{H\phi_f\rho_w c_w \Delta T}\exp\{Gt\} \right|, \qquad (5.2.49)$$

where

$$\frac{K}{H\phi_f\rho_w c_w \Delta T} = \frac{\left(\left| \chi_1\lambda_1 \left| \frac{\delta_2}{t_{cl,2}} \right|^2 + \chi_2\lambda_2\left(\frac{\delta_1}{t_{cl,1}}\right)^2 \right| \right)}{\left(\chi_1\lambda_1\frac{\delta_2}{t_{cl,2}} + \chi_2\lambda_2\frac{\delta_1}{t_{cl,1}} \right)^2}, \qquad (5.2.50)$$

$$\frac{J}{H\phi_f\rho_w c_w \Delta T} = \frac{1}{\left| \chi_1\lambda_1\frac{t_{cl,1}}{\delta_1} + \chi_2\lambda_2\frac{t_{cl,2}}{\delta_2} \right|}, \qquad (5.2.51)$$

$$\frac{L}{\phi_f\rho_w c_w \Delta T} = -\frac{1}{(\chi_1\lambda_1 + \chi_2\lambda_2)}, \qquad (5.2.52)$$

$$\frac{M}{H\phi_f\rho_w c_w \Delta T} = \frac{1}{(\chi_1\lambda_1 + \chi_2\lambda_2)} - \frac{\chi_1\lambda_1 \left| \frac{\delta_2}{t_{cl,2}} \right|^2 + \chi_2\lambda_2 \left(\frac{\delta}{t_{tr,1}} \right)^2}{\left(\chi_1\lambda_1 \frac{\delta_2}{t_{cl,2}} + \chi_2\lambda_2 \frac{\delta_1}{t_{cl,1}} \right)^2} . \tag{5.2.53}$$

Alternatively, an expression for the water swept area when the fracture porosity is negligible can be found by substituting Eq. 5.2.35 into Eq. 5.2.3:

$$A(t) = \frac{h_{inj}}{(\chi_1\lambda_1 + \chi_2\lambda_2)} \left[\left| \frac{D - \frac{E}{I}}{I} \right| + \frac{E}{I} t + \left[1 - \left| \frac{D - \frac{E}{I}}{I} \right| \right| \exp\{-It\} \right], \tag{5.2.54}$$

where

$$I = \frac{\left| \chi_1\lambda_1 \frac{\delta_2}{t_{cl,2}} + \chi_2\lambda_2 \frac{\delta_1}{t_{cl,1}} \right|}{(\chi_1\lambda_1 + \chi_2\lambda_2)} . \tag{5.2.55}$$

Eq. 5.2.54 is identical to Eq. 5.2.49.

If the two matrix domains in the fractured layer are identical, Eqs. 5.2.49 and 5.2.54 simplify to

$$A(t) = \frac{h_{inj} t_{cl}}{H\rho_m c_m \Delta T \delta} \left| 1 + \delta \frac{t}{t_{cl}} \right| . \tag{5.2.56}$$

This linear advance rate for the area of the thermal zone is analogous to that for a single fracture given by Eq. 5.1.42. A linear advance rate occurs when conduction has come to completion around the injection point and the zone of thermal transients is pushed away from the injection point.

5.2.3 Discussion of Late-Time Period Models

This analysis has presented new models for quantifying the effect of the advance of a thermal front through a fracture network when two matrix domains exist.

The effect of different thermal properties on the areal sweep of the thermal zone can be seen in Fig. 38. In this figure, the matrix blocks are all cubes. The relevant properties are given in Table 1. Equation 5.2.54 is used for the case of different properties and Eq. 5.2.56 is used for identical properties. The volume fractions for the two matrix domains are equal at 50% each. It can be seen that lowering the thermal conductivity of one matrix domain resulted in the thermal area to grow faster than otherwise. This is from the resulting delay in heating the matrix blocks behind the thermal front from slower conduction.

The effect of different matrix block sizes on the areal sweep can be seen in Fig. 39. In this figure, the thermal properties of the two matrix domains are equal, but the size of the matrix blocks in one domain is doubled. As with Fig. 38, the matrix blocks are cubes. It can be seen that having one matrix domain containing larger matrix blocks resulted in a faster expansion of the thermal zone. With one matrix domain having larger matrix blocks than the other, it will take longer for conduction to come to completion within the matrix blocks in that domain. Thus, more thermal energy will be available to expand the thermal zone as conduction proceeds.

A comparison to the early-time model, given by Eq. 5.2.28, with the late-time model, given by Eq. 5.2.54, is shown in Figs. 40 and 41 for the case of a single matrix domain. The matrix block domain dimensions for Fig. 40 are L_x = 10 m, $L_y = L_x$, and L_y given by Eq. 5.2.31. This gives a three-dimensional shape to the matrix block domain. For this case, the time for the conduction front within the matrix block to reach the its centerline is about 30 days and the early-time model is probably valid for about 150 days. The matrix block domain dimensions for Fig. 41 are L_x = 10 m and L_y = 1,000 m L_z = 10,000m. This gives a one-dimensional, slab shape to the matrix block domain. For this case, the time for the conduction front within the matrix block to reach the its centerline is about 50 days and the early-time model is probably valid for about 250 days. These figure show that the two models overlap for one-dimensional geometry, but do not for three-dimensional geometry. The problem lies in the late-time model that assumes a late-time conduction model through the early-time period.

The difference in the estimated time for the conduction front to reach the centerline of the matrix block, even though the smallest dimension is the same, is an artifact of the model. This artifact arose from using the linear-temperature-profile model to determine the centerline time. The primary effect of this artifact is in establishing a time to switch from the early-time to late-time period models for the area of the thermal zone. Because of the difficulty in using the late-time period model during the early-time period, this artifact is not considered significant.

6.0 Fracture Spacing Distributions

In naturally fractured geothermal reservoirs, fracture properties can govern fluid flow through the reservoir. Although exact information about the fracture locations, distributions, spacings, and apertures in the reservoir can never be completely known, relevant statistical fracture properties can often be obtained from outcrop and/or wellbore measurements. These statistical fracture properties can then be used in reservoir models to determine the probable reservoir behavior.

Fracture spacings are typically measured using a scanline along an outcrop or a core, where the successive spacings between fractures as they intersect the scanline are recorded. A variety of fracture spacing studies have been reported. In some studies, the spacing between successive fractures was recorded without regard to the fracture orientation (Priest and Hudson, 1976; Baecher et al., 1977; Einstein et al., 1979; Wallis and King, 1980; and Sen and Eissa, 1992). Although that method of measuring fracture spacing provides a qualitative measure of how fractured a formation may be, it does not provide a quantitative measure of the true spacing between fractures. The true spacing is the perpendicular spacing between parallel fractures.

In most fracture spacing studies, both the spacing between fractures and the fracture orientation (attitude) has been measured (Mahtab et al., 1973; Steffen, 1975; Bridges, 1975; Call et al., 1976; Barton, 1977; Baecher et al., 1977; Sen and Kazi, 1984; Rouleau and Gale, 1985; Huang and Angelier, 1989; Bardsley et al., 1990). The fractures are then subdivided into subparallel sets using the orientation data. The spacing between the scanline intersections of the fractures in each set is determined by ignoring all fractures not belonging to that set. The true spacing is then determined for each set using a trigonometric correction to correct for the scanline not being perpendicular to the set.

Once fracture spacing information has been obtained, the spacings for an individual set can be curve fit to a variety of mathematical models, including a negative exponential, log-normal, Weibull, gamma, power law (fractal), and normal distributions. Having such a mathematical model for the spacing distribution allows the data to be concisely summarized and simplifies subsequent simulation studies involving the spacing.

The simplest fracture spacing distribution is the negative exponential model (Mahtab et al., 1973; Call et al., 1976; Priest and Hudson, 1976; Baecher et al., 1977; Einstein et al., 1979; Wallis and King, 1980; Einstein and Baecher, 1983; and Sen and Eissa, 1992). This model has been shown to be related to the power law or fractal model (Poulton et al., 1990). Priest and Hudson (1976) reported that a negative exponential distribution is obtained if fractures are randomly distributed along the scanline, e.g., the presence of a fracture at one location is

independent of whether another fracture is present near that location. For such a distribution, the probability of having a fracture in a particular interval along the scanline has a Poisson distribution.

The most widely used fracture spacing distribution is the log-normal model (Steffen, 1975; Bridges, 1975; Barton, 1977; Baecher et al., 1977; Sen and Kazi, 1984; Rouleau and Gale, 1985; and Huang and Angelier, 1989). Bardsley et al. (1990) and Lorenz and Hill (1994) successfully matched oriented fracture spacing data a Weibull distribution. Huang and Angelier (1989) claimed that a gamma distribution fit their oriented fracture spacing better than a log-normal distribution and that a negative exponential distribution did not match the data at all. There is evidence that the fracture spacing distribution evolves as the joint sets become better developed (Rives et al., 1992).

Mathab, et al. (1995) conducted a systematic evaluation of fracture spacing distribution models by comparing them to various sets of published fracture spacing data. The models evaluated included negative exponential, log-normal, Weibull, normal, and gamma distributions. The fracture spacing data analyzed had been corrected for fracture orientation. They reported that the best overall fit was obtained using a log-normal distribution.

As discussed above, the two most common fracture spacing distributions observed in the field are the negative exponential and log-normal distributions. The probability density function for the negative exponential fracture spacing distribution is expressed as

$$f_{NE}(L) = \frac{1}{\langle L \rangle} \exp\left\{ -\frac{L}{\langle L \rangle} \right\}, \tag{6.1}$$

where L is the fracture spacing and <L> is the average fracture spacing. The cumulative probability density function is the integral of the probability density function and is expressed as

$$P_{NE}(L) = \int_0^L \frac{1}{\langle L \rangle} \exp\left(-\frac{L'}{\langle L \rangle} \right) dL' . \tag{6.2}$$

For the negative exponential distribution, the cumulative probability density function becomes

$$P_{NE}(L) = 1 - \exp\left(-\frac{L}{\langle L \rangle} \right) . \tag{6.3}$$

For a negative exponential distribution, the standard deviation of the fracture spacing about the average fracture spacing is equal to the average spacing.

The probability density function for the log-normal fracture spacing distribution is expressed as

$$f_{LN}(L) = \frac{1}{\sigma L\sqrt{2\pi}} \exp\ -\frac{(\ln(L)-\mu)^2}{2\sigma^2} \quad , \tag{6.4}$$

where μ is the average of the logarithms of the fracture spacings and σ is the standard deviation of the logarithms of the fracture spacings. The cumulative probability density function is the integral of the probability density function and is expressed as

$$P_{LN}(L) = \int_0^L \frac{1}{\sigma L'\sqrt{2\pi}} \exp\ -\frac{(\ln(L')-\mu)^2}{2\sigma^2}\ dL' \ , \tag{6.5}$$

or

$$P(L) = \frac{1}{\sqrt{2\pi}} \int_{-\infty}^{u} \exp\ -\frac{u^2}{2}\ du \ , \tag{6.6}$$

where

$$u = \frac{\ln(L)-\mu}{\sigma} \ . \tag{6.7}$$

The cumulative probability density function for a log-normal fracture spacing distribution is the normal probability integral in the variable $(\ln(L)-\mu)/\sigma$.

7.0 Incorporation of Fracture Data in Models

In this section, methods for incorporating statistical parameters from measured fracture spacing distributions into the models for the area of the thermal zone are developed. The objective of this analysis is to determine the appropriate values of L_x, L_y, and L_z to be used in the thermal advance models.

7.1 Early-Time Period: Single Matrix Domain

During the early-time period, the energy transfer between the fluid in the fracture network and the associated matrix blocks is proportional to the surface area of the matrix blocks available for heat transfer. The greater the surface area, the more rapid the energy transfer and the more slowly the areal extent of the thermal zone will grow. Large matrix block surface areas result from many small matrix blocks with close fracture spacings. Large matrix blocks have high surface areas per matrix block, but lower surface areas per volume, resulting in a lower overall surface area in the reservoir for heat transfer. This behavior was observed in Fig. 36.

The relationship between the thermal zone area and the surface area of individual matrix blocks is shown in Fig. 42. In this figure, the values of L_x, and L_y were varied from 1 m to 50 m in accordance with Eq. 5.2.29 while L_z was determined from Eq. 5.2.31. The area of the thermal zone is shown after one year for the properties given in Table 1. This figure shows that there is a very good correlation between the surface area of an individual matrix blocks comprising the formation and the areal extend of the thermal zone. Consistent with the previous discussion, large matrix blocks yield large thermal zone areas because of the lower overall heat transfer between the fluid and matrix blocks.

The next step to incorporate fracture spacing data into the model is to relate measured fracture spacing statistical data to the individual matrix block surface areas. Because of its relative simplicity, a negative exponential fracture spacing distribution was used. For each of the three orthogonal directions, fracture spacings were randomly generated that obeyed the negative fracture spacing distribution. These fracture spacing realizations were generated independently for each of the three directions and each had their own average fracture spacing. Typically over 10,000 individual realizations were obtained for each fracture set. For each set of three random fracture spacings, the spacings were sorted and labeled such that $L_x < L_y < L_z$.

The surface area of each individual matrix block was then calculated for those sets that satisfied Eq. 5.2.31. The average surface area per matrix block was then determined. These

Monte Carlo generated surface areas were then compared to the matrix block surface areas calculated from the average fracture spacings in the three directions and are shown in Fig. 43. Each data point in this figure corresponds to a complete Monte Carlo analysis for different sets of assumed average fracture spacings. The average spacings in two of the directions were varied from 1 m to 50 m, while that of the third direction was calculated by substituting the assumed fracture spacings from the first two directions into Eq. 5.2.31. It can be seen that the surface area calculated from the average fracture spacing is virtually equal to that calculated from the average of the areas obtained from the Monte Carlo analysis. Because the fracture spacings in the three directions are independent of each other, this result is to be expected.

The fracture spacing distribution data are incorporated into the one matrix domain, early-time period model by using the average fracture spacings in each direction in Eq. 5.2.28. These spacings are ordered such that $L_x < L_y < L_z$. Since there is only one matrix domain, $\chi_1 = 1$ and $\chi_2 = 0$.

7.2 Early-Time Period: Two Matrix Domains

The fracture spacing data for two matrix domains is incorporated into the early-time period model by finding an appropriate average matrix block surface area for each matrix domain and then selecting appropriate fracture spacings for each domain that yield the desired average matrix block surface area. One domain will tend to have the smaller matrix blocks and the other will have the larger matrix blocks.

The first step is to select the volume fractions associated with each domain. This is a choice made by the user. Then the midrange cumulative volume fractions for each matrix domain are determined. The midrange volume fraction is the characteristic cumulative volume fraction for each domain. If the matrix domains are assumed to each occupy 50% of the reservoir, the midrange cumulative volume fractions are 25% (midrange between 0 and 50%) and 75% (midrange between 50 and 100%). If the matrix domains are assumed to be 25% and 75% of the reservoir volume, the midrange cumulative volume fractions are 12.5% and 62.5%, respectively.

Next the surface area for matrix blocks in each domain is obtained from the midrange volume fraction. A relationship between the matrix block volume and surface area was obtained through a Monte Carlo analysis. For a particular set of average fracture spacings in three orthogonal directions, thousands of realizations of specific fracture spacings were generated and the surface area and volume of each corresponding matrix block was calculated. These data were

then sorted by increasing matrix block volume. The cumulative surface area was then calculated as a function of cumulative matrix block volume for the entire set of matrix blocks realizations. These curves were normalized by the total surface area and volume yielding the fractional cumulative surface area in the reservoir as a function of fractional cumulative volume of the reservoir, sorted by increasing matrix block volume. This process was repeated for a wide variety of average fracture spacings. Figure 44 shows this relationship for three arbitrary sets of average fracture spacings. It can be seen that there is little difference between these curves for different fracture spacings. This relationship can be approximated by the following equation:

$$A_{frac} = V_{frac}^{0.47} . \tag{7.2.1}$$

This curve is shown in Fig. 44 without plot symbols.

The characteristic fractional cumulative surface areas for each matrix domain are obtained by substituting the midrange cumulative volume fractions for the matrix domains into Eq. 7.2.1. The characteristic fractional cumulative matrix domain surface areas for each of the two domains are then normalized by dividing them by the characteristic fractional area of the reservoir if the reservoir were modeled as having only a single matrix domain, i.e., they are divided by the fractional cumulative area from Eq. 7.2.1 at a mid-range fractional cumulative volume fraction of 0.5. This fractional area is 0.72. This gives the normalized fractional cumulative surface area for each domain relative to that of a reservoir with a single matrix domain.

The final step is to relate the normalized fractional cumulative surface areas to the measured average fracture spacings. This is done by multiplying the values of average fracture spacings by the square root of the normalized fractional cumulative surface area for each domain and using those values in Eq. 5.2.28. This approach extends the method for a single matrix domain to two matrix domains. The square root is used because it yields the proper adjusted surface area for each domain when two lengths are multiplied to get an area.

7.3 Late-Time Period

Fracture spacing data can be incorporated into the late-time period model for the thermal area that was presented in Eq. 5.2.54. In this model, the area of the affected region was given as

$$A(t) = \frac{h_{inj}}{(\chi_1\lambda_1 + \chi_2\lambda_2)}\left[\left|\frac{D - \frac{E}{I}}{I}\right| + \frac{E}{I}t + \left[1 - \left(\left|\frac{D - \frac{E}{I}}{I}\right|\right)\right|\exp\{-It\}\right], \tag{7.3.1}$$

where

$$I = \frac{\left|\chi_1\lambda_1\frac{\delta_2}{t_{cl,2}} + \chi_2\lambda_2\frac{\delta_1}{t_{cl,1}}\right|}{(\chi_1\lambda_1 + \chi_2\lambda_2)}, \tag{7.3.2}$$

$$D = \frac{\delta_1}{t_{cl,1}} + \frac{\delta_2}{t_{cl,2}}, \tag{7.3.3}$$

$$E = \frac{\delta_1}{t_{cl,1}}\frac{\delta_2}{t_{cl,2}}, \tag{7.3.4}$$

$$\lambda_1 = \frac{H\rho_1 c_1 \Delta T}{t_{cl,1}}\delta_1, \tag{7.3.5}$$

$$\lambda_2 = \frac{H\rho_2 c_2 \Delta T}{t_{cl,2}}\delta_2, \tag{5.3.6}$$

and

$$\delta = \ln\left|\frac{12L_yL_z}{L_x^2 + 6L_yL_z - 2L_xL_y - 2L_xL_z}\right|. \tag{7.3.7}$$

An examination of the model reveals that all of the information about the matrix block size is provided in the ratio of δ/t_{cl}. This ratio can be written as

$$\frac{\delta}{t_{cl}} = \alpha \frac{576\left(L_x L_y + L_x L_z + L_y L_z\right)}{L_x^2\left(4L_x L_y + 4L_x L_z + 36L_y L_z - 5L_x^2\right)} \ln\left| \frac{12L_y L_z}{L_x^2 + 6L_y L_z - 2L_x L_y - 2L_x L_z} \right| . \qquad (7.3.8)$$

If a matrix block size parameter is defined such that

$$R = \frac{576\left(L_x L_y + L_x L_z + L_y L_z\right)}{L_x^2\left(4L_x L_y + 4L_x L_z + 36L_y L_z - 5L_x^2\right)} \ln\left| \frac{12L_y L_z}{L_x^2 + 6L_y L_z - 2L_x L_y - 2L_x L_z} \right| , \qquad (7.3.9)$$

then the ratio can be written as

$$\frac{\delta}{t_{cl}} = \alpha R . \qquad (7.3.10)$$

With this definition, the equation for the area of the thermal zone, Eq. 7.3.1, can be rewritten as

$$A(t) = \frac{h_{inj}}{H\rho c \Delta T \alpha} \left[\left| \frac{(R_1 + R_2) - (\chi_1 R_1 + \chi_2 R_2)}{R_1 R_2} \right| + \alpha t + \left[\frac{1}{(\chi_1 R_1 + \chi_2 R_2)} - \left(\frac{(R_1 + R_2) - (\chi_1 R_1 + \chi_2 R_2)}{R_2 R_1} \right| \exp\left\{ - \frac{R_1 R_2}{(\chi_1 R_1 + \chi_2 R_2)} \alpha t \right\} \right] \right| , \qquad (7.3.11)$$

where it has been assumed that the thermal properties of the matrix blocks in the two domains are equal, i.e., the fractures cut homogeneous rock.

For the case of a double porosity reservoir, i.e., one matrix domain, $R_1 = R_2$ and Eq. 7.3.11 simplifies to

$$A(t) = \frac{h_{inj}}{H\rho c \Delta T \alpha} \left(\frac{1}{R} + \alpha t \right) . \qquad (7.3.12)$$

A relationship between the matrix block size parameter, R, and the statistical parameters governing the fracture spacing distribution was obtained through Monte Carlo analysis. The matrix block size parameter was determined stochastically from Eq. 7.3.9 through independent realizations of the fracture spacings (matrix block sizes). Using the assumed negative-exponential fracture spacing distribution and three random numbers, three fracture spacings (orthogonal matrix block dimensions) were obtained that obeyed that distribution. The three orthogonal fracture spacings were then ordered such that $L_x < L_y < L_z$. These values were then

substituted into Eq. 7.3.9 to obtain one realization of the matrix block size parameter. The associated matrix block volume was also determined by multiplying the three fracture spacings. This process was then repeated with different random numbers having the same statistical parameters to obtain corresponding values for a large number of matrix blocks. Typically over 8,000 individual realizations were obtained for each fracture spacing distribution.

Once the multiple realizations of the matrix block size parameter and associated matrix block volume were obtained for a fracture spacing distribution, they were sorted in order of increasing matrix block size parameter and the cumulative volume fraction determined. These values were then curve-fit to a log-normal distribution of the cumulative matrix block volume as a function of increasing matrix block size parameter:

$$P(V_{frac}) = \frac{1}{\sqrt{2\pi}} \int_{-\infty}^{\frac{\ln(R)-\mu_R}{\sigma_R}} \exp\left(-\frac{u^2}{2}\right) du \ . \tag{7.3.13}$$

For a negative-exponential fracture spacing distribution, it was found that the statistical parameters for the cumulative matrix block volume probability density function as a function of the matrix block size parameter can be obtained using the following values:

$$\mu_R = 2 \ln\left| \frac{1}{\langle L_x \rangle} + \frac{1}{\langle L_y \rangle} + \frac{1}{\langle L_z \rangle} \right| + 1.41 \tag{7.3.14}$$

and

$$\sigma_R = 1.45 \ , \tag{7.3.15}$$

where $\langle L_x \rangle$, $\langle L_y \rangle$, and $\langle L_z \rangle$ are the respective average fracture spacings for the three orthogonal fracture sets defining the fracture network. One typical data set is compared to a log-normal distribution in Fig. 45. The validity of using Eq. 7.3.14 to relate the measured fracture spacing to the log-normal distribution statistical parameter, μ_R, is demonstrated in Fig. 46. In this latter figure, the values of μ_R computed from the Monte Carlo analysis are compared to those calculated with Eq. 7.3.14. These figures show that the matrix block size distribution can be reasonably modeled with this log-normal model.

A dimensionless matrix block size parameter can be defined as

$$X_R = \frac{\ln(R) - \mu_R}{\sigma_R} \quad . \tag{7.3.16}$$

The cumulative matrix block volume fraction given by Eq. 7.3.13 is plotted as a function of this dimensionless matrix block size parameter in Fig. 47. The matrix block size parameter, R, can be determined from the dimensionless matrix block size parameter given by Fig. 47 by inverting Eq. 7.3.16:

$$R = \exp\{X_R \sigma_R + \mu_R\} \quad . \tag{7.3.17}$$

where μ_R and σ_R are obtained from Eqs. 7.3.16 and 7.3.15, respectively.

The late-time period model is used by first selecting the matrix domain volume fractions and corresponding midrange volume fractions, determining the dimensionless matrix block size parameter from Fig. 47 using the midrange volume fractions, calculating the matrix block size parameter from Eq. 7.3.17 with the measured average fracture spacings, and then using those parameters in Eq. 7.3.12 for the case of a single matrix domain or Eq. 7.3.11 for two matrix domains.

7.4 Comparison on Models

The effect of using fracture spacing information in the models for the area of the thermal zone is demonstrated in this section. For this example, three orthogonal sets of fractures are assumed. The fracture spacing distribution for each set is assumed to follow the negative-exponential distribution, with average spacings of 10 m, 20 m, and 100 m, respectively. The other properties are given in Table 1.

7.4.1 Early-Time, One Matrix Domain (Double Porosity Reservoir)

For this case, the methodology presented in Section 5.2.1 is to be followed. The values of L_x, L_y, and L_z to be used in Eq. 5.2.28 are the average fracture spacings, 10 m, 20 m, and 100 m, respectively. The resulting area of the thermal zone is plotted in Fig. 48 as a function of time.

7.4.2 Early-Time, Two Matrix Domains (Triple Porosity Reservoir)

For this case, the methodology presented in Section 5.2.1, is to be followed. It will be assumed that the two matrix domains have equal volume fractions. The midrange volume fractions are 0.25 and 0.75, respectively for the two domains. The corresponding area fractions from Eq. 7.2.1 are 0.52 and 0.87, for the respective domains. The normalized area fractions are 0.72 and 1.21, respectively. The average fracture spacings for the two domains are then obtained by multiplying the measured average fracture spacing by the square root of the normalized area fraction. The values of L_x, L_y, and L_z to be used in Eq. 5.2.28 are then 8.5 m, 17.0 m, and 85 m for the first domain and 11 m, 22 m, and 110 m for the second domain. The resulting area of the thermal zone is plotted in Fig. 48 as a function of time.

7.4.3 Late-Time, One Matrix Domains (Double Porosity Reservoir)

For this case, the methodology presented in Section 5.2.2, is to be followed. If all matrix blocks are identical and have the same dimensions as the average fracture spacing, the value of the matrix size parameter can be determined from Eq. 7.3.9. However, uniform matrix blocks are not consistent with the assumption of a negative-exponential fracture spacing distribution. For the assumed fracture spacing distribution, the dimensionless matrix block size parameter is determined from Fig. 47 at the midrange volume fraction. Because there is only one matrix domain, the midrange volume fraction is 0.5, yielding dimensionless matrix block size parameter of 1. The statistical values for the mean and standard deviation of the logarithm of the fracture spacings given by Eqs. 7.3.14 and 7.3.15 are -2.26 and 1.45, respectively. The resulting matrix block size parameter is given by Eq. 7.3.17 as 0.44 m^{-2}. This matrix block size parameter is then used in Eq. 7.3.12. The resulting area of the thermal zone is plotted in Fig. 48 as a function of time.

7.4.4 Late-Time, Two Matrix Domains (Triple Porosity Reservoir)

For this case, the methodology presented in Section 5.2.2, is to be followed. It will be assumed that the two matrix domains have equal volume fractions. The midrange volume fractions are 0.25 and 0.75, respectively for the two domains. The corresponding logarithms of

the dimensionless matrix block size parameter from Fig. 47 are -0.67 and 0.67, for the respective domains, yielding dimensionless matrix block size parameters of 0.512 and 1.95, for the two domains, respectively. The statistical values for the mean and standard deviation of the logarithm of the fracture spacings given by Eqs. 7.3.14 and 7.3.15 are -2.26 and 1.45, respectively. The resulting matrix block size parameters are given by Eq. 7.3.17 as 0.22 m^{-2} and 1.76 m^{-2} for the two domains, respectively. These matrix block size parameters are then used in Eq. 7.3.11. The resulting area of the thermal zone is plotted in Fig. 48 as a function of time.

7.4.5 Discussion

The four models demonstrated in this section are shown in Fig. 48. This figure shows that the difference between the double-porosity and triple-porosity models, i.e., one or two matrix domains, is minor. Within the typical accuracy of most fracture spacing data, the additional complication of using models having multiple matrix domains is probably not justified. The reason that there is not a significant difference between the double and triple porosity systems is that the fracture spacings used for the two matrix domains are not radically different from each other. Because the fracture spacings used in the models are based on the assumption of a negative exponential fracture spacing distribution and because such a fracture spacing distribution has been shown to represent actual fracture spacings in many geothermal reservoirs, the use of more extreme fracture spacings to force a difference between the double and triple porosity models is expected to yield a physically unrealistic model.

The difference in the early- and late-time period models is from the bias of using a late-time period conduction model through the early-time period. The centerline time for these data are about 40 days.

8.0 Conclusions

In this project, new models were developed for estimating the size of the zone in a geothermal reservoir that has an altered temperature caused by the injection of a fluid into the fracture network at a temperature different from that of reservoir. The project was divided into two parts: thermal conduction into matrix blocks and thermal convection through the fracture network. One- and three-dimensional conduction models were developed for conduction into the matrix blocks. One- and three-dimensional convection models were developed for the advance of the thermally affected zone through the reservoir that utilize those conduction models for the thermal cross flow between the fractures and matrix blocks.

The key accomplishments of this project are summarized below.

1. A variety of one- and three-dimensional models for the transient conductive heating of parallelepiped matrix blocks were developed and compared to the classical models based on the solution to the constant thermal property heat diffusion equation.

2. Two conduction periods were identified: an early-time period in which conduction occurs as if into a semi-infinite medium and a late-time period in which conduction fronts from opposing faces merge at the center of the matrix block and interfere with each other. Interference from adjacent faces is allowed in both early- and late-time period three-dimensional models.

3. The best conduction model for the early-time period was found to be the classical model obtained from a similarity solution of the heat diffusion. This model is the square-root solution in one-dimensions and the extended square-root solution in three dimensions.

4. The best conduction model for the late-time period was found to be a semi-empirical exponential model. Although not exact, this model provides a reasonably accurate, relatively simple model that can be easily employed in simulators or spreadsheets. Unfortunately, this model is not accurate at very early times.

5. No simple model was found that was accurate over the entire conduction period.

6. A simple method was developed for estimating the centerline time, i.e., the time when the conduction fronts from opposing faces of the matrix block reach the center of the matrix block and begin to interfere with each other.

7. New models were developed for the advance of a thermal front in a single fracture (or set of parallel fractures) using the early- or late-time one-dimensional conduction models discussed above.

8. New models were developed for the advance of a thermal front in a fracture network using the early- or late-time three-dimensional conduction models discussed above. Models for both a double- and triple-porosity reservoir (one and two matrix domains) were also developed.

9. Methods for incorporating fracture spacing distribution data into all of the new thermal advance models were developed. The standard assumption of uniform fracture spacing is not required to use the new thermal advance models. A negative exponential fracture spacing distribution was assumed.

10. For an example reservoir, the use of a triple-porosity model (two matrix domains and one fracture domain) yielded results not significantly different from a double-porosity model (one matrix and one fracture domain). This result is expected to be valid for all reservoirs having a negative-exponential fracture spacing distribution. Given the usual uncertainties in fracture spacing and matrix properties, using the more sophisticated triple-porosity models is probably not warranted. This conclusion is based on the observation that many measured fracture spacing distributions follow the negative exponential behavior assumed in this study.

The results of this study have been condensed into two papers and presented at geothermal conferences: Reis (2000 and 2001).

Nomenclature

A	Area of matrix block face or heat transfer area
A_{frac}	Cumulative surface area fraction
A_o	Total surface area of one matrix block
A_x	Surface area of one matrix block face perpendicular to the x-direction
A_y	Surface area of one matrix block face perpendicular to the y-direction
A_z	Surface area of one matrix block face perpendicular to the z-direction
A'	Area of conduction front within matrix block
c_p	Specific heat
c_f	Heat capacity of fracture or permeable formation
c_m	Heat capacity of matrix
c_w	Heat capacity of water
C_f	Correction factor given by Eq. 3.2.23
D	Diffusion coefficient for imbibition
D_L	Dimensionless geometry factor in conduction models
h	Heat transfer coefficient
h_{inj}	Enthalpy injection rate
H	Height of formation or width of permeable layer
k	Permeability
k_{ro}	Relative permeability for oil
k_{rw}	Relative permeability for water
K	Thermal conductivity
K_m	Thermal conductivity of impermeable matrix
L	Matrix block or distance between evenly-spaced, parallel fractures
L_{eq}	Equivalent size of matrix block
L_f	Fracture aperture or formation thickness in direction of conduction
L_x	Matrix block dimension in x direction (three dimensional geometry)
L_y	Matrix block dimension in y direction (three dimensional geometry)
L_z	Matrix block dimension in z direction (three dimensional geometry)
L'	Distance of leading edge of thermal front from matrix block face
P_c	Capillary pressure
P_1	Parameter in VW-PW model
P_2	Parameter in VW-PW model
q	Thermal conduction rate

q_{acc} Energy accumulation rate in permeable layer or fracture

q_{loss} Energy loss rate to matrix from conduction

$q_{A,i}$ Conduction rate per unit area into i^{th} matrix domain

q_x Conduction rate in x-direction

q_y Conduction rate in y-direction

q_z Conduction rate in z-direction

Q Cumulative energy conducted

Q_{early} Cumulative energy conducted during early-time period

Q_{late} Cumulative energy conducted during late-time period

Q_∞ Cumulative energy conducted after an infinite time

R Matrix block size parameter

S_w Water saturation

r Radius from wellbore

r_w Radius of wellbore

t Time

t_{cl} Time when conduction front reaches the centerline of matrix block

t_D Dimensionless time

t_{tr} Transition time

t_{late} Time since beginning of late-time period

T Temperature

T_{cl} Temperature at centerline of matrix block

T_f Temperature of fracture or permeable formation

T_i Initial temperature

T_{inj} Injection temperature of water

T_m Temperature of matrix

T_s Surface temperature

T_w Temperature of water

$\overline{T}$ Average Temperature

ΔT T_w-T_i

$U(x)$ Unit step function

V Volume of matrix block

V_{corner} Volume of one corner of multi-dimensional matrix block

V_e Volume of differential element

V_{frac} Cumulative volume fraction

V_m Volume of matrix block

V_w Volume of water within fracture network

Vel_w Velocity of water in fracture

$\dot{V}_w$ Volumetric water injection rate

V' Volume of matrix block between conduction front and surface

x Coordinate direction, distance from matrix block surface

x_D Dimensionless distance

X Location of thermal front in fracture

X_R Dimensionless matrix block size parameter

y Coordinate direction, distance

y_D Dimensionless distance

z Coordinate direction

Greek Symbols

α Thermal diffusivity

α_m Thermal diffusivity of matrix

β Pre-exponential constant in late-time power-law model

β Geometric parameter in linear temperature-profile model

β Parameter in one-dimensional, early-time period thermal advance model

γ Exponent in late-time power-law model

γ Geometric parameter in linear temperature-profile model

γ Parameter in one-dimensional, late-time period thermal advance model

δ Geometric parameter given in exponential model

ϕ Matrix block porosity

ϕ_f Fracture porosity

λ Parameter in three-dimensional, late-time period thermal advance model

μ_o Oil viscosity

μ_w Water viscosity

ρ Density

ρ_f Density of fracture or permeable formation

ρ_m Density of matrix

ρ_w Density of water

ω Parameter in three-dimensional, early-time period thermal advance model

χ_i Matrix domain volume fraction

References

Baecher, G. B., Lanney, N. A., and Einstein, H. H., "Statistical Description of Rock Properties and Sampling," Proc. 18th US Symp. Rock Mechanics, pp. 501-508, 1977.

Bardsley, W. E., Major, T. J., and Selby, M. J., "Note on a Weibull Property for Joint Spacing Analysis," Int. J. Rock Mech. Min. Sci. and Geomech. Abstr., Vol. 27, pp. 133-134, 1990.

Barton, C. M., "A Geotechnical Analysis of Rock Structure and Fabric in the CSA Mine, Cobor, New South Wales, CSIRO Div. Appl. Geomech. Tech. paper 24, pp. 30-37, 1977.

Bech, N., Jensen, O. K., Nielsen, B., "Modeling of Gravity-Imbibition and Gravity-Drainage Processes: Analytic and Numerical Solutions," SPE Reservoir Engineering, pp. 129-136, Feb. 1991.

Beckner, B. K., Firoozabadi, A., and Aziz, K., "Modeling Transverse Imbibition in Double-Porosity Simulators," paper SPE 17414 presented at the California Regional Meeting, Long Beach, March 23-25, 1988.

Bodvarsson, G. S., "On the Temperature of Water Flowing Through Fractures," J. Geophys. Res., Vol. 74, No. 8, pp. 1987-1992, 1969.

Bodvarsson, G. S. and Tsang, C. F., "Injection and Thermal Breakthrough in Fractured Geothermal Reservoirs," J. Geophysical Res., Vol. 87, No. B2, pp. 1031-1048, Feb. 10, 1982.

Bodvarsson, G. S., Pruess, K., and O'Sullivan, M. J., "Injection and Energy Recovery in Fractured Geothermal Reservoirs," Soc. Pet. Eng. J., pp. 303-312, April 1985.

Bodvarsson, G. S., Pruess, K., and Lippmann, M. J., "Modeling of Geothermal Systems," J. Pet. Tech., Vol. 38, No. 10, pp. 1007-1021, Sept. 1986.

Bridges, M. C., "Presentation of Fracture Data for Rock Mechanics," Proc. 2nd Australian-New Zealand Conf. of Geomech., Brisbane, pp. 144-148, 1975.

Brook, C. A., Mariner, R. H., Swanson, J. R., Guffanti, M., and Muffler, L. J. P., "Hydrothermal Convection Systems with Reservoir Temperatures $\geq$90 ^{o}C, Assessment of Geothermal resources of the United States--1978, U.S. Geol. Surv. Cir., 790, 1978.

Call, R. D., Savely, J. P., and Nicholas, D. E., "Estimation of Joint Set Characteristics from Surface Mapping Data," Proc. 17th US Symp. on Rock Mechanics, Salt Lake City, Utah, Vol. 2b2, 1976.

Carslaw, H. S. and Jaeger, J. C., Conduction of Heat in Solids, Oxford U. Press, 1959.

Chen, J. Miller, M. A., and Sepehrnoori, K., "Investigations of Matrix-Fracture Transfer Flows in Dual Porosity Modeling of Naturally Fractured Reservoirs," paper SPE 29562 presented at the SPE Rocky Mountain Regional/Low-Permeability Reservoirs Symposium, Denver, CO, March 20-22, 1995a.

Chen, J. Miller, M. A., and Sepehrnoori, K., "Theoretical Investigation of Counter-Current Imbibition in a Fractured Reservoir Matrix Block," paper SPE 29141 presented at the SPE Symposium on Reservoir Simulation, San Antonio, TX Feb. 12-15, 1995b.

Cil, M., "Investigation of Individual and Combined Effects of Thermal Expansion and Capillary Imbibition in Naturally Fractured Reservoirs," M.S. Thesis, U. of Texas, Austin, 1992.

Closmann, P. J., "Steam Zone Growth During Multiple-Layer Steam Injection," Soc. Pet. Eng. J., pp. 1-10, March, 1967.

Dutra, J. and Aziz, K., "A New Double-Porosity Reservoir Model for Oil/Water Flow Problems," SPE Reservoir Engineering, pp. 419-425, Nov. 1992.

Einstein, H. H., Baecher, G. B., and Veneziano, D., "Risk Analysis for Rock Slopes in Open Pit Mines," Part I and Final Technical Report to US Bureau of Mines, Nov. 1979.

Einstein, H. H. and Baecher, G. B., "Probabilistic and Statistical Methods in Engineering Geology: Specific Methods and Examples, Part I: Exploration," Rock Mechanics and Rock Engineering, Vol. 16, pp. 39-72, 1983.

Gringarten, A. C., Witherspoon, P. A., and Ohnishi, Y., "Theory of Heat Extraction from Fractured Hot Dry Rock," J. Geophysical Res., Vol. 80, No. 8, pp. 1120-1124, March 10, 1975.

Handy, L. L., "Determination of Effective Capillary Pressures for Porous Media from Imbibition Data," Trans. AIME, Vol. 219, pp. 75-80, 1960.

Hearn, C. L., "Effect of Latent Heat Content of Injected Steam in a Steam Drive," J. Pet. Tech., pp. 374-375, April 1969.

Huang, Q and Angelier, J., "Fracture Spacing and its Relation to Bed Thickness," Geological Magazine, Vol. 126, No. 4, pp. 355-362, 1989.

Kuo, M. C. T., Kruger, P., and Brigham, W. E., "Shape-Factor Correlations for Transient Heat Conduction from Irregular-Shaped Rock Fragments to Surrounding Fluid," proceedings of the AIChE-ASME Heat Transfer Conference, Salt Lake City, April 15, 1977.

Lauwerier, H. A., "The Transport of Heat in an Oil Layer Caused by the Injection of Hot Fluid," Appl. Sci. Res. A, Vol. 5, pp. 145-150, 1955.

Lorenz, J. C. and Hill, R. E., “Subsurface Fracture Spacing: Comparison of Inferences From Slant/Horizontal and Vertical Cores,” SPE Formation Evaluation. 66-72. March, 1994.

Marx, J. W. and Langenheim, R. H., "Reservoir Heating by Hot Fluid Injection," Trans. AIME, Vol. 216, pp. 312-315, 1959.

Mahtab, M. A., Bolstad, D. D., and Kendorski, F. S., "Analysis of the Geometry of Fractures in San Manual Copper Mine, Arizona," U. S. Department of the Interior, Bureau of Mines, Report of Investigations 7715, 1973.

Mathab, M. A., Xu, S., Grasso, P., and Kendorski, F. S., "Use of Alternative Distributions for Characterizing Joint Extent and Spacing," in Fractured and Jointed Rock Masses, Myer, Cook, Goodman, and Tsang (eds), Balkema, Rotterdam, 1995.

Moody, J. D. G. and Horne, R. N., "Thermal Displacement in a Fractured Reservoir," paper SPE 17090, unsolicited manuscript, 1988.

Poulton, M. M., Mojtabai, N., and Farmer, I. W., "Scale Invariant Behavior of Massive and Fragmented Rock," Int. J. Rock Mech Min. Sci. and Geomech. Abstr., Vol. 27, No. 3, pp. 219-221, 1990.

Priest, S. D. and Hudson, J. A., "Discontinuity Spacing in Rock," Int. J. Rock Mech. & Min. Sci., Vol. 13, pp. 135-148, 1976.

Pruess, K. and Narisimhan, T. N., "A Practical Method for Modeling Fluid and Heat Flow in Fractured Porous Media," Soc. Pet. Eng. J., pp. 14-26, Feb. 1985.

Pruess, K. and Wu. Y-Sh., "A New Semi-Analytical Method for Numerical Simulation of Fluid and Heat Flow in Fractured Reservoirs, SPE Advanced Technology Series, Vol. 1, No. 2, pp. 63-72, 1993.

Pruess, K., Finsterle, S., Moridis, G., Oldenburg, C., Antunez, E., and Wu, Y., "Advances in the TOUGH2 Family of General-Purpose Reservoir Simulators," Proc. Geothermal Program Review XIV: Keeping Geothermal Energy Competitive in Foreign and Domestic Markets," Berkeley, CA, April 8-10, 1996.

Reis, J. C., "New Analytical Models for Multi-Dimensional Thermal Conduction in Fractured Geothermal Reservoirs," presented at the 25th Workshop on Geothermal Energy, Stanford University, CA, January 24-26, 2000.

Reis, J. C., "New Analytical Models for Growth of the Thermal Zone in Fractured Geothermal Reservoirs," presented at the 26th Workshop on Geothermal Energy, Stanford University, CA, January 29-31, 2001.

Reis, J. C. and Cil. M., "A Model for Oil Expulsion by Counter-Current Water Imbibition in Rocks: One-Dimensional Geometry," J. Pet. Sci and Eng., Vol. 10, pp. 97-107, 1993.

Reis, J. C. and Cil, M, "Analytical Models for Capillary Imbibition: One-Dimensional Matrix Blocks," In Situ, Vol. 23, No. 3, pp. 243-270, 1999.

Reis, J. C. and Cil, M, "Analytical Models for Capillary Imbibition: Multi-Dimensional Matrix Blocks," In Situ, Vol. 24, No. 1, pp. 79-106, 2000.

Rives, T., Razack, M., Petit, J.-P., and Rawnsley, K. D., "Joint Spacing: Analogue and Numerical Simulations," Journal of Structural Geology, Vol. 14, No. 8/9, pp. 925-937, 1992.

Rouleau, A. and Gale, J. E., "Statistical Characterization of the Fracture System in the Stripa Granite, Sweden," Int. J. Rock Mech. Min. Sci. and Geomech. Abstr., Vol. 22, No. 6, pp. 353-367, 1985.

Satman, A., "Solutions of Heat- and Fluid-Flow Problems in Naturally Fractured Reservoirs: Part 2 - Fluid Flow Problems," SPE Production Engineering, pp. 467-473, Nov. 1988.

Sen, Z. and Eissa, E. A., "Rock Quality Charts for Log-Normally Distributed Block Sizes," Int. J. Rock Mech. Min. Sci. and Geomech. Abstr., Vol. 29, pp. 1-12, 1992.

Sen, Z. and Kazi, A., "Discontinuity Spacing and RQD Estimates from Finite Length Scanlines," Int. J. Rock. Mech. Min. Sci. and Geomech. Abstr., Vol. 21, No. 4, pp. 203-312, 1984.

Somerton, W. H., Thermal Properties and Temperature-Related Behavior of Rock/Fluid Systems, Elsevier, Amsterdam, 1992.

Steffen, O., "Recent Developments in the Interpretation of Data from Joint Surveys in Rock Masses," Proc. 6th Reg. Cong. for Africa on Soil Mech. and Found., Vol. 9, No. 2, pp. 7-26, 1975.

Stehfest, H., "Algorithm 368: Numerical Inversion of Laplace Transforms," Communications of the ACM, Vol. 13, No. 1., pp. 47-49, 1970.

Vinsome, P. K. W. and Westerveld, J., "A Simple Method for Predicting Cap and Base Rock Heat Losses in Thermal Reservoir Simulators," J. Can. Pet. Tech., pp. 87-90, 1980.

Wallis, P. F. and King, M. S., "Discontinuity Spacings in a Crystalline Rock," Int. J. Rock Mech., Min. Sci. Geomech. Abstr., Vol. 17, pp. 63-66, 1980.

Zhang, X., Morrow, N. R., Ma, S., "Experimental Verification of a Modified Scaling Group for Spontaneous Imbibition," SPE Reservoir Engineering, pp. 280-285, Nov. 1996.

Zimmerman, R. W., Bodvarsson, G. S., and Kwicklis, E. M., "Absorption of Water into Porous Blocks of Various Shapes and Sizes," Water Resources Research, Vol. 26, No. 11, pp. 2729-2806, 1990.

Table 1. Properties of Example Reservoir

Property	**Value**
L_m	10 m
h_{inj}	1.0×10^6 J/s
H	100 m
k_m	2.8 W/m/K
ρ_m	2630 kg/m^3
c_m	800 J/kg/K
t_{cl} (one-D)	3.69×10^6 s
t_{cl} (multi-D)	1.70×10^6 s
ΔT	200 K
β	2.74×10^5 J/s$^{1/2}$/m^2
γ	395 J/s/m^2
λ	3.44×10^4 J/s/m^2

Appendix: Summary of Thermal Growth Models

Two models were developed in this study for the areal extent of the thermal zone following reinjection in a geothermal reservoir: one for early-time behavior and one for late-time behavior. These models are summarized in this appendix. Because it has been shown that the difference between dual- and triple-porosity models is small, only the dual porosity models will be described here. The data required by these models is also summarized.

Early-Time Model

The thermal area is given by

$$A(t) = \frac{h_{inj}}{E_1}\left[-f_2 a \exp\{a^2 t\}\operatorname{erfc}\{a\sqrt{t}\} - f_3 b \exp\{b^2 t\}\operatorname{erfc}\{b\sqrt{t}\}\right] . \quad (5.2.28)$$

where

$$f_2 = -\frac{1}{a(b-a)} , \quad (5.2.23)$$

$$f_3 = \frac{1}{a(b-a)} - \frac{1}{ab} , \quad (5.2.24)$$

$$a = \frac{1}{2}\frac{E_2}{E_1} + \frac{\sqrt{\left|\frac{E_2}{E_1}\right|^2 - 4\frac{E_3}{E_1}}}{2} , \quad (5.2.25)$$

$$b = \frac{1}{2}\frac{E_2}{E_1} - \frac{\sqrt{\left|\frac{E_2}{E_1}\right|^2 - 4\frac{E_3}{E_1}}}{2} . \quad (5.2.26)$$

$$E_1 = \omega J\sqrt{\pi t_{cl}} , \quad (5.2.17)$$

$$E_2 = \omega K , \quad (5.2.18)$$

$$E_3 = \frac{\omega M}{\sqrt{t_{cl}}} \frac{\sqrt{\pi}}{2} \quad . \tag{5.2.19}$$

$$\omega = \frac{H \rho_m c_m \Delta T}{t_{cl}}, \tag{5.2.15}$$

$$J = \frac{1}{12} \left| 1 + \frac{L_x}{L_y} + \frac{L_x}{L_z} \right| \sqrt{\frac{D_L}{\pi}}, \tag{5.2.7}$$

$$K = \frac{1}{36} \left| \frac{L_x}{L_y} + \frac{L_x}{L_z} + \frac{L_x^2}{L_y L_z} \right| \frac{D_L}{\pi}, \tag{5.2.8}$$

$$M = \frac{1}{144} \frac{L_x^2}{L_y L_z} \sqrt{\frac{D_L}{\pi}^3}, \tag{5.2.9}$$

$$D_L = \frac{\left(4L_x L_y + 4L_x L_z + 36 L_y L_z - 5L_x^2\right)}{\left(L_x L_y + L_x L_z + L_y L_z\right)}, \tag{5.2.10}$$

and

$$t_{cl} = \frac{L_x^2}{576\alpha} D_L . \tag{5.2.11}$$

The data required for this model are

h_{inj}	Enthaply of injected water (relative to water at formation temperature)
H	Formation thickness
L_x	Smallest average fracture spacing in any direction
L_y, L_z	Average fracture spacings in the other two orthogonal directions
ΔT	Temperature Difference between formation and injected water
α	Formation thermal diffusivity
$\rho_m c_m$	Formation volumetric heat capacity

The fracture spacings are constrained such that

$$L_z \geq \frac{1}{2}\left(\frac{3\pi}{2}-2\right)(L_x+L_y)\pm\frac{1}{2}\sqrt{\left[\left(2-\frac{3\pi}{2}\right)(L_x+L_y)\right]^2-4\left[\left(2-\frac{3\pi}{2}\right)L_xL_y+L_y^2+L_x^2\right]}\,, \qquad (5.2.30)$$

or, more conservatively, by

$$L_z \geq \frac{1}{2}\left[\left(\frac{3\pi}{2}-2\right)+\sqrt{3\pi\left(\frac{3\pi}{4}-2\right)}\right]L_y + 4.84425L_x\,. \qquad (5.2.31)$$

or

$$L_z \geq 2.272L_y + 4.84425L_x\,.$$

Late-Time Model

The thermal area is given by

$$A(t)=\frac{h_{inj}}{H\rho_m c_m \Delta T\alpha}\left(\frac{1}{R}+\alpha t\right)\,, \qquad (7.3.12)$$

$$R=\exp\{X_R\sigma_R+\mu_R\}\,, \qquad (7.3.17)$$

$$\mu_R=2\ln\left|\frac{1}{\langle L_x\rangle}+\frac{1}{\langle L_y\rangle}+\frac{1}{\langle L_z\rangle}\right|+1.41\,, \qquad (7.3.14)$$

$$\sigma_R=1.45\,, \qquad (7.3.15)$$

and

$$X_R=1\,.$$

The data requirements for the late-time model are identical to that of the early-time model, except that there are no constraints on the matrix block dimensions:

h_{inj}	Enthaply of injected water (relative to water at formation temperature)
H	Formation thickness
L_x	Smallest average fracture spacing in any direction

L_y, L_z Average fracture spacings in the other two orthogonal directions

ΔT Temperature Difference between formation and injected water

α Formation thermal diffusivity

$\rho_m c_m$ Formation volumetric heat capacity

Transition from Early-Time to Late-Time Behavior

Transition from early-time behavior, when conduction fronts into individual matrix blocks have not reached the center of the matrix blocks, to late-time behavior when the conduction fronts from opposing faces of the matrix block have merged with the matrix block occurs when the conduction fronts are modeled to reach the center of the matrix block:

$$t_{cl} = \frac{L_x^2}{576\alpha} D_L . \qquad (5.2.11)$$

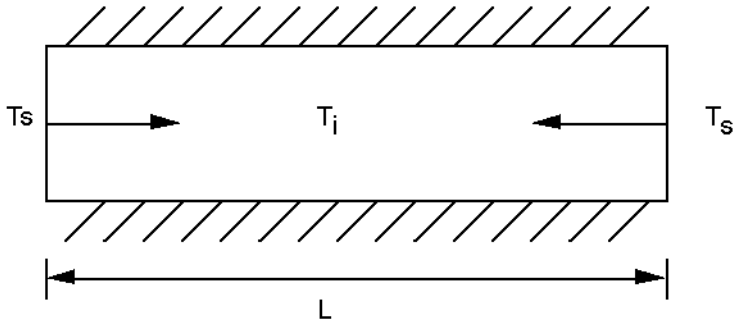

Figure 1. Geometry for One-Dimensional Conduction Model

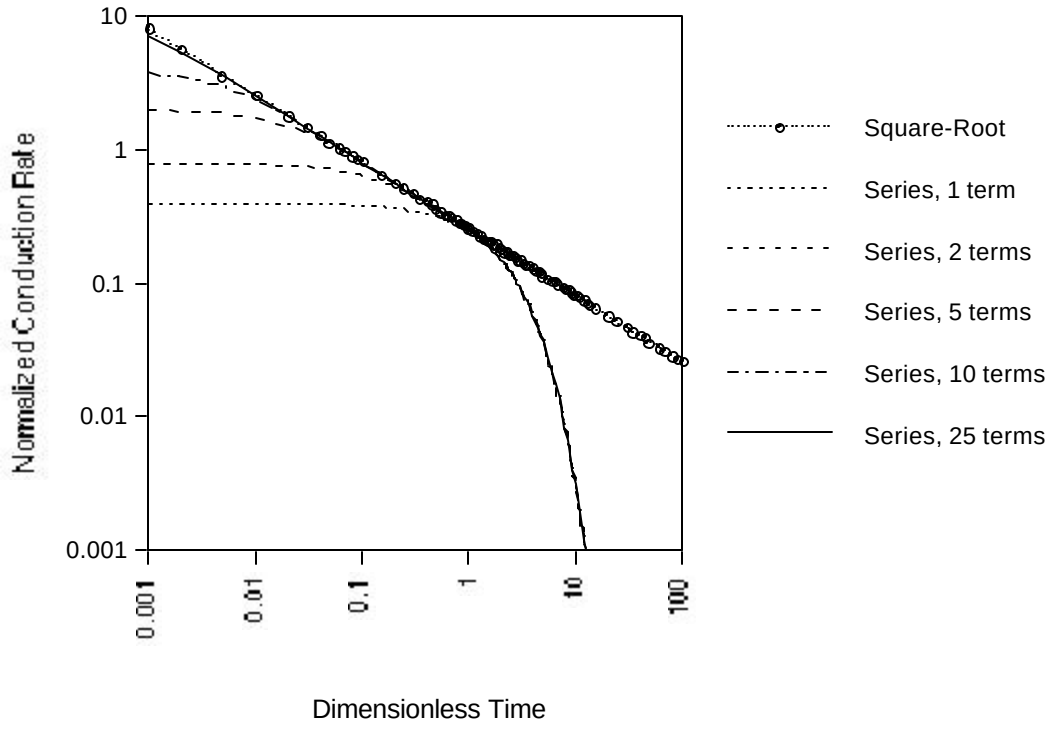

Figure 2. One-Dimensional Conduction Rate: Exact Models

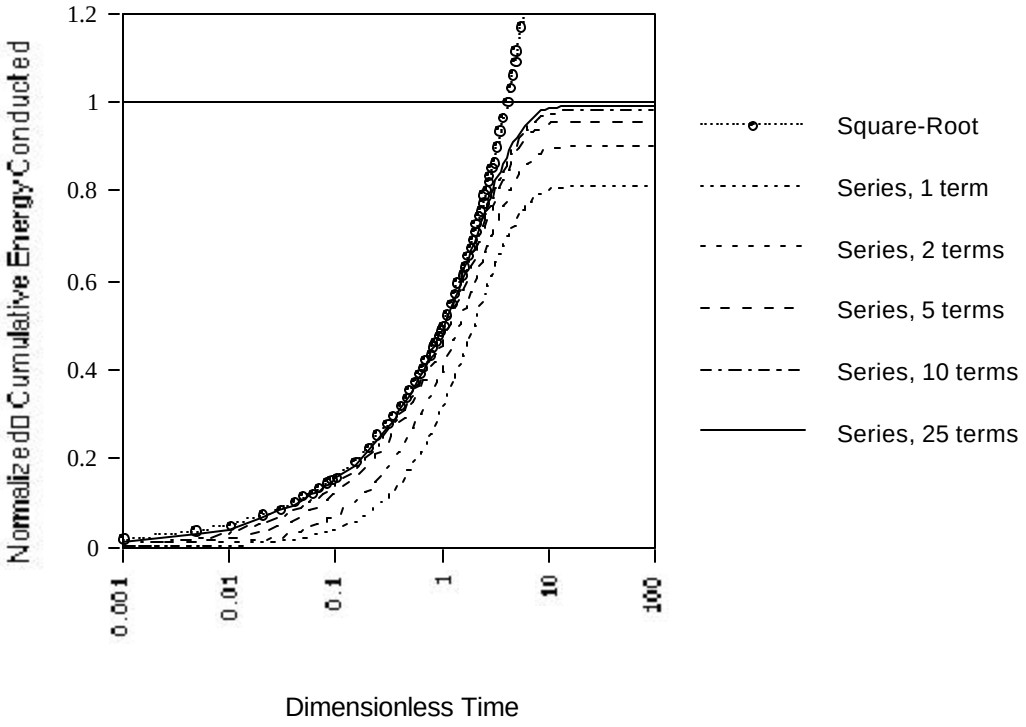

Figure 3. One-Dimensional Cumulative Energy Conducted: Exact Models

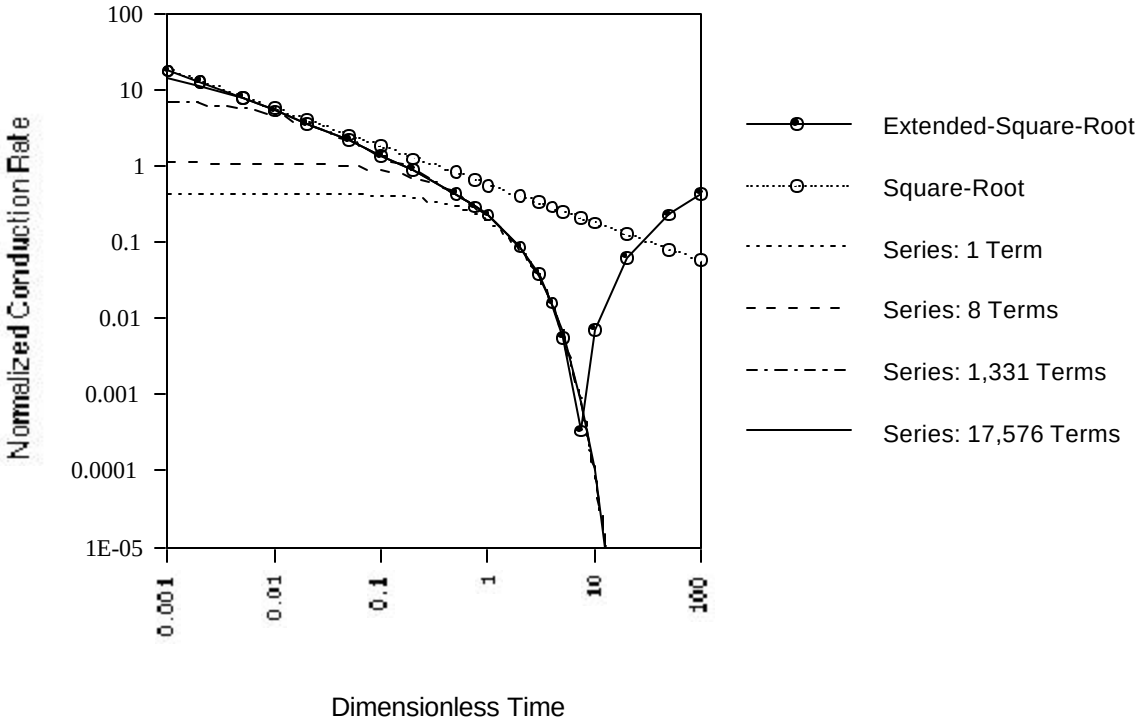

Figure 4. Multi-Dimensional Conduction Rate: Exact Models

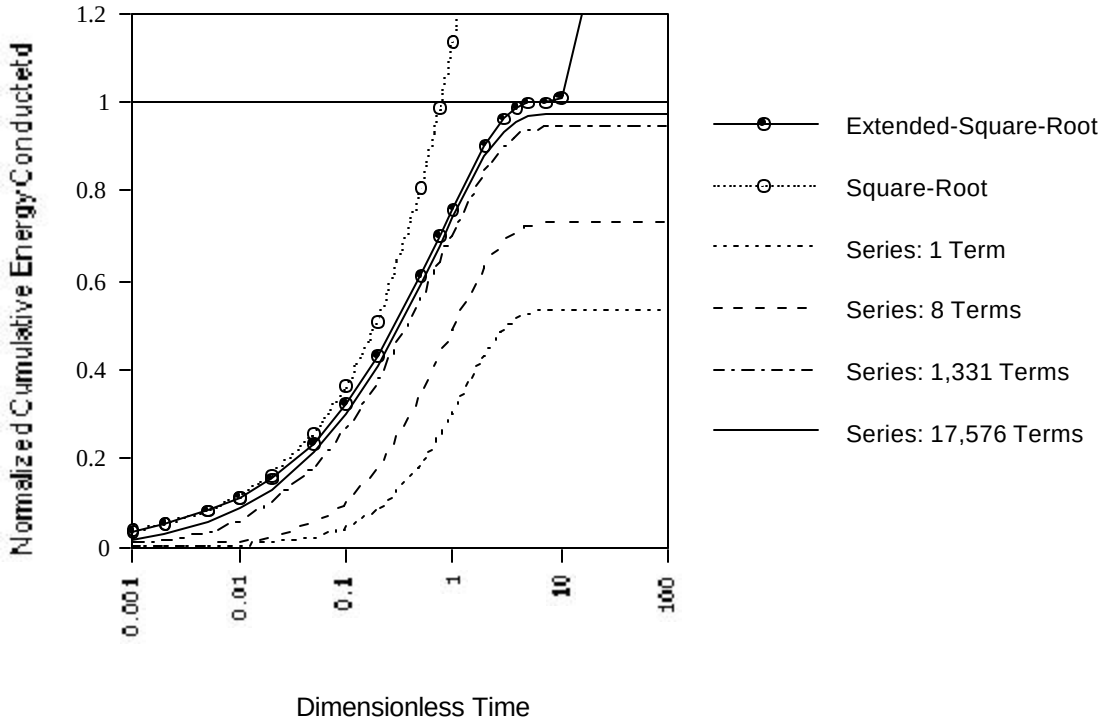

Figure 5. Multi-Dimensional Cumulative Energy Conducted: Exact Models

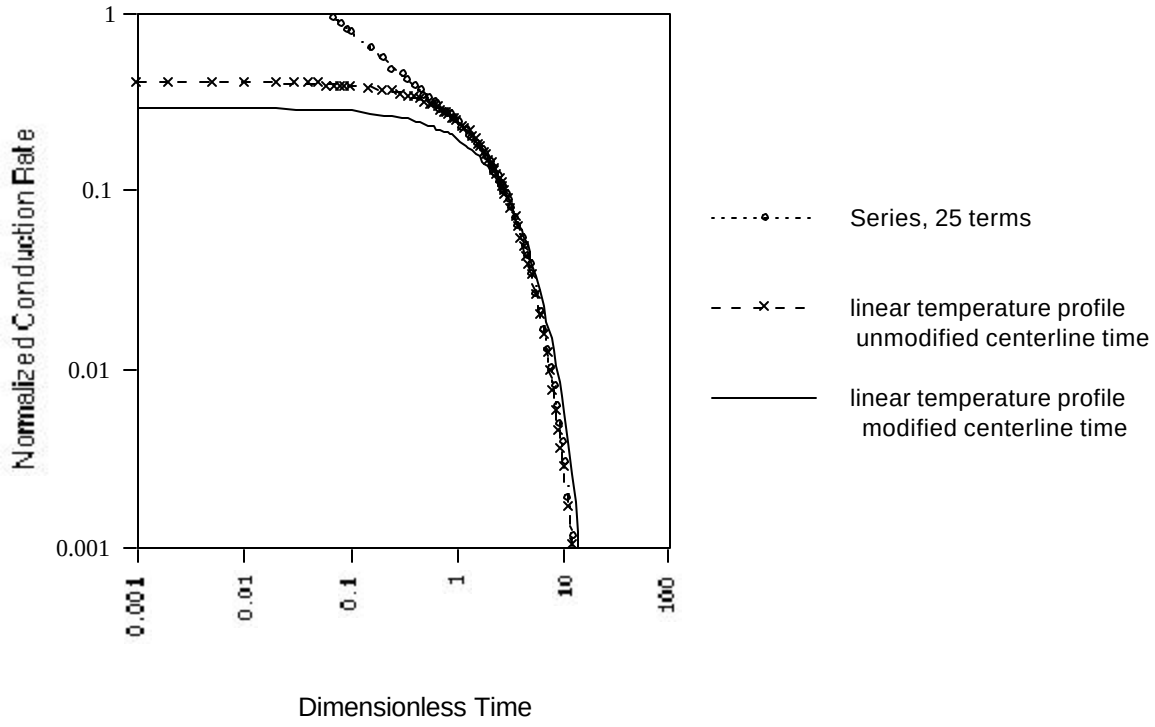

Figure 6. Comparison of Linear-Temperature-Profile Rate Models

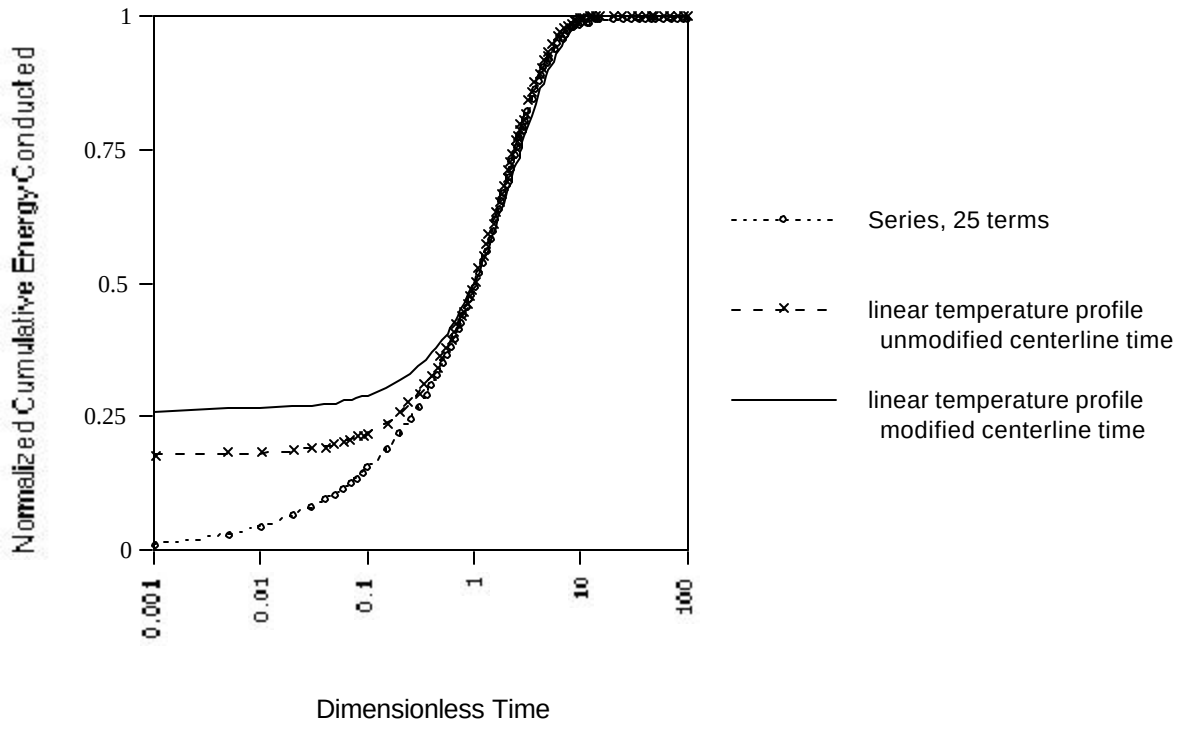

Figure 7. Comparison of Linear-Temperature-Profile Cumulative Models

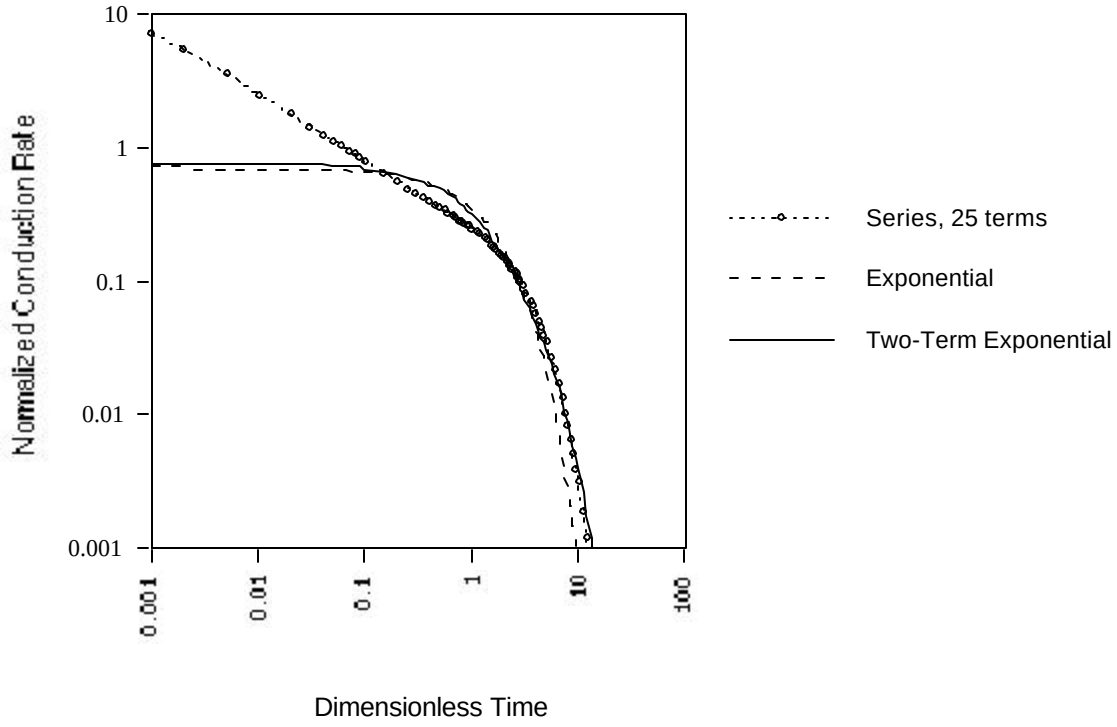

Figure 8. Comparison of Exponential Rate Models

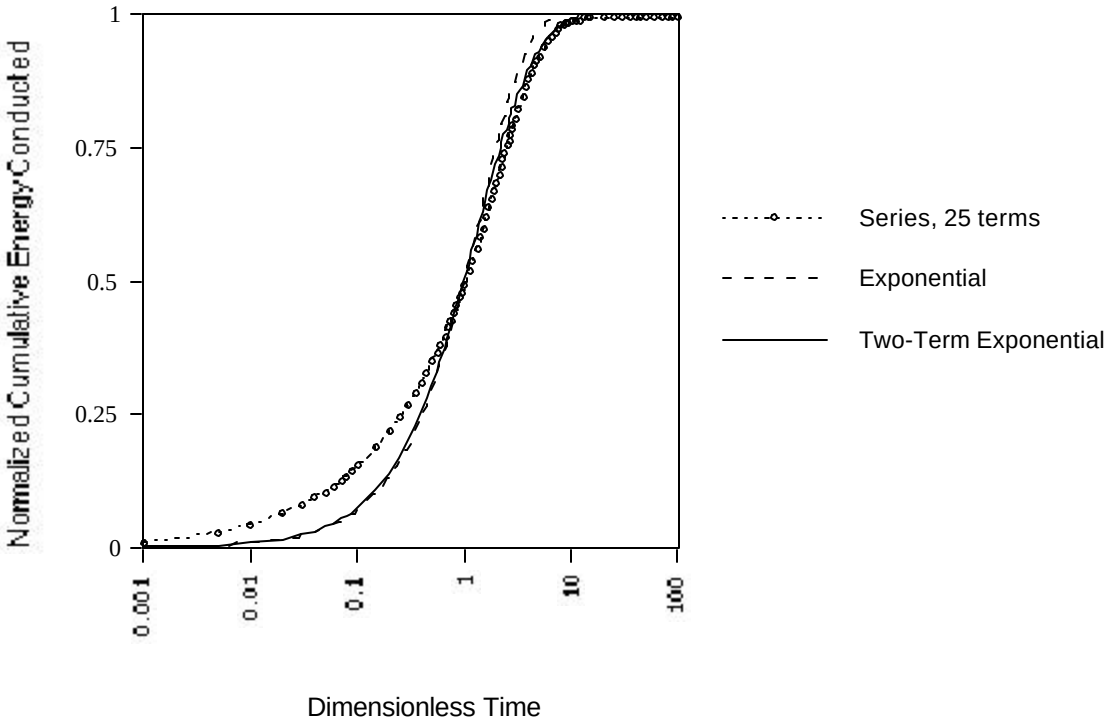

Figure 9. Comparison of Exponential Cumulative Models

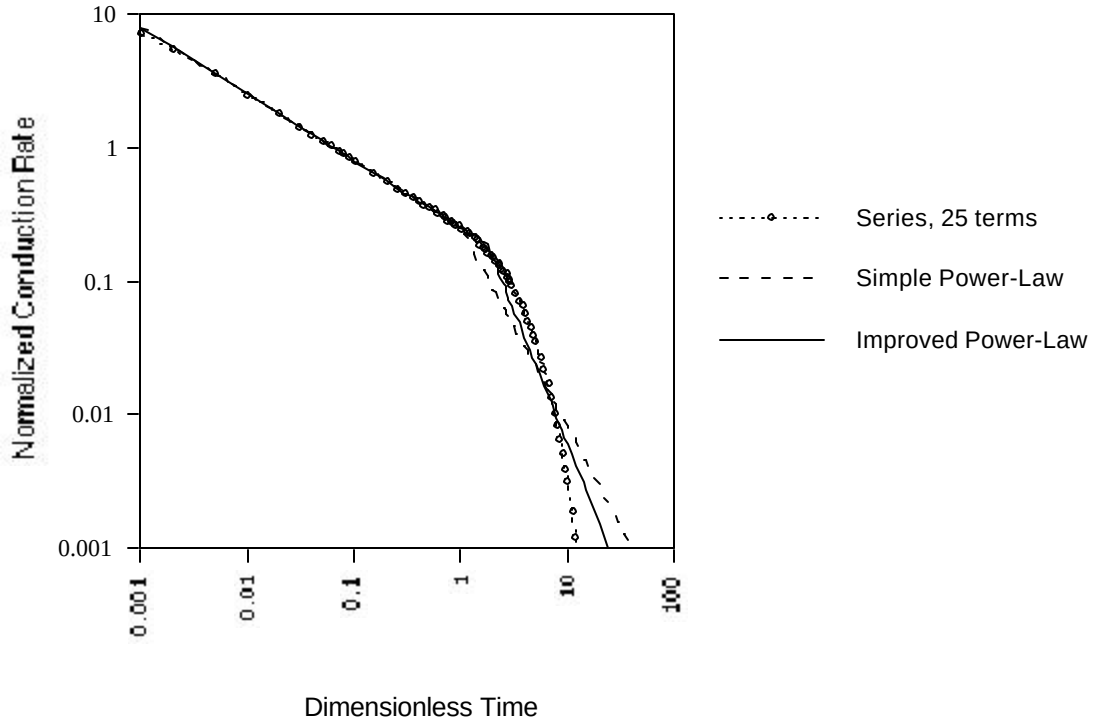

Figure 10. Comparison of Power-Law Rate Models

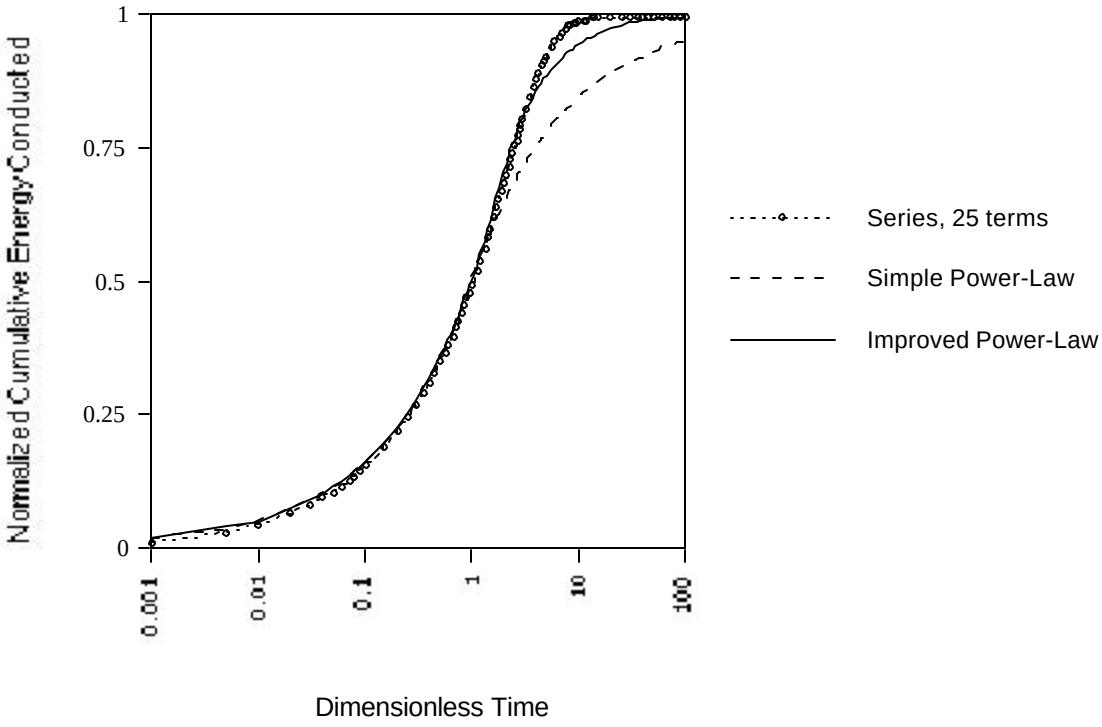

Figure 11. Comparison of Power-Law Cumulative Models

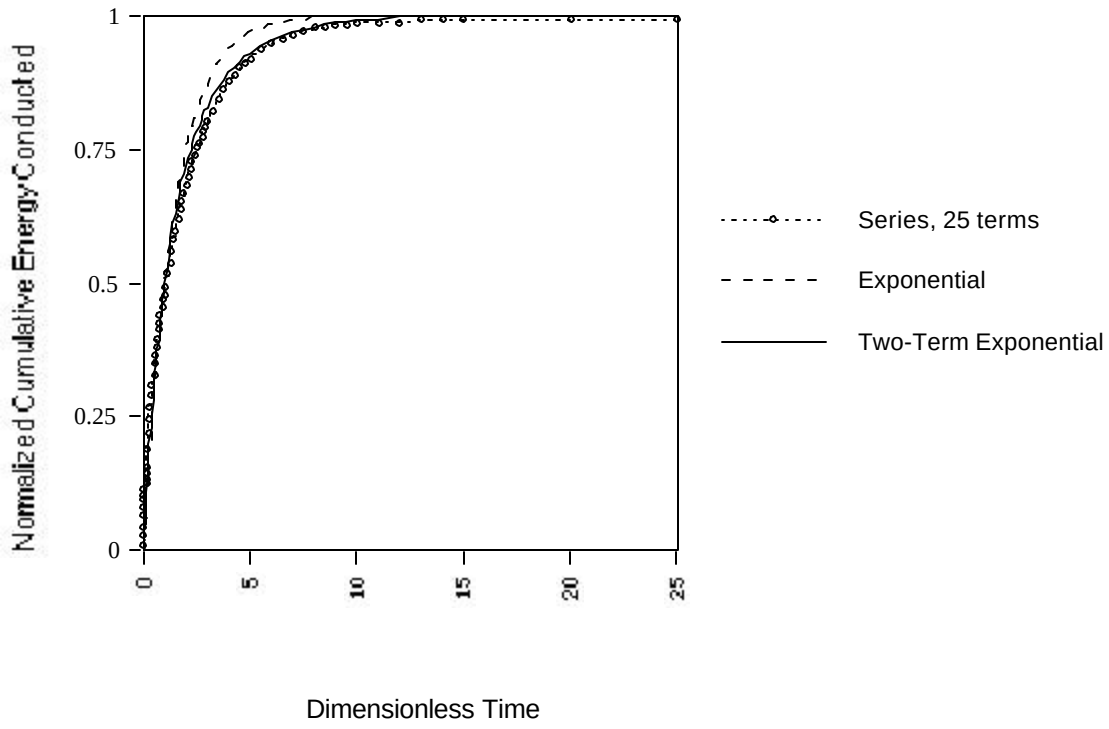

Figure 12. Comparison of Exponential Cumulative Models Linear Scale

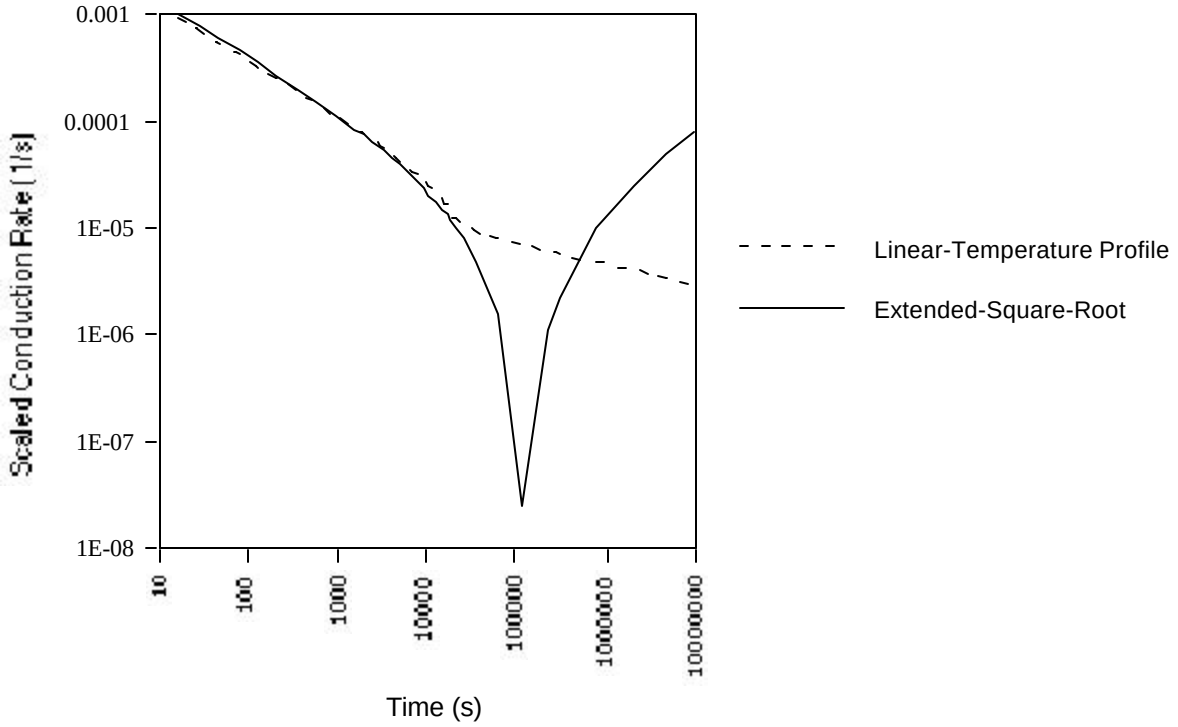

Figure 13. Comparison of Early-Time, Dimensional, Linear-Temperature-Profile Rate Model: Cubic Geometry

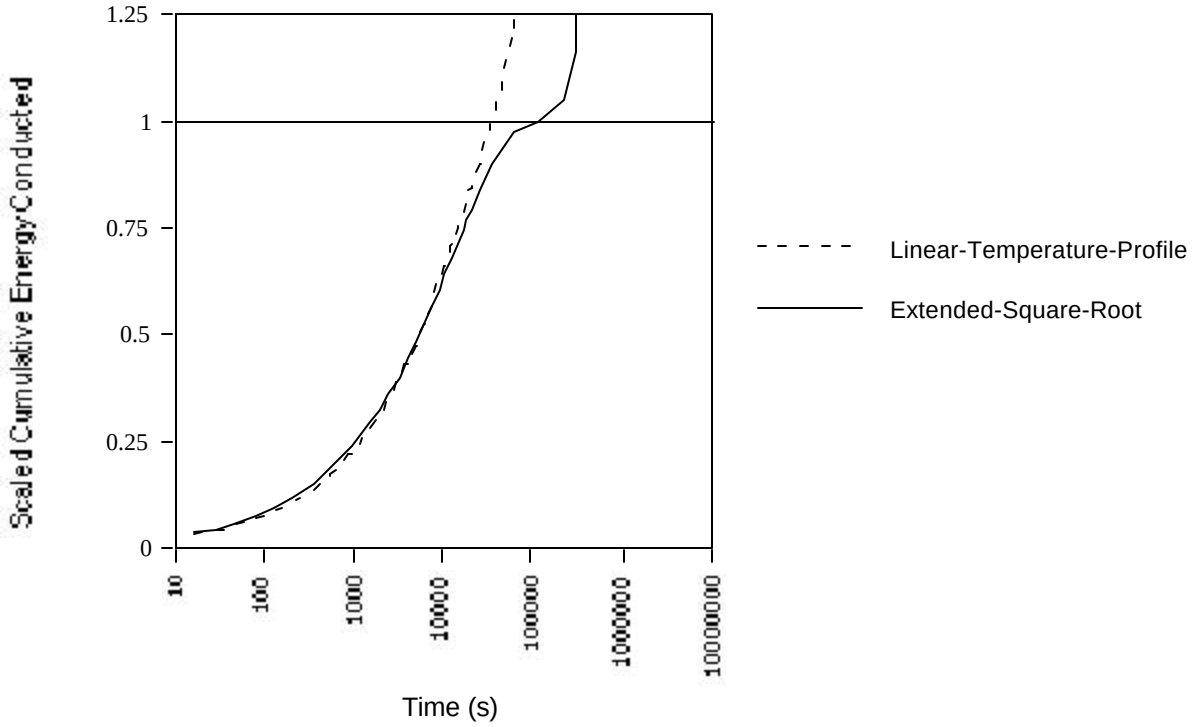

Figure 14. Comparison of Early-Time, Dimensional, Linear-Temperature-Profile Cumulative Model: Cubic Geometry

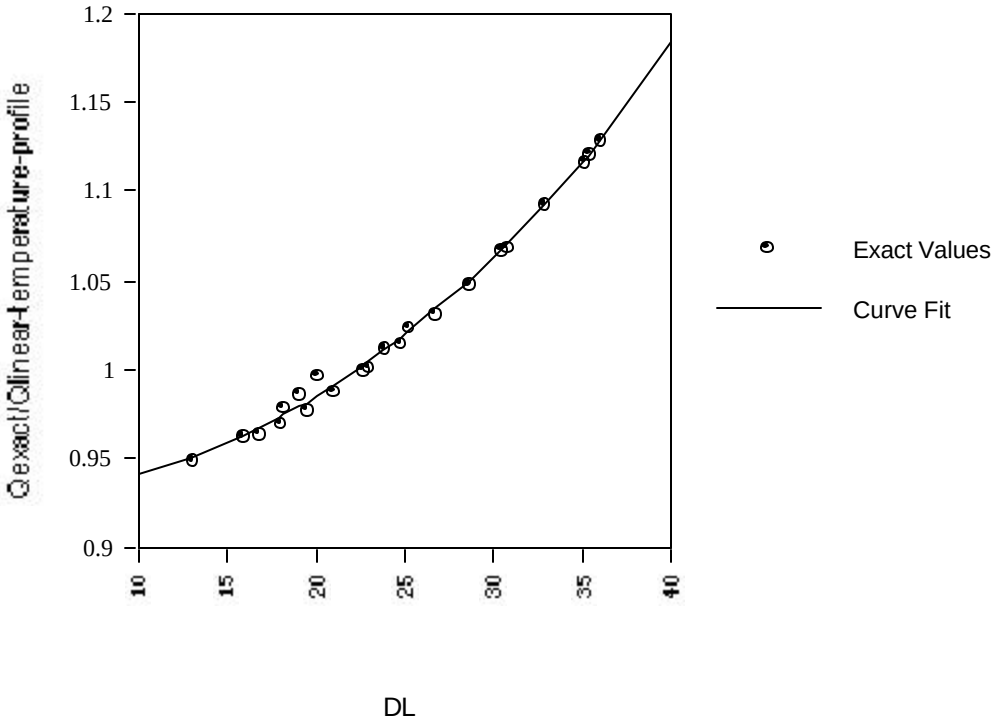

Figure 15. Correction Factor for Linear-Temperature-Profile Model

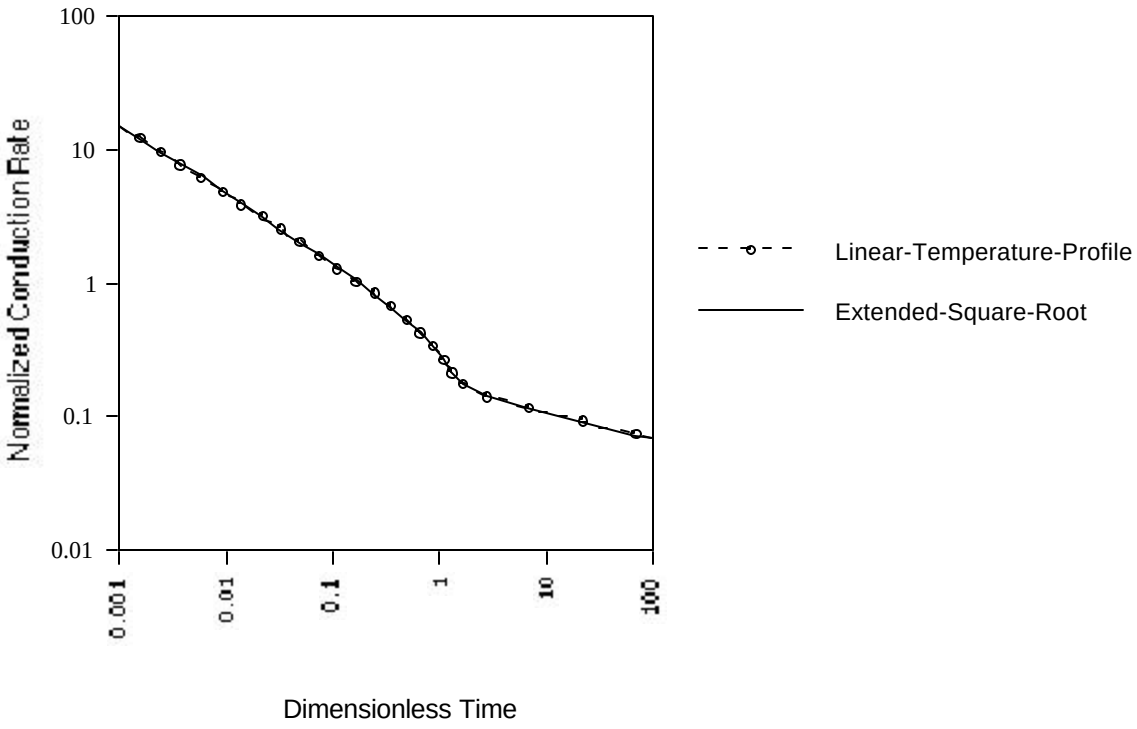

Figure 16a. Comparison of Early-Time Linear-Temperature-Profile Rate Model: Slab Geometry

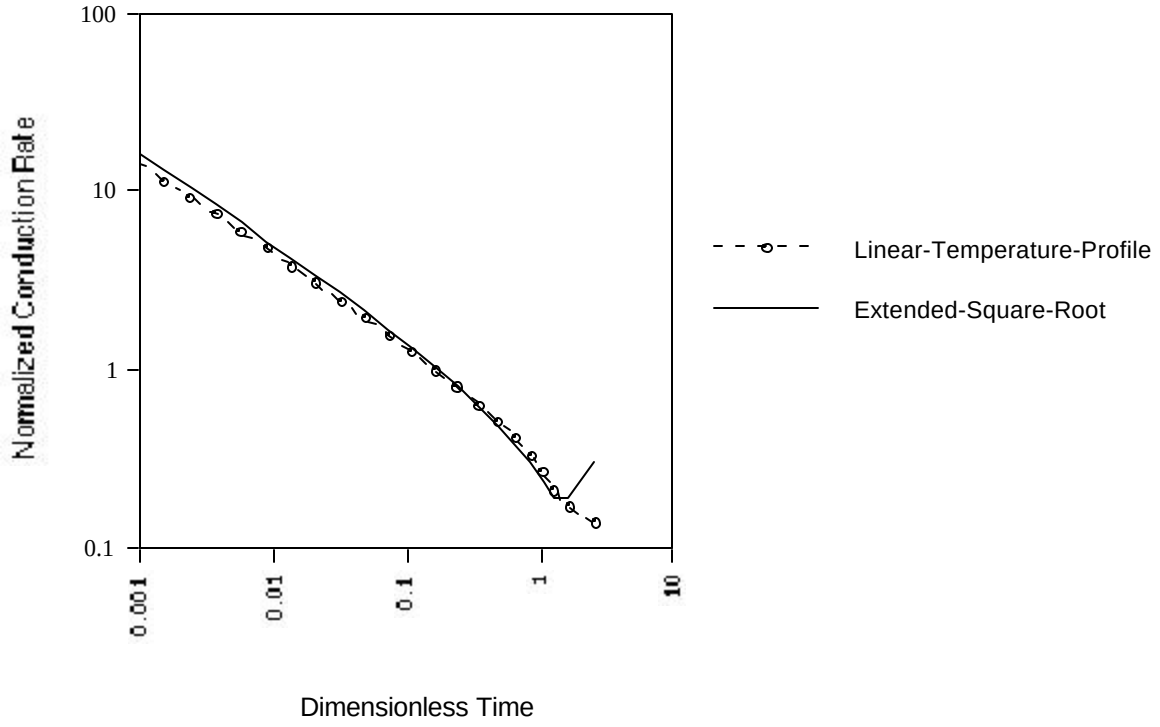

Figure 16b. Comparison of Early-Time Linear-Temperature-Profile Rate Model: Matchstick Geometry

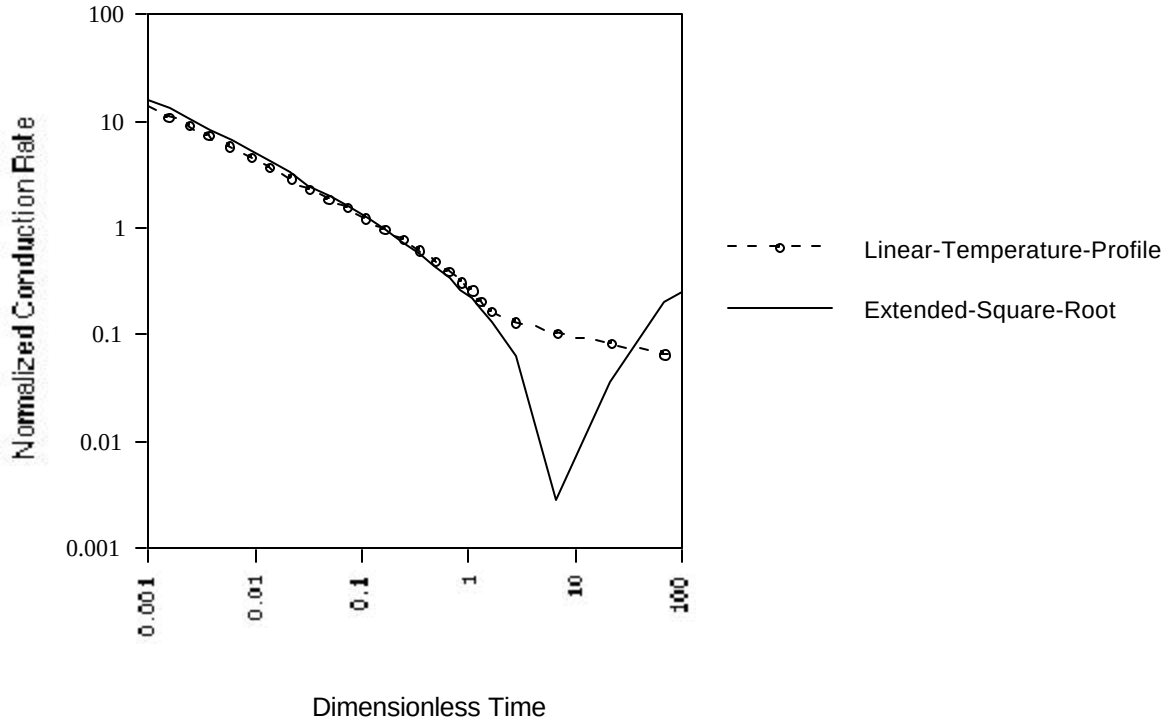

Figure 16c. Comparison of Early-Time Linear-Temperature-Profile Rate Model: Cubic Geometry

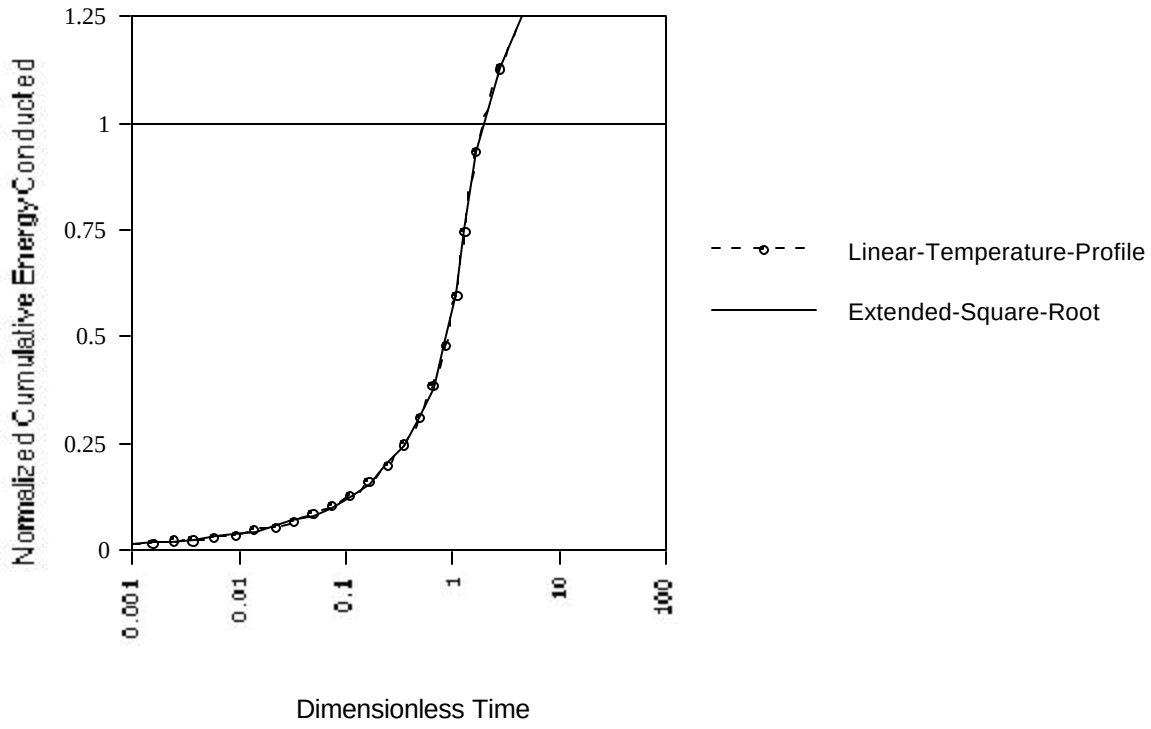

Figure 17a. Comparison of Early-Time Linear-Temperature-Profile Cumulative Model: Slab Geometry

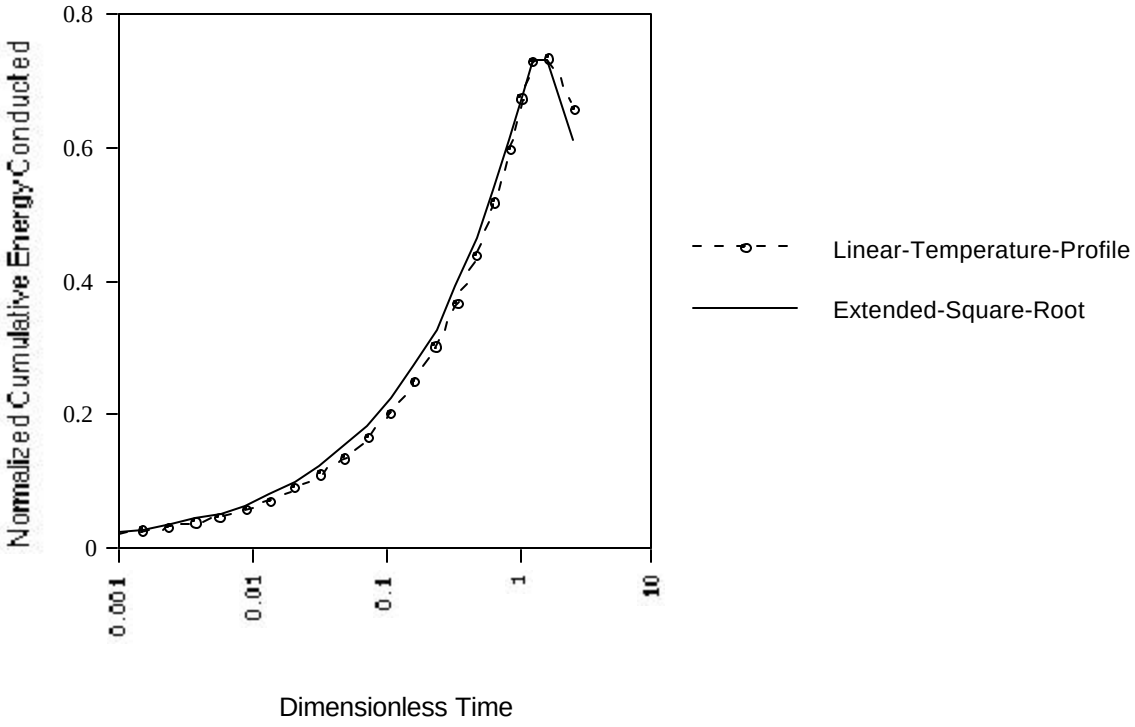

Figure 17b. Comparison of Early-Time Linear-Temperature-Profile Cumulative Model: Matchstick Geometry

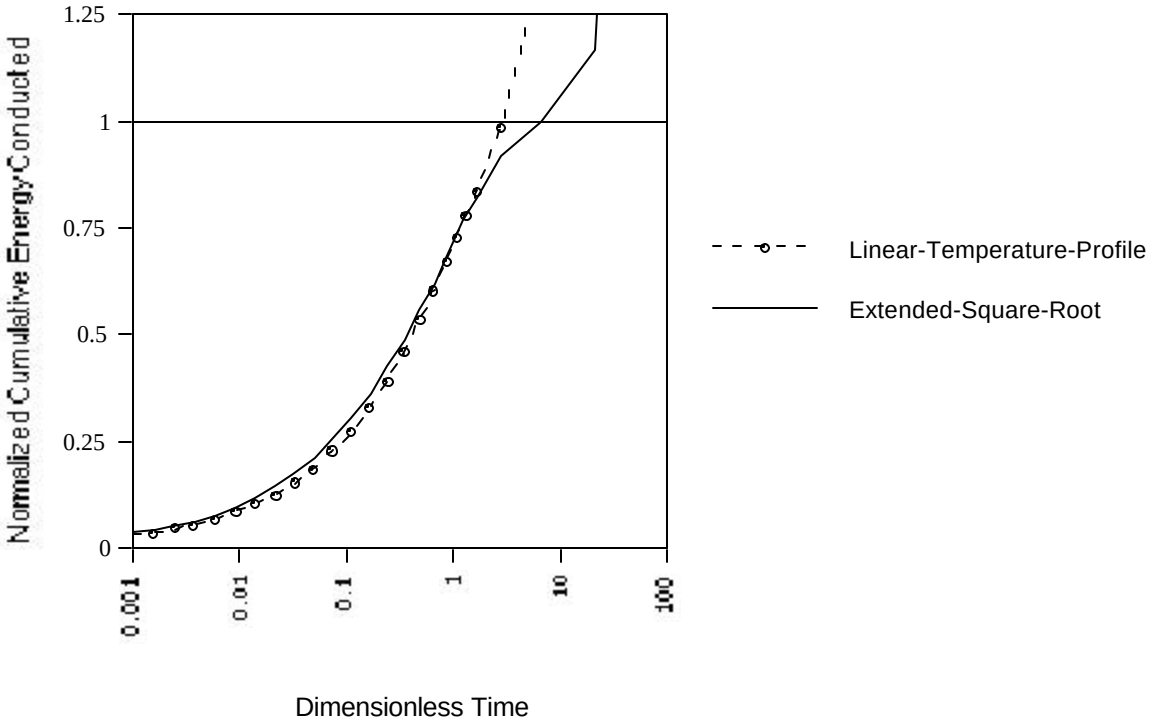

Figure 17c. Comparison of Early-Time Linear-Temperature-Profile Cumulative Model: Cubic Geometry

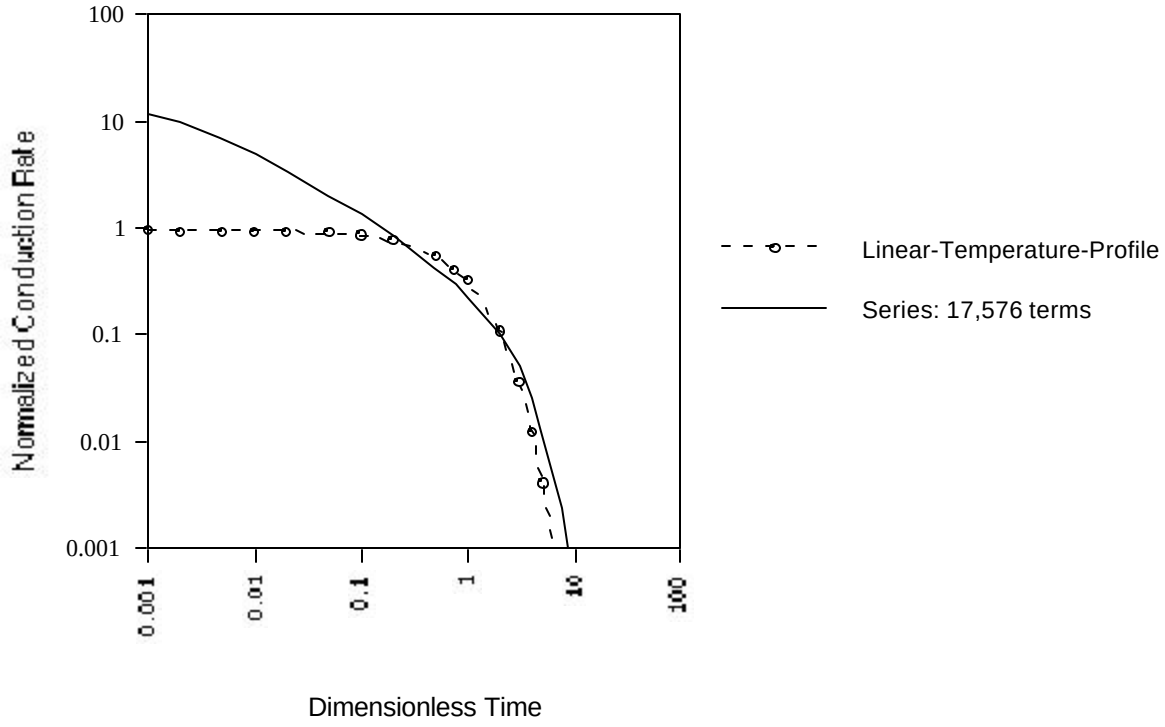

Figure 18. Comparison of Late-Time Linear-Temperature-Profile Rate Model: Cubic Geometry

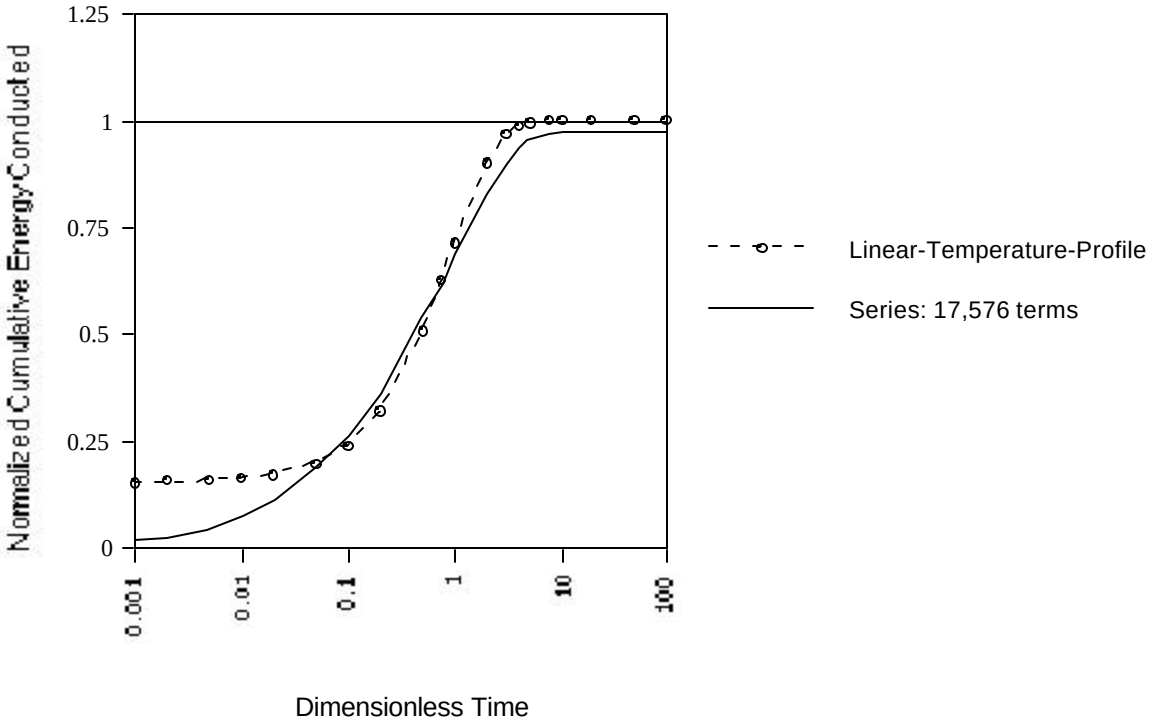

Figure 19. Comparison of Late -Time Linear-Temperature-Profile Cumulative Model: Cubic Geometry

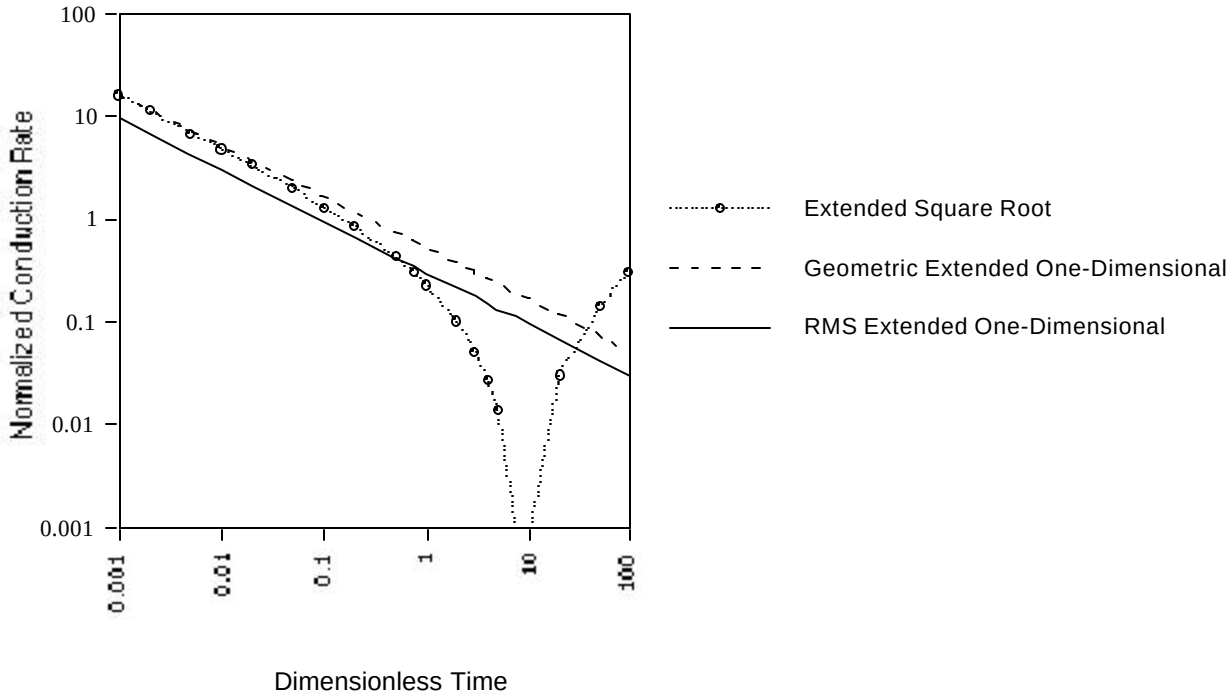

Figure 20. Comparison of Extended One-Dimensional Rate Model: Cubic Geometry

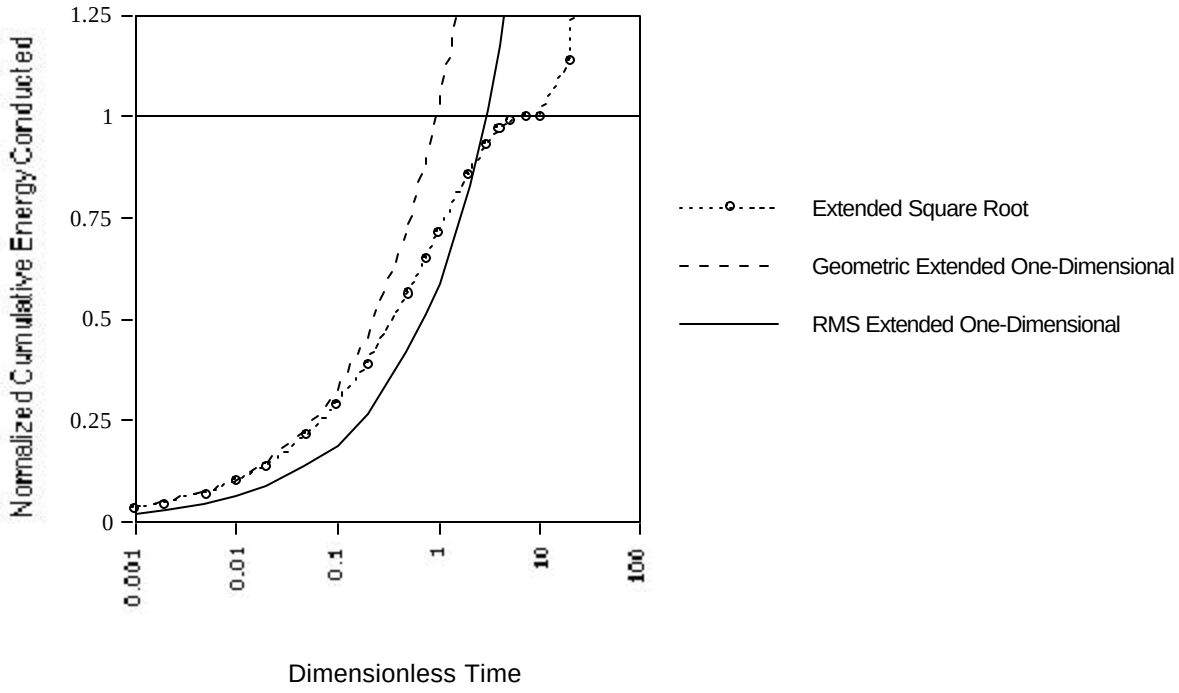

Figure 21. Comparison of Extended One-Dimensional Cumulative Model: Cubic Geometry

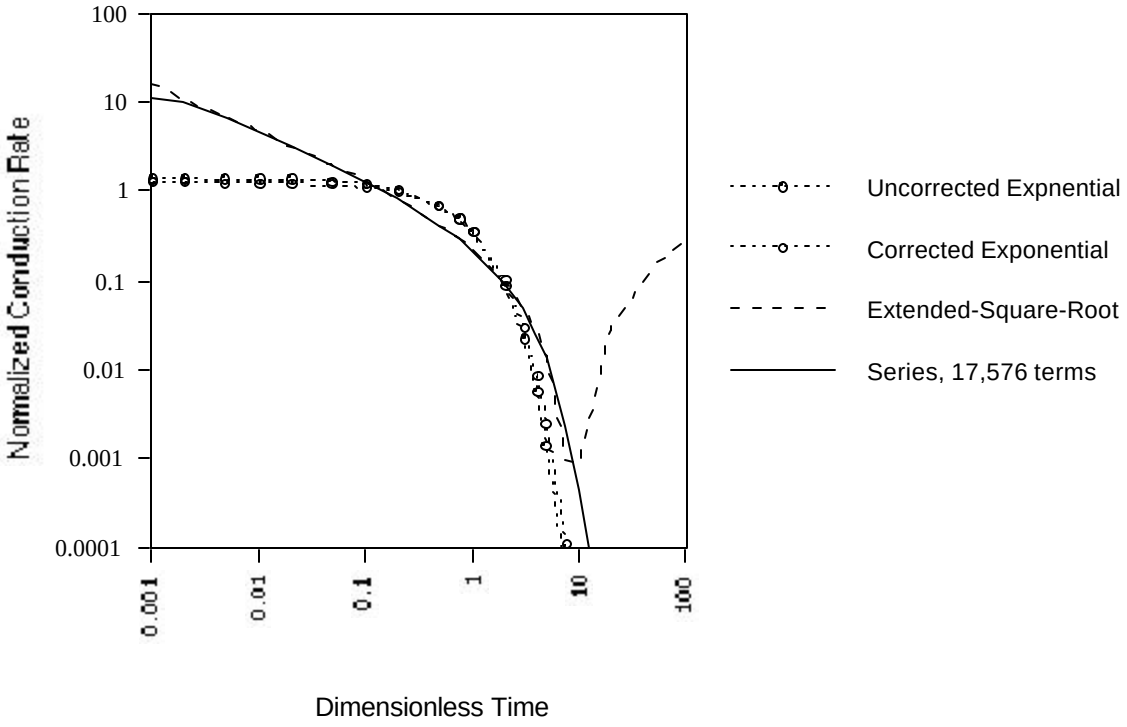

Figure 22. Comparison of Exponential Rate Model: Cubic Geometry

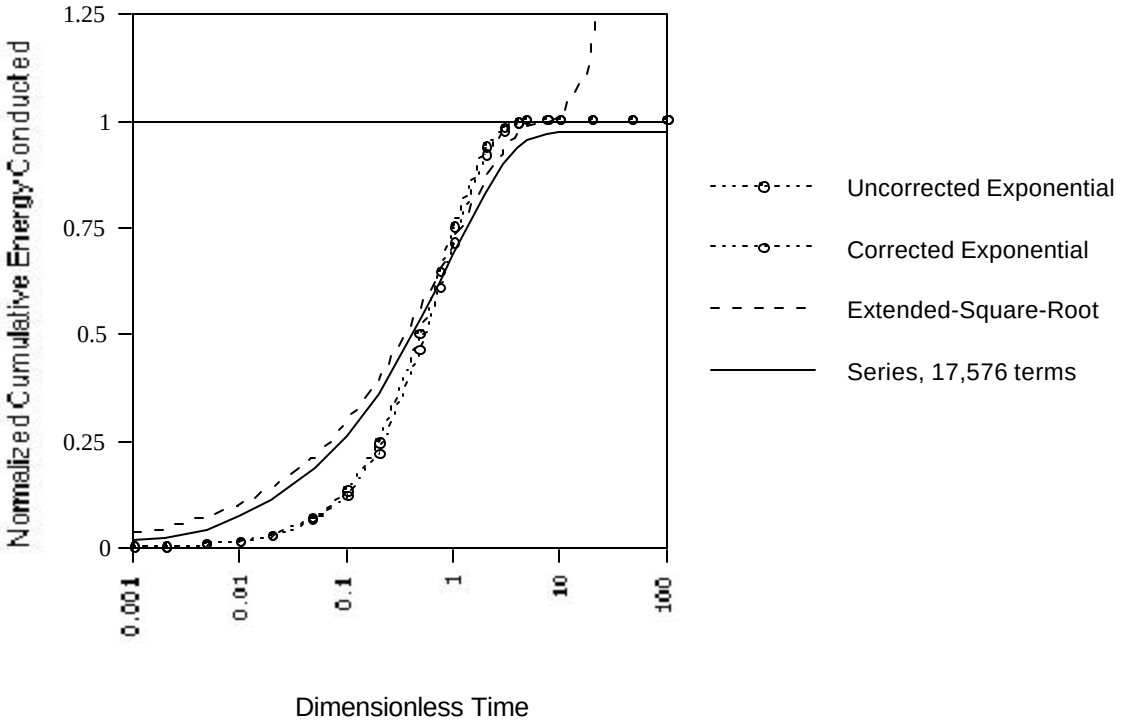

Figure 23. Comparison of Exponential Cumulative Model: Cubic Geometry

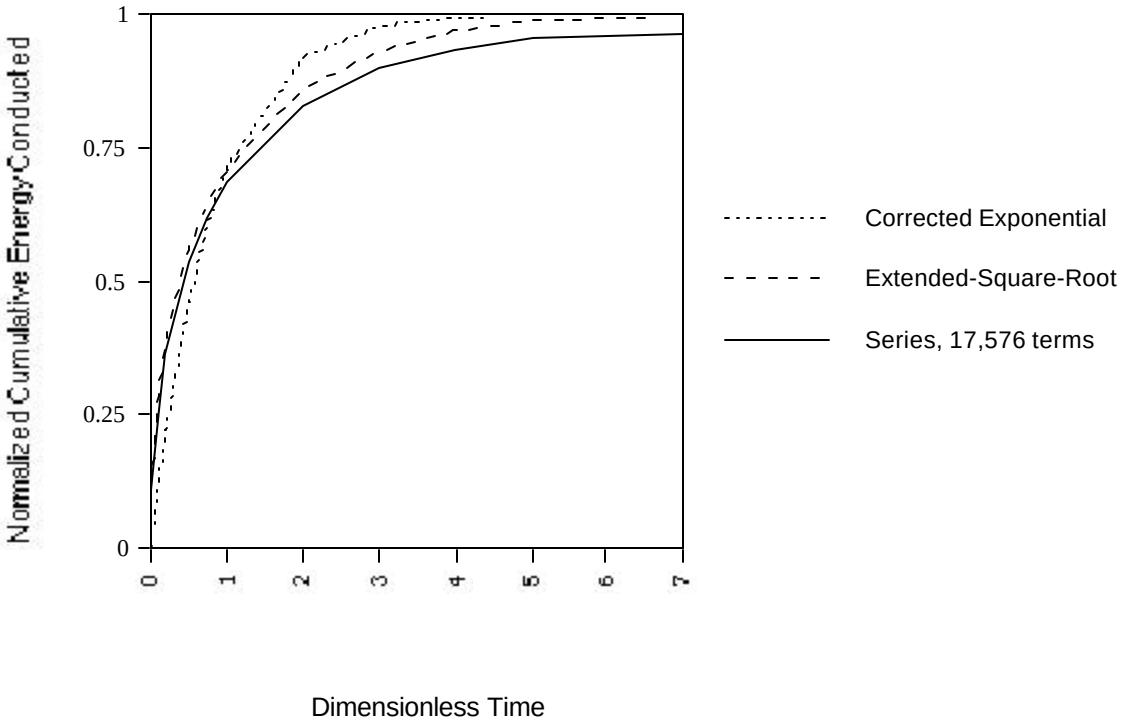

Figure 24. Comparison of Exponential Cumulative Model, Linear Scale: Cubic Geometry

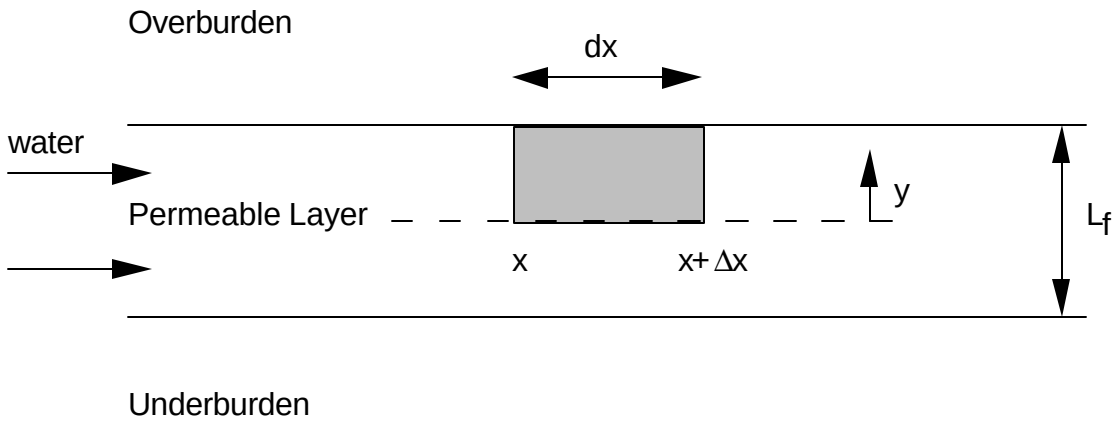

Figure 25. Geometry of Lauwerier Model

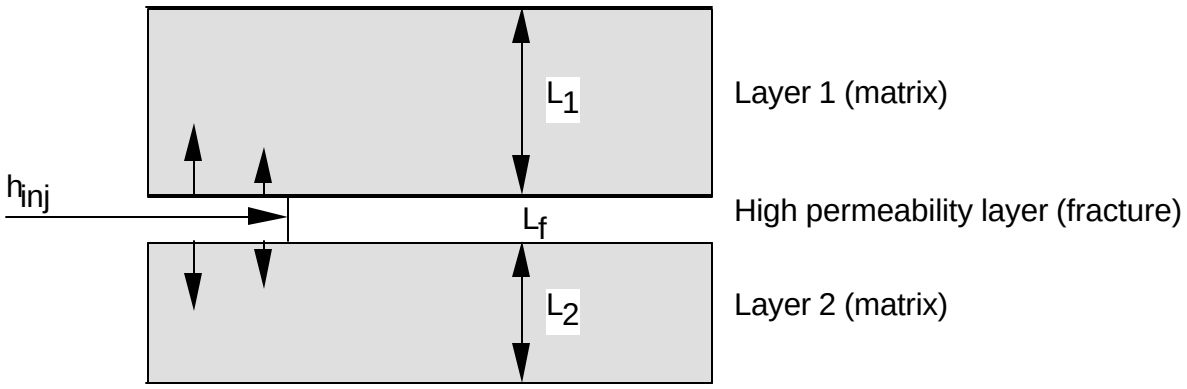

Figure 26. Geometry of New One-Dimensional Thermal Model

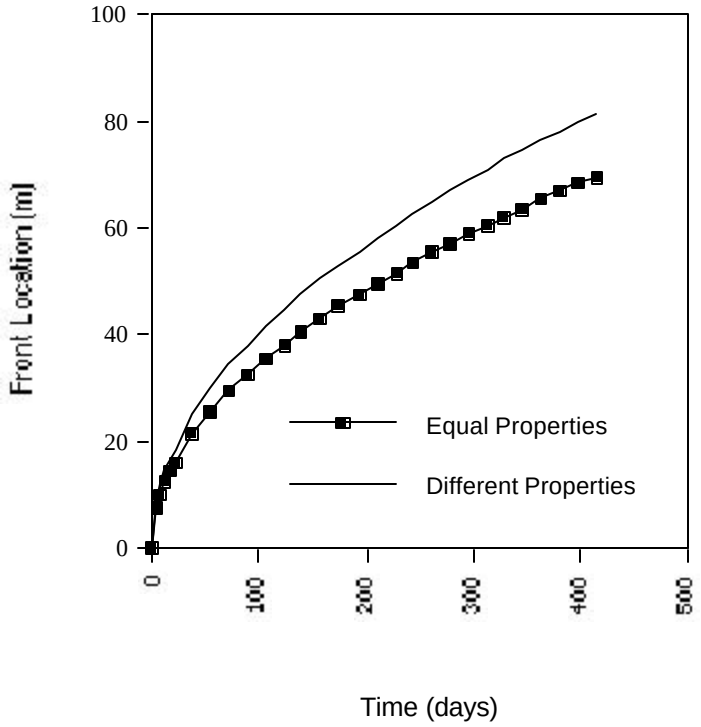

Figure 27. Effect of Matrix Properties for One-Dimensional, Early-Time Models

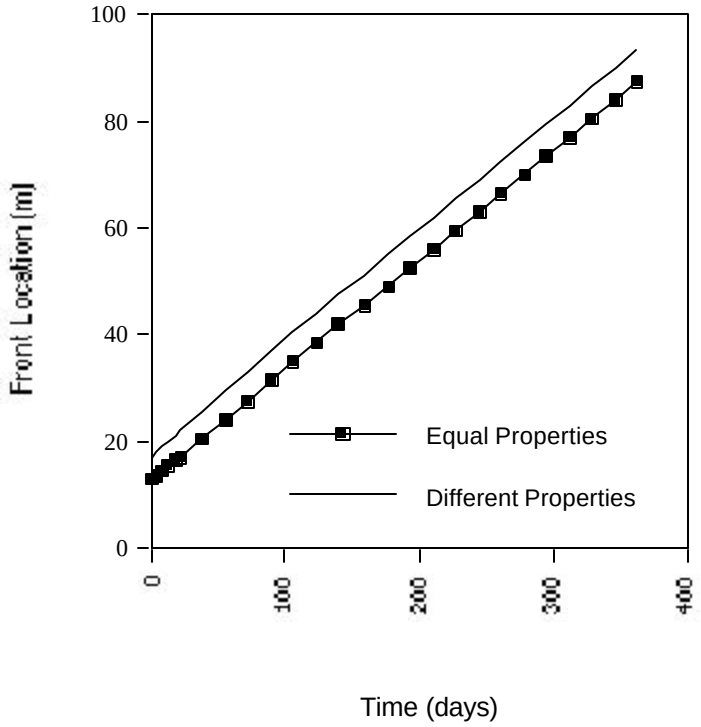

Figure 28. Effect of Matrix Properties for One-Dimensional, Late-Time Models

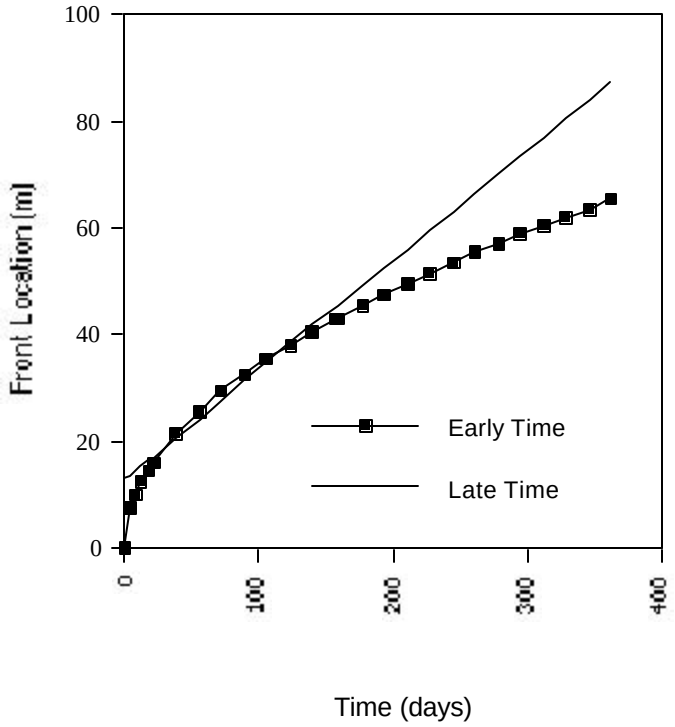

Figure 29. Comparison of One-Dimensional Thermal Advance Models: Identical Properties

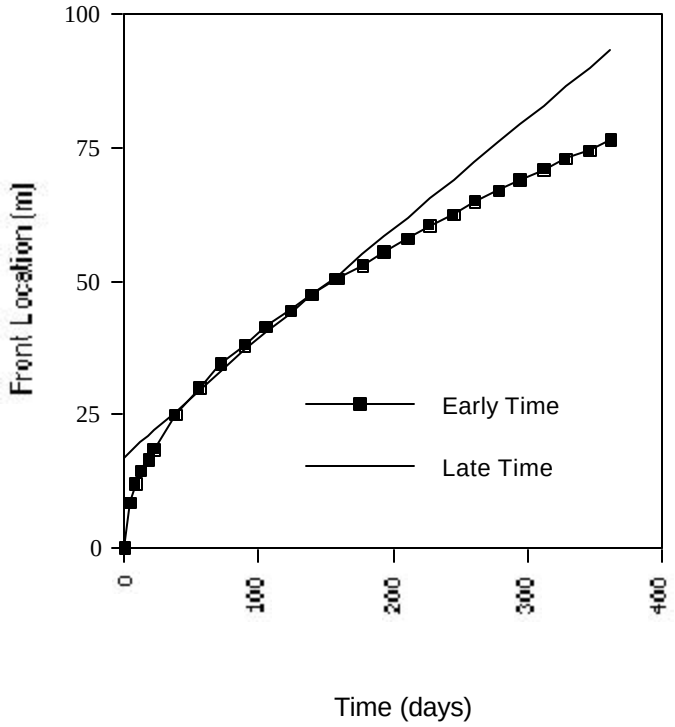

Figure 30. Comparison of One-Dimensional Thermal Advance Models: Different Properties

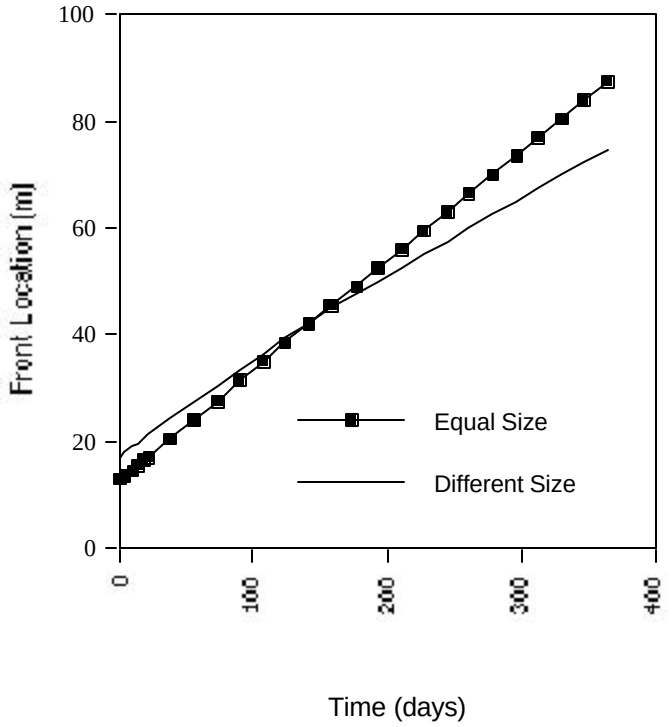

Figure 31. Effect of Matrix Size for One-Dimensional, Late -Time Models

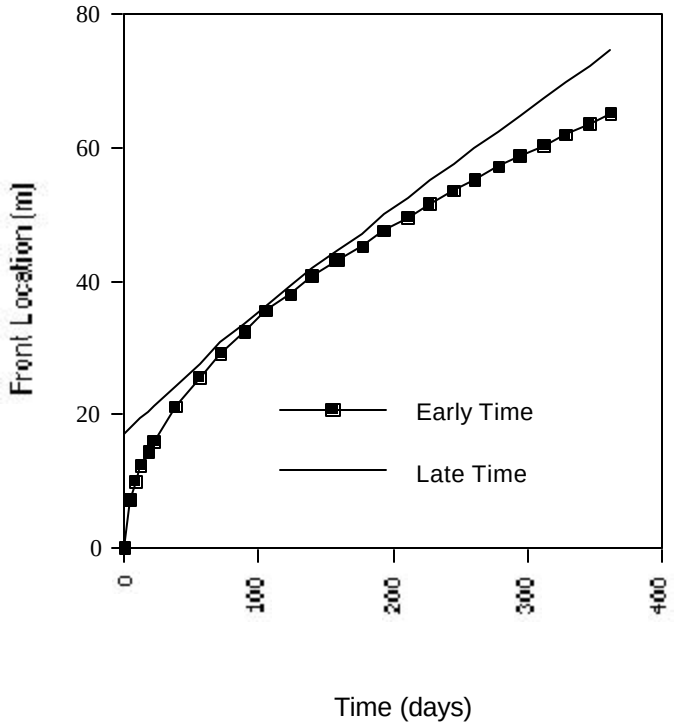

Figure 32. Comparison of One-Dimensional Thermal Advance Models: Different Size

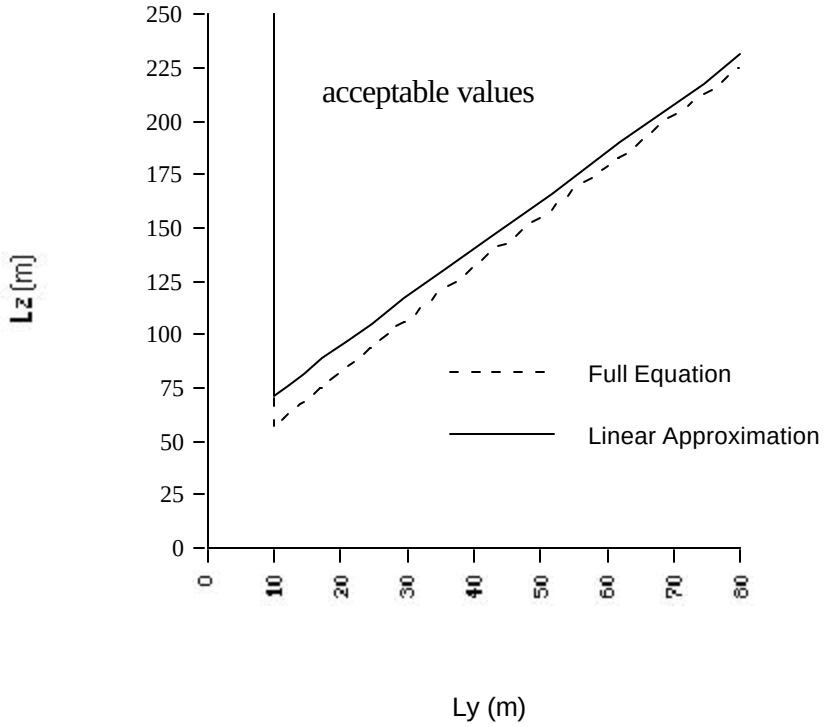

Figure 33. Acceptable Matrix Block Dimensions for L_x = 10 m

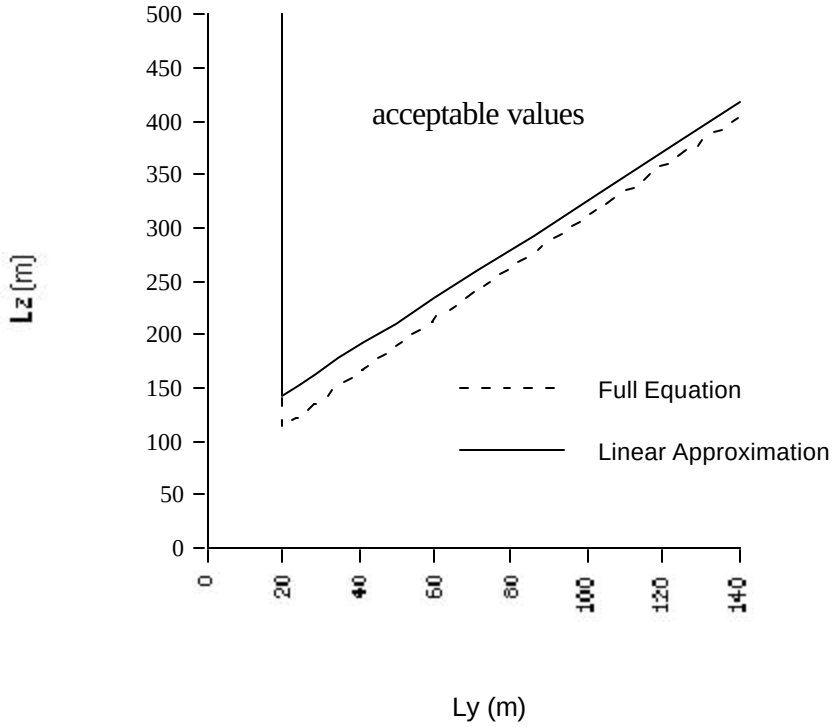

Figure 34. Acceptable Matrix Block Dimensions for L_x = 20 m

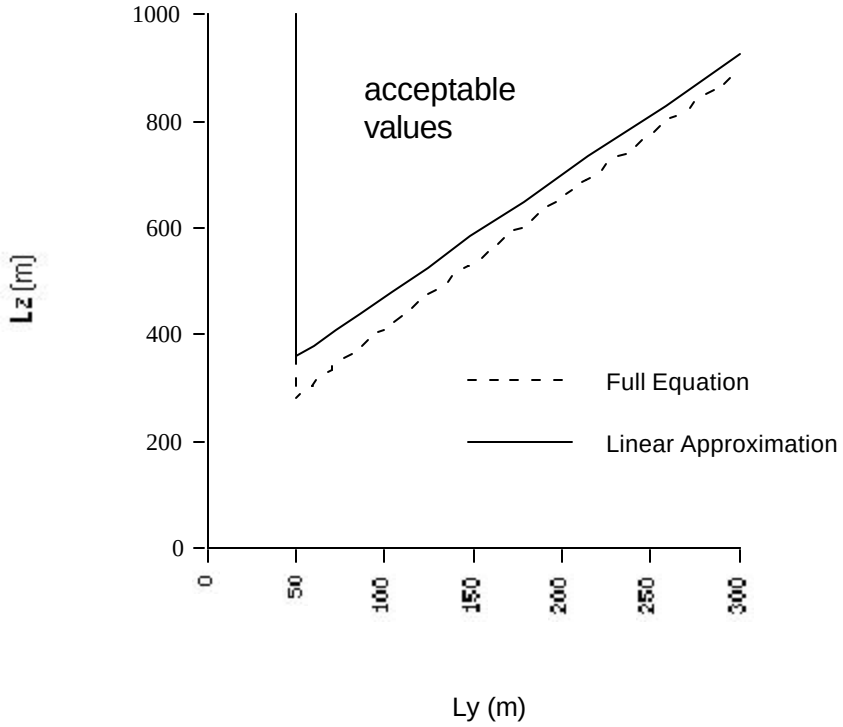

Figure 35. Acceptable Matrix Block Dimensions for L_x = 50 m

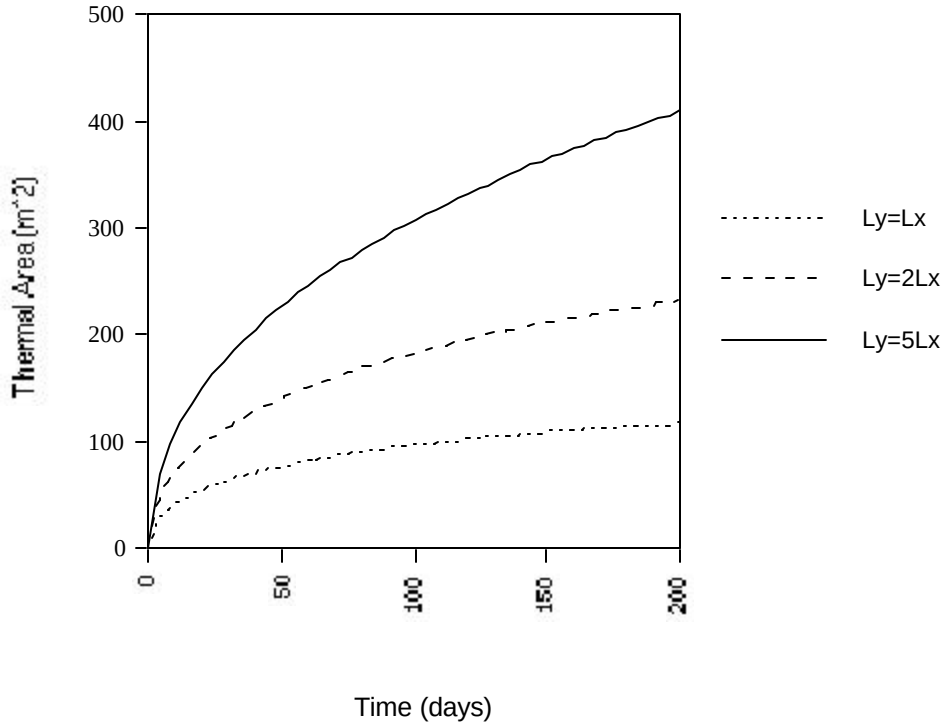

Figure 36. Effect of Matrix Block Shape on Thermal Area, L_x=10 m

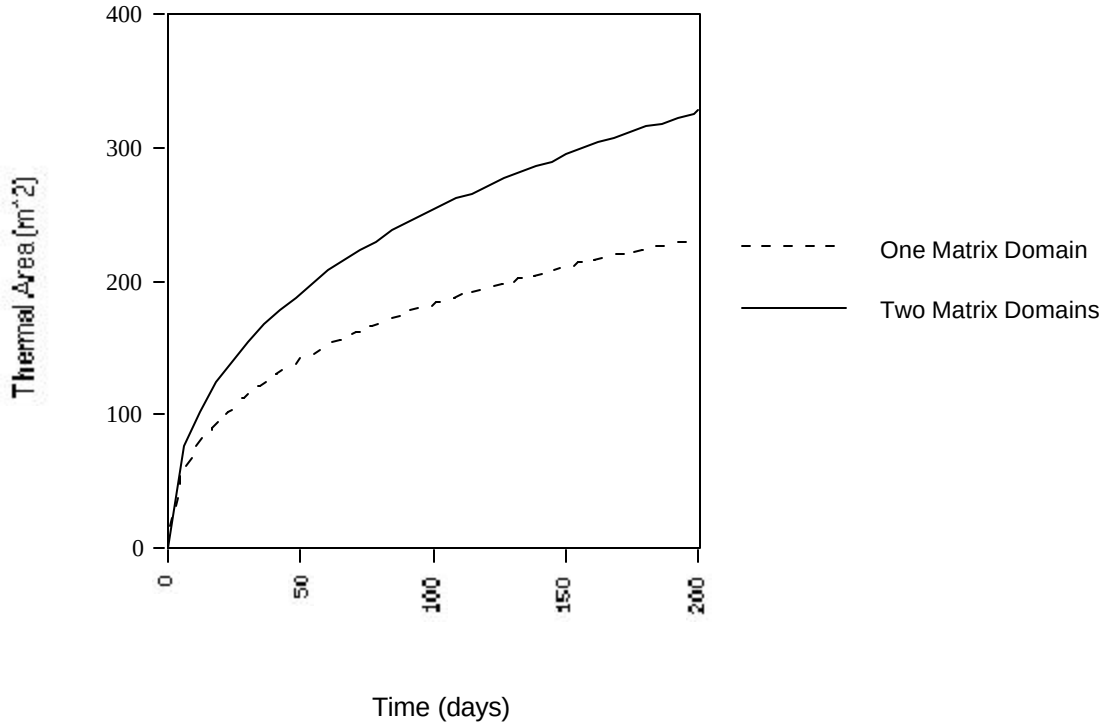

Figure 37. Effect of Multiple Matrix Domains having Different Sized Matrix Blocks

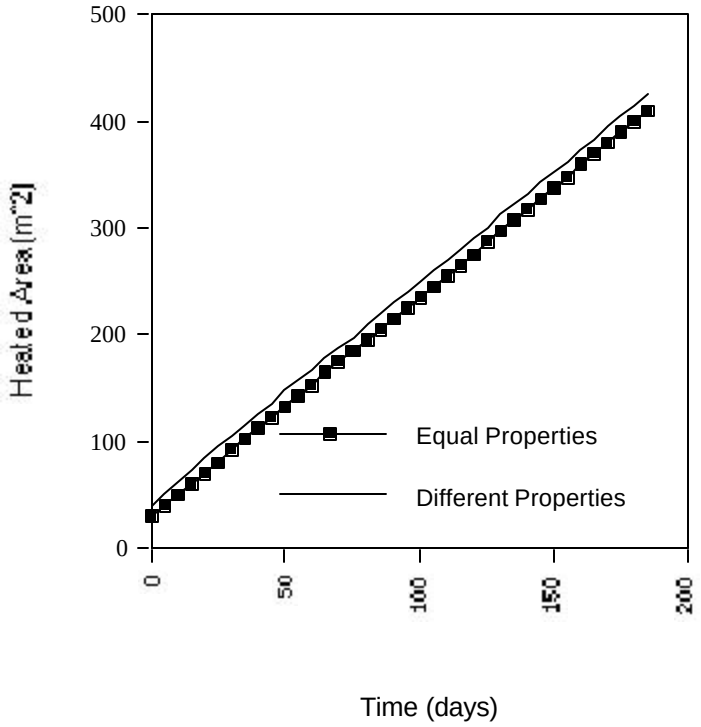

Figure 38. Effect of Matrix Properties for Multi-Dimensional, Late-Time Models

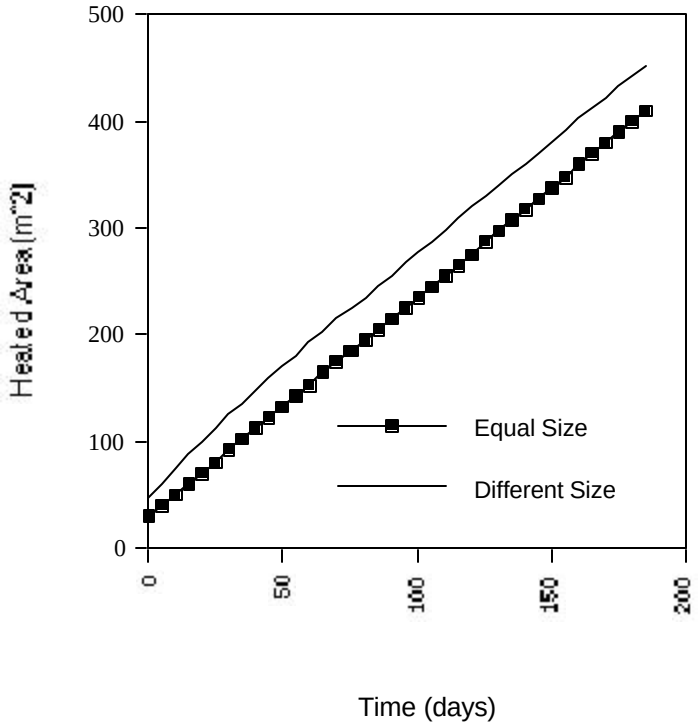

Figure 39. Effect of Matrix Size for Multi -Dimensional, Late -Time Models

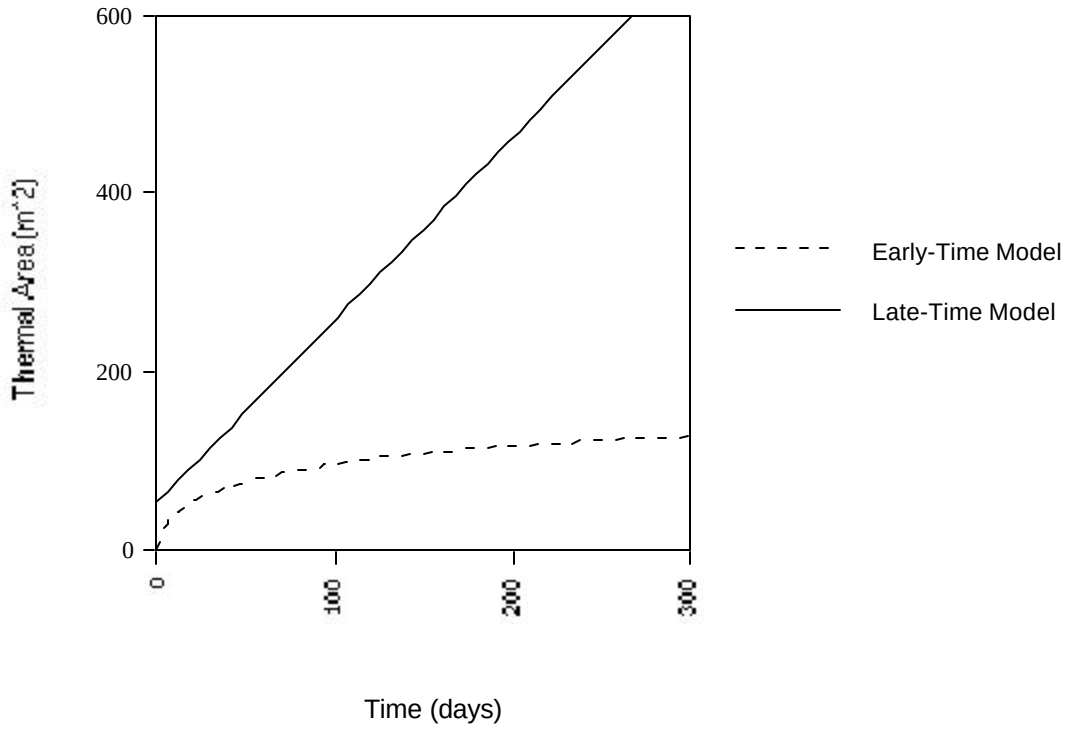

Figure 40. Comparison of Early- and Late-Time Models for 3-D Matrix Blocks

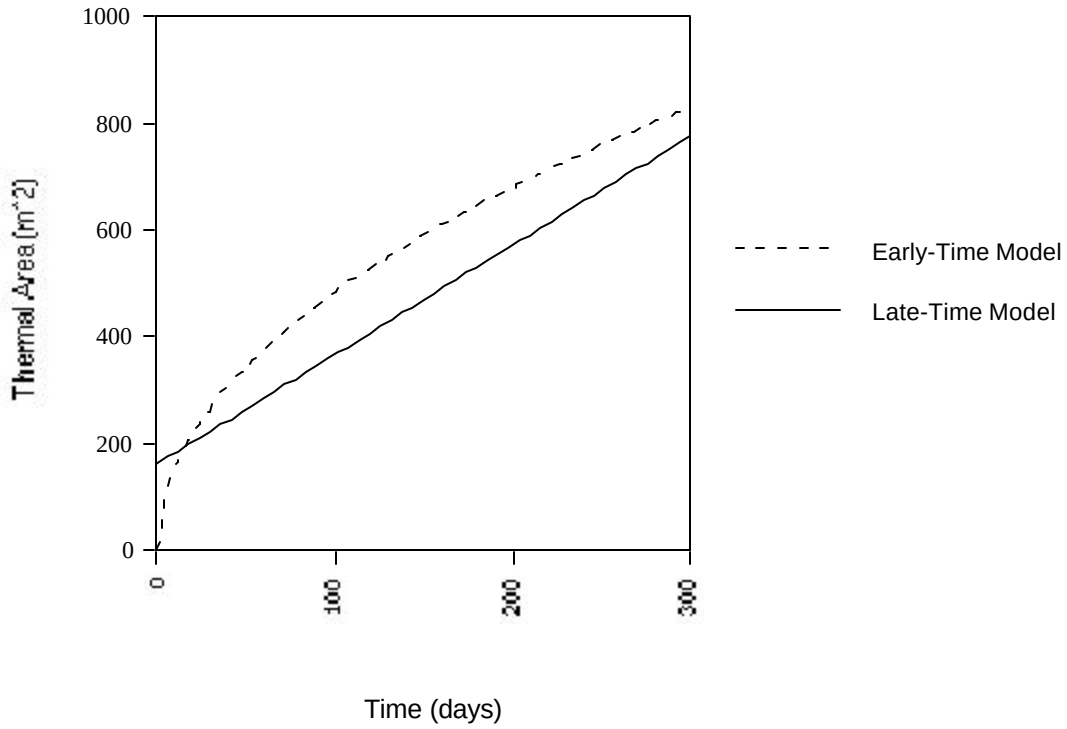

Figure 41. Comparison of Early- and Late-Time Models for 1-D Matrix Blocks

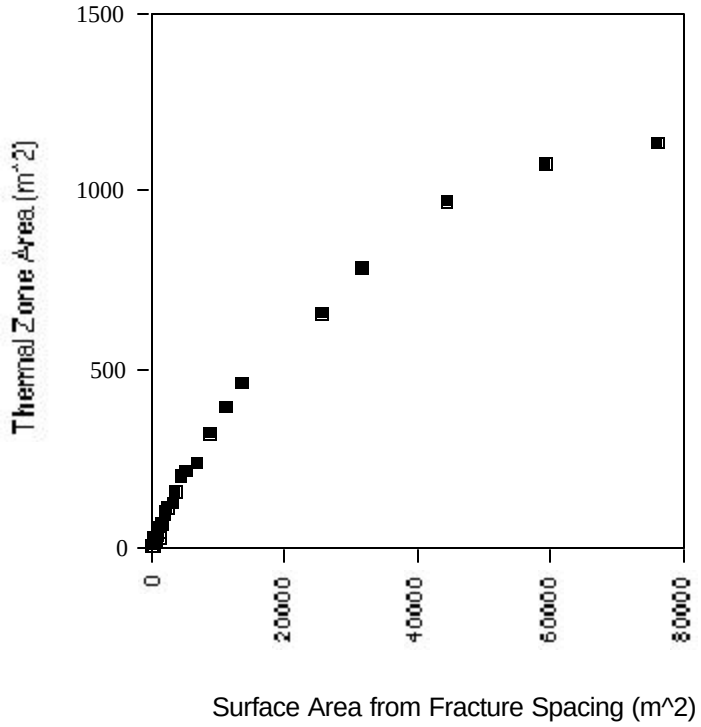

Figure 42. Effect of Matrix Block Surface Area on Extent of Thermal Area

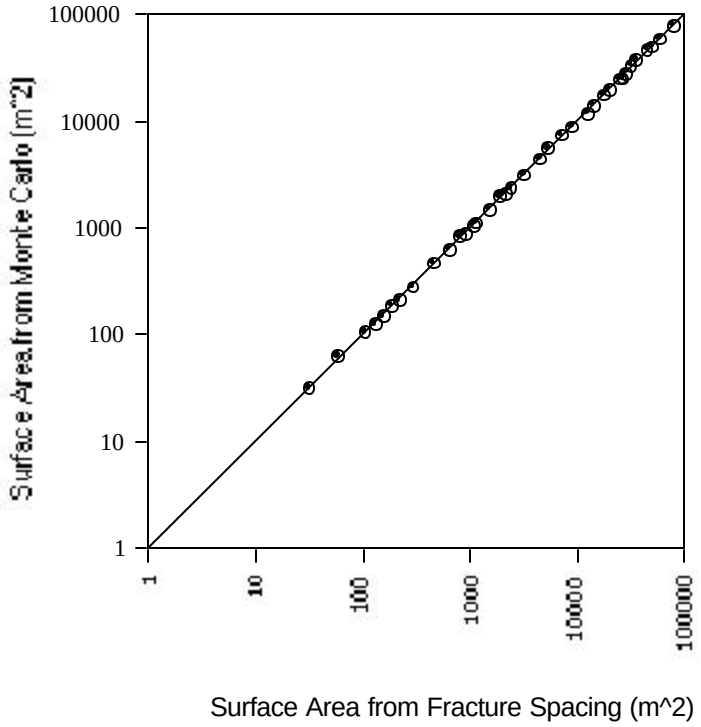

Figure 43. Relationship between Matrix Block Surface Area Generated from Monte Carlo Analysis and from Average Fracture Spacings.

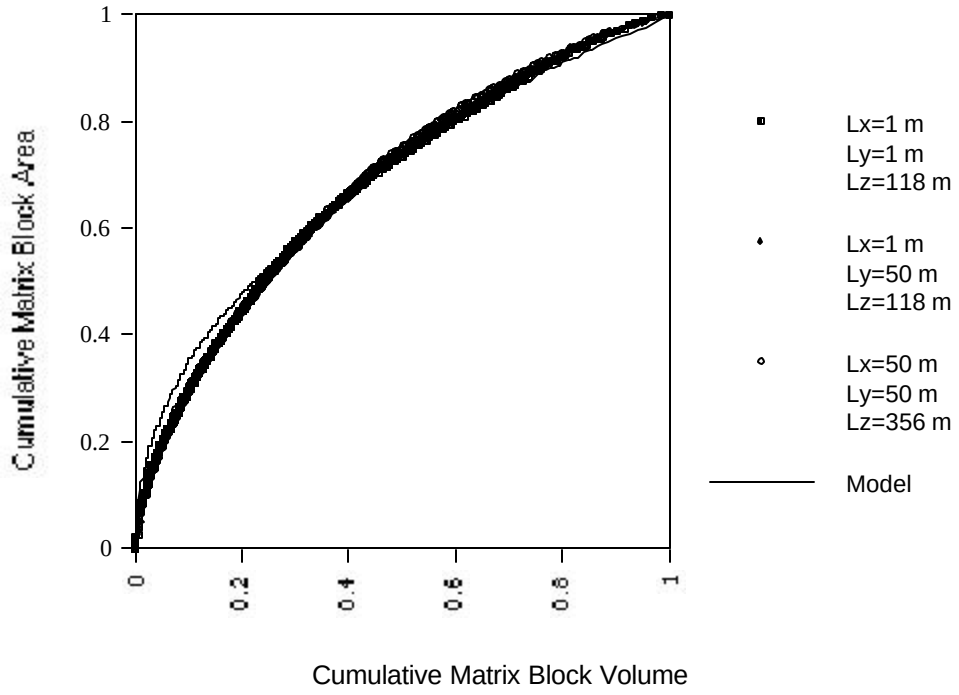

Figure 44. Fractional Cumulative Matrix Block Surface Area as a Function of Fractional Cumulative Matrix Block Volume

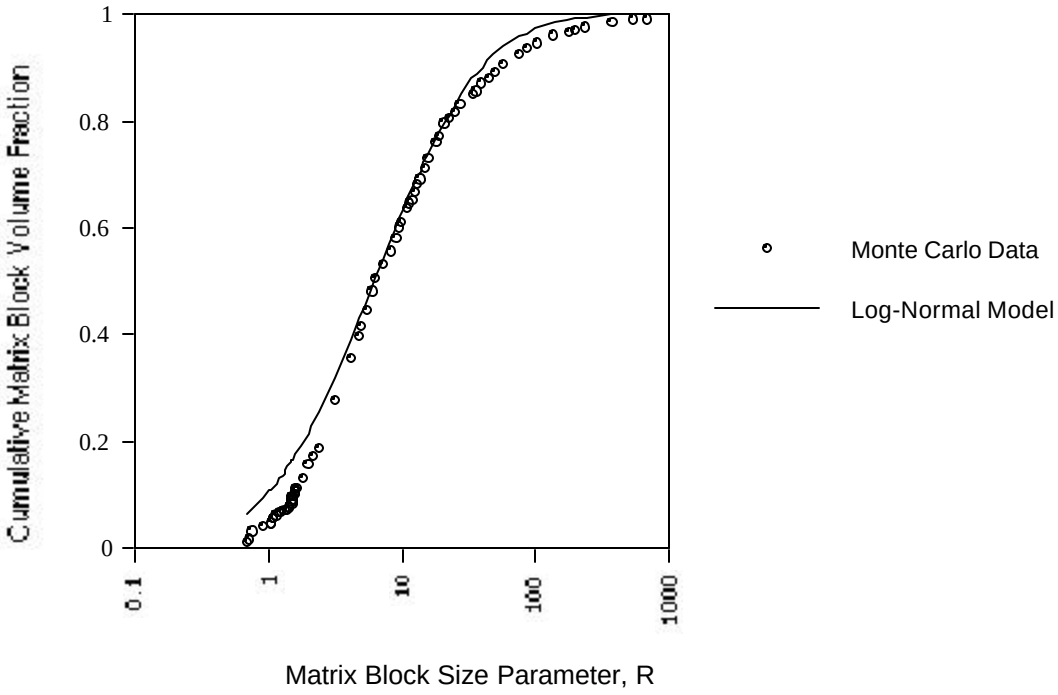

Figure 45. Comparison of Monte Carlo and Curve-Fit Matrix Block Size Parameters, Late-Time Model

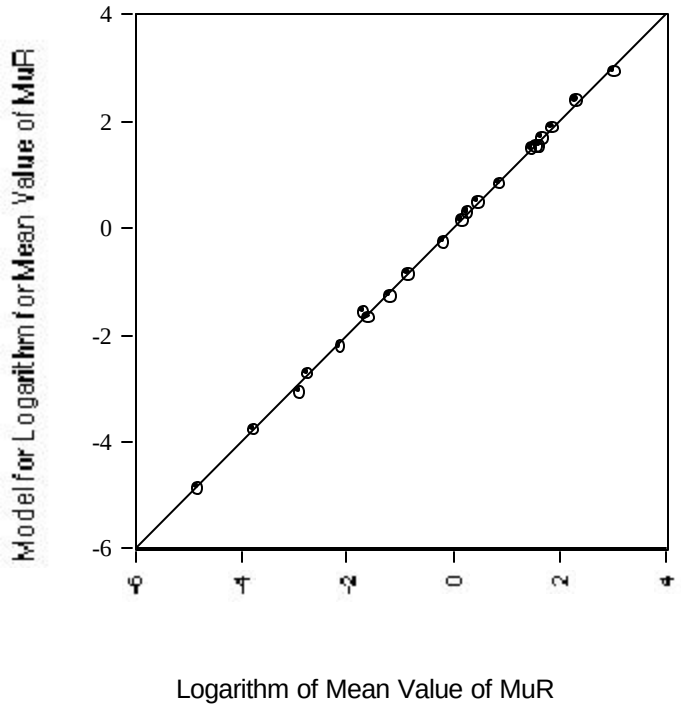

Figure 46. Validity of Eq. 7.3.14 for Modeling Logarithm of μ_R.

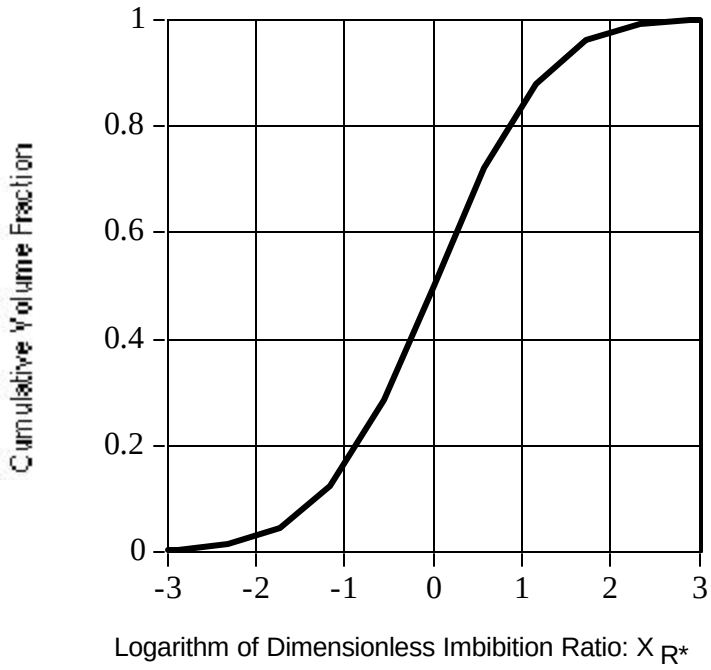

Figure 47. Dimensionless Relationship Between Matrix Block Size Parameter, R, and Matrix Block Volume Fraction

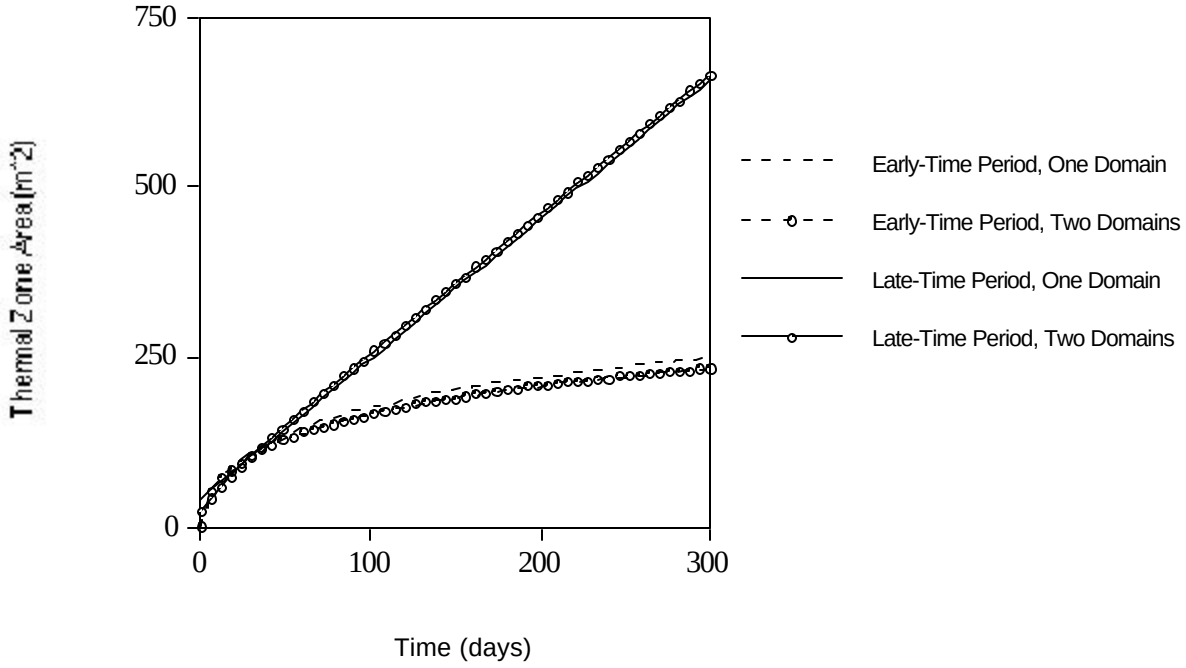

Figure 48. Comparison of Models